

**OXYGEN STORAGE PROPERTIES OF DOUBLE PEROVSKITE
OXIDES CONTAINING MANGANESE**

A Dissertation Presented to
the Faculty of the Department of Chemistry
University of Houston

In Partial Fulfillment
of the Requirements for the Degree
Doctor of Philosophy

By
Kannika Jeamjumnunja

May 2017

**OXYGEN STORAGE PROPERTIES OF DOUBLE PEROVSKITE
OXIDES CONTAINING MANGANESE**

Kannika Jeamjumnunja

APPROVED:

Dr. Allan J. Jacobson, Chairman

Dr. Arnold M. Guloy

Dr. P. Shiv Halasyamani

Dr. Shoujun Xu

Dr. Yan Yao

Dean, College of Natural Sciences and Mathematics

To my parents and family

Acknowledgements

First and foremost, I would like to express the deepest appreciation to Dr. Allan Jacobson, my doctoral advisor, for the guidance and mentorship that he has provided to me. He has been an excellent and very supportive advisor. His patience and generosity have always been admirable, and I am truly fortunate to have had the opportunity to work with him. I am also very grateful to my dissertation committee members, Dr. Arnold Guloy, Dr. Shiv Halasyamani, Dr. Shoujun Xu, and Dr. Yan Yao for the valuable and constructive suggestions.

I wish to express my appreciation to the past and present members of the Jacobson's research group. I am very much grateful to my mentor, Dr. Wenquan Gong for his dedicated help and guidance in the solid-state electrochemical experiments. I would also like to thank Tanya Makarenko (and Dr. Boris Makarenko) for their assistance with TGA, DSC, dilatometry measurements, and whatever else in the lab I needed. I thank Dr. Xiqu Wang for his help with high-temperature X-ray diffraction. I thank to my labmates, Julie, Bee, Sam, Parastou, and Dmitry for warm and friendly environment. I also cannot express enough thanks to Ellen Lee, our lab manager, who has always been there to provide us with whatever assistance that we need.

I am indebted to several people who shared their valuable time and research expertise. I wish to express my great appreciation to Dr. Zhongjia Tang (XRD), Dr. James Meen (SEM, EDS, and microprobe), Dr. Karoline Mueller (XRD and SEM). I also thank Dr. Jakoah Brgoch and Dr. Arnold Guloy for giving me access to their lab facilities. My grateful thanks are also extended to the staff in the chemistry department,

including, but not limited to Mark (machine work), Roger (glass work), and Jerry (computer work).

My graduate study at University of Houston would be impossible without the generous support of Dr. Randall Lee. I am deeply grateful to him. I also thank my seniors, Weekit and Nuttawut who have helped me countlessly over the course work of my graduate study. My life in Houston would have been less enjoyable without my lovely friends, Suchanun, Pawinee, Chalada, Napat, Krit, Sitti, Suppanat, Pannaree, Thamon, and Worawit. I am so grateful to Jerry Law and his family for their warm and kind hospitality. I am very thankful to my best friend, Leela Ruckthong, who has always been there for me.

I wish to express my deep gratitude to Weera and Nareeluk Bunsaringkharnan, who love me like their daughter, for the continuous love, support and care. I gratefully appreciate the support shown by all members of my family, especially uncle Jirawit, uncle Udompruth, aunt Nongluck, and my younger sister Kanpicha.

Finally, and most importantly, I am endlessly grateful to my wonderful grandmother Sudjai, and my parents, Thanapat and Thanaprn for the unconditional love, constant support and endurance. Their support and understanding have helped me to overcome all difficulties during my PhD journey.

**OXYGEN STORAGE PROPERTIES OF DOUBLE PEROVSKITE
OXIDES CONTAINING MANGANESE**

An Abstract of a Dissertation
Presented to
the Faculty of the Department of Chemistry
University of Houston

In Partial Fulfillment
of the Requirements for the Degree
Doctor of Philosophy

By
Kannika Jeamjumnunja

May 2017

Abstract

Non-stoichiometric oxides which are capable of reversibly storing and releasing large amounts of oxygen are called oxygen-storage materials (OSMs). The A-site double-perovskite $\text{LnBaMn}_2\text{O}_{5+\delta}$ oxides have attracted a lot of interest as good OSM candidates for various oxygen-related applications, such as chemical looping, combustion and oxygen separation. In this work, the oxygen uptake/release behavior of the $\text{LnBaMn}_2\text{O}_{5+\delta}$ ($\text{Ln} = \text{Y, Gd, Eu, Sm, Nd, and Pr}$) compounds were investigated by thermogravimetry. The results show good oxygen uptake/release ability at moderate temperatures with oxygen-storage capacity exceeding 3 wt. % for all compounds. Oxygen uptake begins at lower temperatures in both air and oxygen in the compounds with larger Ln^{3+} ions. These oxides show almost complete and reversible oxygen uptake/release between $\text{LnBaMn}_2\text{O}_5$ and $\text{LnBaMn}_2\text{O}_6$ during switching between oxygen (or air) and 1.99% H_2/Ar .

The oxygen non-stoichiometries of the $\text{LnBaMn}_2\text{O}_{5+\delta}$ ($\text{Ln} = \text{Y, Gd, and Pr}$) oxides were determined as a function of $p\text{O}_2$ at different temperatures by Coulometric titration. These materials exhibit two distinct phases (with $\delta \approx 0, 0.5$) and a third phase with a range of composition with the δ value approaching to ~ 1 during oxidation/reduction. The phase transition occurs at higher $p\text{O}_2$ with increasing temperature. Isothermal experiments show that the larger the Ln^{3+} cation the lower $p\text{O}_2$ for phase conversion. The thermodynamic quantities corresponding to the phase transition were investigated. At some temperatures and $p\text{O}_2$ conditions, the $\text{LnBaMn}_2\text{O}_{5+\delta}$ compounds are unstable with respect to decomposition to $\text{BaMnO}_{3-\delta}$ and LnMnO_3 .

The electrical conductivity of YBaMn_2O_5 was studied as a function of temperature by using the four-probe DC method in an electrochemical cell in the low- $p\text{O}_2$ range of 10^{-16} to 10^{-23} atm. The electrical conductivity is relatively low with an average activation energy (E_a) of 0.87 eV in 500-700 °C. Barium migration and segregation on the sample surface were observed after the long-period experiments in low- $p\text{O}_2$ atmosphere at high temperatures. The linear thermal expansion for the three phases (O_5 , O_6 , and $\text{O}_{5.5}$) of $\text{YBaMn}_2\text{O}_{5+\delta}$ was investigated by dilatometry measurements and high-temperature XRD studies under different atmospheres. The phase transitions of $\text{LnBaMn}_2\text{O}_6$ were examined by DSC measurements.

Table of Contents

Acknowledgements	iv
Abstract	vii
List of Figures	xiii
List of Tables	xviii
List of Symbols and Abbreviations	xx
CHAPTER 1: Introduction	1
1.1 Objective	1
1.2 Scope of the thesis	1
1.3 The Perovskite Structure	2
1.4 Theoretical Background	3
1.4.1 Defect Chemistry and Non-stoichiometry	4
1.4.2 Electrical Conductivity	6
1.4.3 Thermodynamic Quantities	8
1.5 References	11
CHAPTER 2: Synthesis, Crystal Structure and Oxygen Storage Properties of the Double-Perovskites $\text{LnBaMn}_2\text{O}_{5+\delta}$ (Ln = Y, Gd, Eu, Sm, Nd, and Pr)	13
2.1 Introduction	13
2.2 Experimental Section	17

2.2.1	Synthesis of $\text{LnBaMn}_2\text{O}_{5+\delta}$	17
2.2.2	Crystal Structure Analysis	18
2.2.3	Chemical Analysis	19
2.2.4	Thermogravimetric Analysis	19
2.3	Results and Discussion	20
2.3.1	Synthesis and Crystal structure of $\text{LnBaMn}_2\text{O}_{5+\delta}$ at room temperature	20
2.3.2	Oxygen Storage Properties	26
2.4	Conclusions	30
2.5	References	30
	Appendix	35

CHAPTER 3: Oxygen Non-stoichiometry of the Oxygen Storage

	Materials $\text{LnBaMn}_2\text{O}_{5+\delta}$ (Ln = Y, Gd, and Pr)	40
3.1	Introduction	40
3.2	Experimental Section	41
3.2.1	Sample Preparation	41
3.2.2	Solid-State Coulometric Titration	42
	3.2.2.1 Theoretical background	42
	3.2.2.2 Experimental details of solid-state Coulometric titration	46
3.3	Results and Discussion	47
3.3.1	Coulometric Titration of $\text{YBaMn}_2\text{O}_{5+\delta}$	47
	3.3.1.1 Oxygen non-stoichiometry	47
	3.3.1.2 Kinetics effect and phase stability	52

3.3.2	Coulometric titration of $\text{GdBaMn}_2\text{O}_{5+\delta}$	54
3.3.2.1	Oxygen non-stoichiometry	54
3.3.2.2	Kinetics and phase stability	58
3.3.3	Coulometric titration of $\text{PrBaMn}_2\text{O}_{5+\delta}$	61
3.3.3.1	Oxygen non-stoichiometry	61
3.3.3.2	Kinetics and phase stability	64
3.3.4	Effect of A-site cationic substitution on phase conversion	66
3.3.5	Thermodynamics	68
3.4	Conclusions	71
3.5	References	72

CHAPTER 4: Electrical Conductivity and Thermal Expansion

	of $\text{YBaMn}_2\text{O}_{5+\delta}$	77
4.1	Introduction	77
4.2	Experimental Section	79
4.2.1	Pellet Fabrication and Sample Characterization	79
4.2.2	Electrical Conductivity	80
4.2.2.1	Sample preparation	80
4.2.2.2	Theoretical background and experimental details	81
4.2.3	Thermal Expansion	83
4.2.3.1	Dilatometry	83
4.2.3.2	High-temperature XRD studies	85
4.2.4	Differential Scanning Calorimetry (DSC)	85

4.3 Results and Discussion	86
4.3.1 Characterization of the sample	86
4.3.2 Electrical Conductivity	86
4.3.3 Thermal Expansion of $\text{YBaMn}_2\text{O}_{5+\delta}$	91
4.3.3.1 YBaMn_2O_5	91
4.3.3.2 $\text{YBaMn}_2\text{O}_{5.5}$	95
4.3.3.3 YBaMn_2O_6	96
4.3.4 Differential Scanning Calorimetry (DSC) of $\text{LnBaMn}_2\text{O}_6$	101
4.4 Conclusions	103
4.5 References	104
CHAPTER 5: Summary and Future Work	107
5.1 Summary	107
5.2 Future Work	109
5.3 References	110

List of Figures

Figure 1.1	The ideal ABO_3 perovskite structure.	3
Figure 1.2	A schematic diagram for the concentrations of the defects $[V_{O}^{\bullet\bullet}]$, $[Sr'_{La}]$, $[Fe'_{Fe}]$, and $[Fe_{Fe}^{\bullet}]$ as a function of $\log pO_2$ for $La_{1-x}SrFeO_{3-\delta}$.	6
Figure 2.1	Crystal structures of $YBaMn_2O_{5+\delta}$: (a) fully-reduced O_5 phase ($\delta = 0$), (b) half-reduced $O_{5.5}$ phase ($\delta = 0.5$), and (c) fully-reduced O_6 phase ($\delta = 1$).	16
Figure 2.2	X-ray data for (a) $GdBaMn_2O_5$, (b) $GdBaMn_2O_{5.5}$, and (c) $GdBaMn_2O_6$.	23
Figure 2.3	Unit cell volumes of the $LnBaMn_2O_{5+\delta}$ phases (normalized to $Z = 2$) as a function of Ln^{3+} ionic radius.	25
Figure 2.4	Thermogravimetric analysis of $LnBaMn_2O_{5+\delta}$ ($Ln = Y, Gd, Eu, Sm, Nd$ and Pr) compounds under: (a) oxygen, (b) air, (c) nitrogen, and (d) 1.99% H_2/Ar .	27
Figure 3.1	An electrochemical cell for Coulometric titration.	44
Figure 3.2	The complete apparatus of Coulometric titration: (1) a titration cell, (2) thermocouple, (3) quartz tube, (4) metal frame, (5) gas out, (6) Pt wires, (7) spring, (8) gas in, (9) furnace.	44
Figure 3.3	The pO_2 dependence of oxygen non-stoichiometry measured on reduction and re-oxidation of $YBaMn_2O_{5+\delta}$ at (a) 650 °C, (b) 700 °C, and (c) 750 °C.	49

Figure 3.4	The temperature dependence of pO_2 corresponding to the transitions from O_5 to $O_{5.5}$ and $O_{5.5}$ to $O_{5.5+\delta}$ for $YBaMn_2O_{5+\delta}$.	50
Figure 3.5	Equilibrium times as a function of non-stoichiometry for $YBaMn_2O_{5+\delta}$ at 650 °C.	52
Figure 3.6	X-ray data for $YBaMn_2O_{5+\delta}$ collected after re-oxidation by Coulometric titration at 750 °C, compared with the X-ray diffraction patterns of $2H-BaMnO_3$ and $YMnO_3$ obtained from the ICSD database.	54
Figure 3.7	The dependence of oxygen non-stoichiometry on pO_2 measured on reduction at different temperatures for $GdBaMn_2O_{5+\delta}$.	55
Figure 3.8	The temperature dependence of pO_2 corresponding to the transitions from O_5 to $O_{5.5}$ and $O_{5.5}$ to $O_{5.5+\delta}$ for $GdBaMn_2O_{5+\delta}$.	56
Figure 3.9	Equilibrium times as a function of oxygen non-stoichiometry at 650 °C for $GdBaMn_2O_{5+\delta}$. The criterion for equilibrium was $0.005\% \text{ min}^{-1}$.	59
Figure 3.10	(a) The oxygen non-stoichiometry of $GdBaMn_2O_{5+\delta}$ as a function of pO_2 obtained on reduction/oxidation at 700 °C in the initial experiments; (b) Equilibrium times as a function of oxygen non-stoichiometry at 700 °C. The criterion for equilibrium was $0.008\% \text{ min}^{-1}$.	60
Figure 3.11	X-ray data for $GdBaMn_2O_{5+\delta}$ collected after re-oxidation by Coulometric titration at 700 °C, and the corresponding data for $2H-BaMnO_3$ and $GdMnO_3$ obtained from the ICSD database.	61

- Figure 3.12** The pO_2 dependence of oxygen non-stoichiometry in the low- pO_2 region for $PrBaMn_2O_{5+\delta}$ measured on reduction at different temperatures. 63
- Figure 3.13** The temperature dependence of pO_2 corresponding to the transitions from O_5 to $O_{5.5}$ for $PrBaMn_2O_{5+\delta}$. The data were measured on reduction. 63
- Figure 3.14** Equilibrium times as a function of oxygen non-stoichiometry at 650 °C for $PrBaMn_2O_{5+\delta}$. The criterion for equilibrium was $0.005\% \text{ min}^{-1}$. 65
- Figure 3.15** The variation of pO_2 at the transition from O_5 to $O_{5.5}$ for $LnBaMn_2O_{5+\delta}$ ($Ln = Y, Gd, \text{ and } Pr$) with (a) temperature, and (b) the Ln^{3+} ($CN = 8$) ionic size at different temperatures. 67
- Figure 3.16** Partial molar free energy of oxygen atom ($\Delta\mu_o$) as a function of oxygen content for (a) $YBaMn_2O_{5+\delta}$, (b) $GdBaMn_2O_{5+\delta}$, and (c) $PrBaMn_2O_{5+\delta}$ at 600, 650, 700, and 750 °C. 69
- Figure 3.17** The relation between (a) $R/2 \cdot \ln(pO_2)$ and $1/T$, and (b) between $RT/2 \cdot \ln(pO_2)$ and T of $YBaMn_2O_{5+\delta}$ in low- pO_2 region. 71
- Figure 4.1** Sample arrangement for the electrical conductivity experiments; L is the distance between two inside electrodes, A is the applied current, V is the measured voltage across the sample. 81
- Figure 4.2** (a) A gas-tight electrochemical cell for electrical conductivity experiments; (b) a photograph of a complete cell. 82

Figure 4.3	X-ray data for the YBaMn ₂ O ₅ pellet sintered at 1300 °C for 24 h in 10 ppm H ₂ /N ₂ .	86
Figure 4.4	SEM images showing the microstructures of the fresh YBaMn ₂ O ₅ bar: (a) at the polished surface, and (b) on the cross-sectional area.	87
Figure 4.5	The electrical conductivity of YBaMn ₂ O ₅ in low-pO ₂ region (a) in 500-750 °C on both increasing and decreasing temperature, (b) in 610-750 °C on increasing temperature, and (c) in 570-750 °C on decreasing temperature.	87
Figure 4.6	SEM images of (a-b) surface, and (c-d) cross-section of YBaMn ₂ O ₅ microstructure after the electrical conductivity experiments in low pO ₂ atmosphere.	90
Figure 4.7	EDS spectrum of the YBaMn ₂ O ₅ surface after the long-time electrical conductivity experiments.	90
Figure 4.8	Thermal expansion data for YBaMn ₂ O ₅ as function of temperature in 1.99% H ₂ /Ar, calculated from the cubic root of unit cell volume.	92
Figure 4.9	Thermal expansion behavior of YBaMn ₂ O ₅ in 25-900 °C temperature range in 1.99% H ₂ /Ar, obtained by dilatometry experiments.	94
Figure 4.10	Thermal expansion behaviors of YBaMn ₂ O _{5.5} in N ₂ in the temperature range of 25-800 °C, obtained by dilatometry experiments.	95

Figure 4.11	XRD data for YBaMn ₂ O ₆ recorded during heating up to 800 °C in static air and cooling down to room temperature. The asterisk (*) signs indicate Pt peaks from the Pt sample holder.	97
Figure 4.12	Thermal expansion data for YBaMn ₂ O ₆ as function of temperature in static air at 25-800 °C, obtained from the high-temperature X-ray diffraction studies.	99
Figure 4.13	Thermal expansion behavior of YBaMn ₂ O ₆ from 25-830 °C in air obtained by dilatometry.	100
Figure 4.14	DSC curves of YBaMn ₂ O ₆ measured with a heating/cooling rate of 10 °C/min in (a) static air, and (b) nitrogen.	101
Figure 4.15	DSC curves of LnBaMn ₂ O ₆ with (a) Ln = Sm, and (b) Ln = Nd, measured under nitrogen flow with a heating/cooling rate of 10 °C/min.	103

List of Tables

Table 1.1	Typical values of electrical conductivity.	7
Table 2.1	Structure type, oxygen storage capacity (OSC) and oxygen uptake/release conditions of some oxygen storage materials.	14
Table 2.2	The nitrogen-annealing conditions for preparing half-reduced $\text{LnBaMn}_2\text{O}_{5+\delta}$ ($\delta = 0.5$) compounds for $\text{Ln} = \text{Y, Gd, Eu, and Sm}$.	18
Table 2.3	$\text{LnBaMn}_2\text{O}_{5+\delta}$ ($\text{Ln} = \text{Y, Gd, Eu, Sm, Nd, and Pr}$) summary: ionic radius of Ln^{3+} (CN = 8), excess oxygen content (δ) determined by iodometric titration, and structural parameters.	24
Table 2.4	Oxygen storage properties of $\text{LnBaMn}_2\text{O}_{5+\delta}$ ($\text{Ln} = \text{Y, Gd, Eu, Sm, Nd, and Pr}$) compounds.	29
Table 3.1	Composition ranges of each phase and the $p\text{O}_2$ of phase inter-conversion in $\text{YBaMn}_2\text{O}_{5+\delta}$ at 650, 700 and 750 °C.	51
Table 3.2	Composition ranges of each phase and the $p\text{O}_2$ of phase inter-conversion in $\text{GdBaMn}_2\text{O}_{5+\delta}$ at 600, 650, 700 and 750 °C.	57
Table 3.3	Composition ranges of each phase and the $p\text{O}_2$ of phase inter-conversion in $\text{PrBaMn}_2\text{O}_{5+\delta}$ at 600, 650, 700 and 750 °C in low- $p\text{O}_2$ region.	62
Table 3.4	Partial molar free energy of oxygen atom ($\Delta\mu_{\text{O}}$) in low and high- $p\text{O}_2$ regions for $\text{LnBaMn}_2\text{O}_{5+\delta}$ ($\text{Ln} = \text{Y, Gd, and Pr}$) at different temperatures.	70

Table 3.5	A comparison of the values of the change in enthalpy (Δh_0) and entropy (Δs_0) for $\text{LnBaMn}_2\text{O}_{5+\delta}$ ($\text{Ln} = \text{Y, Gd, and Pr}$) in low and high- $p\text{O}_2$ regions.	71
Table 4.1.	Temperature dependences of the unit cell parameters, and volume of YBaMn_2O_5 determined by high-temperature XRD in 1.99% H_2/Ar .	92
Table 4.2	Thermal evolution of the space group, the unit cell parameters, and the cubic root of the unit cell volume of YBaMn_2O_6 (normalized $Z= 1$), obtained from high-temperature XRD studies in static air.	98
Table 4.3	Transition temperature for $\text{LnBaMn}_2\text{O}_6$ ($\text{Ln} = \text{Y, Gd, Eu, Sm, Nd, and Pr}$), obtained from the DSC curves upon heating (H) and cooling (C) processes.	102

List of Symbols and Abbreviations

XRD	X-ray diffraction
SXRD	Synchrotron X-ray diffraction
TEC	Thermal-expansion coefficient
DSC	Differential scanning calorimetry
SEM	Scanning electron microscope
EDS	Energy dispersive spectroscopy
SOFC	Solid-oxide fuel cell
OSM	Oxygen-storage material
OSC	Oxygen-storage capacity
LN	Lanthanides
TGA	Thermogravimetric analysis
CN	The coordination number
YSZ	Ytria-stabilized zirconia
DC	Direct current
CO	Charge ordering
MI	Metal-insulator
AF	Antiferromagnetic
AFM	Antiferromagnetic metal
PM	Paramagnetic metal
FM	Ferromagnetic metal
t	The tolerance factor

r_i	Ionic radii of species i
σ_i	Conductivity of species i
μ	Mobility
E_a	Activation energy
R	The gas constant
G	Gibbs function
H	Enthalpy
S	Entropy
T	Temperature
K	The equilibrium constant
E	Cell potential
F	The Faraday constant
U	Internal energy
μ_i	Chemical potential of species i
μ°	Chemical potential at the standard state
h_i	Partial molar enthalpy of species i
s_i	Partial molar entropy of species i
pO_2	The oxygen partial pressure
δ	Excess oxygen content
i	Current
Δn_{O_2}	Number of moles of oxygen
M	Molecular weight
W	Weight of the sample

C	Concentration
J_o	oxygen leakage flux
δ_{bulk}	The bulk density
ΔV	The difference of measured voltage
α_L	The linear thermal expansion coefficient

CHAPTER 1

Introduction

1.1 Objective

The objective of this work is to investigate the crystal structures, oxygen non-stoichiometry and oxygen uptake/release behavior of the A-site double-perovskite oxides $\text{LnBaMn}_2\text{O}_{5+\delta}$ ($\text{Ln} = \text{Y, Gd, Eu, Sm, Nd, and Pr}$), and to study the electrical conductivity and thermal expansion of $\text{YBaMn}_2\text{O}_{5+\delta}$.

1.2 Scope of the thesis

Chapter 1 provides the theoretical background for oxygen non-stoichiometry and electrical conductivity in the perovskite oxides. The structural aspects, the defect chemistry relevant to the materials in this thesis, and thermodynamic properties are discussed.

Chapter 2 describes the synthesis of the double-perovskite oxides $\text{LnBaMn}_2\text{O}_{5+\delta}$ ($\text{Ln} = \text{Y, Gd, Eu, Sm, Nd, and Pr}$) via solid-state reaction, and the investigation of the crystal structures of the compounds using X-ray diffraction. The oxygen uptake/release behavior of the $\text{LnBaMn}_2\text{O}_{5+\delta}$ oxides ($\text{Ln} = \text{Y, Gd, Eu, Sm, Nd, and Pr}$), and the effect of A-site cationic substitution on the oxidation/reduction characteristics were studied by using thermogravimetry analysis.

Chapter 3 presents a study of the oxygen non-stoichiometric behavior of the $\text{LnBaMn}_2\text{O}_{5+\delta}$ ($\text{Ln} = \text{Y, Gd, and Pr}$) oxides by using solid-state Coulometric titration. The dependence of the oxygen non-stoichiometry (δ) on temperature, oxygen partial pressure

(pO_2) and A-site cationic substitution were investigated. The kinetic data and thermodynamic quantities under near-equilibrium conditions were determined.

Chapter 4 describes fabrication of dense pellets of $YBaMn_2O_5$, and the electrical conductivity behavior at high temperature of $YBaMn_2O_5$ measured using the four-probe DC method in an electrochemical cell. The linear thermal expansion of $YBaMn_2O_{5+\delta}$ was examined by dilatometry and high-temperature XRD experiments, and the behavior of the thermal-expansion coefficients (TECs) are discussed. The phase transitions of the $LnBaMn_2O_{5+\delta}$ ($Ln = Y, Gd, Eu, Sm, Nd, \text{ and } Pr$) oxides were examined at high temperatures by using differential scanning calorimetry (DSC).

Finally, the key conclusions from all experiments and suggestions for future research are presented in Chapter 5.

1.3 The Perovskite Structure

Perovskites are a large family of compounds with closely related crystal structures and are one of the most-important structure types in the solid-state sciences. The general formula of perovskite is ABX_3 , in which A and B are cations, and X is usually oxygen or fluorine. $CaTiO_3$, $SrTiO_3$, and $BaTiO_3$ are representative materials with the perovskite structure [1]. The perovskite oxides (ABO_3) have a wide variety of interesting physical properties, which are useful in various technological applications such as solid oxide fuel cells (SOFCs), oxidation catalysis, oxygen sensors, and others [2-3]. Figure 1.1 illustrates the ideal primitive cubic ABO_3 perovskite structure, which consists of corner-sharing BO_6 octahedra with the large A-cation occupying the body-center and 12-coordinated by

oxygen-atom positions [4]. The stability of the ABO_3 perovskite structure is related to the Goldschmidt tolerance factor (t) [5]:

$$t = \frac{r_A + r_O}{\sqrt{2} \cdot (r_B + r_O)} \quad (1.1)$$

where, r_A , r_B , and r_O are the ionic radii of the A-site, B-site cations, and the oxygen ion, respectively. The ionic radii were summarized by Shannon [6]. Geometrically, the ideal perovskite structure should have $t = 1.0$ or very close to one. In practice, there is some flexibility over bond lengths. The ABO_3 perovskite structure is generally stable between $0.75 < t < 1.06$ [7].

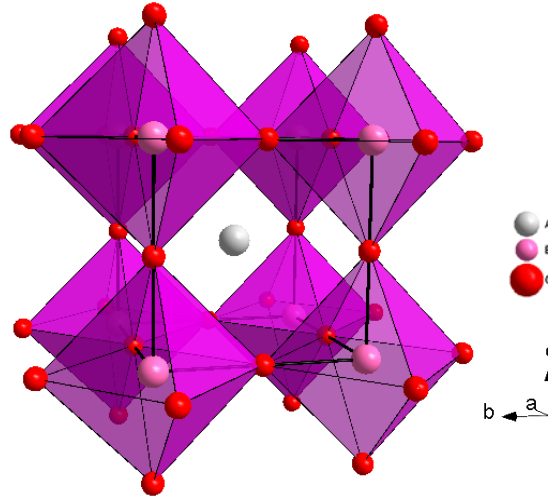


Fig. 1.1 The ideal ABO_3 perovskite structure

1.4 Theoretical Background

The defect chemistry, non-stoichiometry, and thermodynamics relevant to the application of the double-perovskites $LnBaMn_2O_{5+\delta}$ ($Ln = Y, Gd, Eu, Sm, Nd, \text{ and } Pr$) as oxygen-storage materials are reviewed below as background to the experimental methods.

1.4.1 Defect Chemistry and Non-stoichiometry

A perfect crystal, in which all the atoms are at rest on their correct lattice positions, can be hypothetically obtained only at absolute zero temperature. At all real temperatures, crystals are imperfect with presence of defects. Van Roosmalen *et al.* reported three types of non-stoichiometric behaviors to explain the defect chemistry of the perovskite-type oxides [8]. The first type was developed by Frenkel, Schottky, and Wagner [9-10]. The defect concentrations are very small and only point defects occur near the stoichiometric region. The second type is the region of extended defects and microdomains. It was suggested that interaction between points defects generally occurs at defect concentrations exceeding 0.1 at% [11]. Furthermore, depending on the nature of the extended defects, at a particular concentration the extended defects will interact themselves, leading to formation of highly defective ordered phases, that is, the third type of non-stoichiometric behavior. Temperature, pO_2 , and defect concentrations have an important influence on these behaviors.

In ABO_3 perovskite structure, a fraction of dopant, usually a divalent cation, can be introduced into the A-site creating cation deficiency or oxygen deficiency, and resulting in the non-stoichiometry of perovskite oxides. Oxygen deficiency is more common in perovskites, and leads to the formation of oxygen vacancies ($V_O^{\bullet\bullet}$) in the crystal structure having effective positive charges with respect to the lattice.

Defect modelling is used to better illustrate the defect chemistry of the perovskite oxides. A defect model of $La_{1-x}Sr_xFeO_{3-\delta}$ system related to the point defects was developed by Mizusaki *et al.* [12]. The major defects in $La_{1-x}Sr_xFeO_{3-\delta}$ are $V_O^{\bullet\bullet}$, Sr'_{La} , Fe'_{Fe} , and Fe_{Fe}^{\bullet} . In Kröger and Vink notation [13], M_S^C means species M which can be

atom, vacancy, electron or electron hole, located at S lattice site with C net electronic charge. One positive excess charge is represented by a dot (\cdot), one negative excess charge is by a prime ($'$), and neutral is by a cross (\times). Under oxidizing atmospheres, the relation $[Fe_{Fe}^{\cdot}] \gg [Fe_{Fe}']$ holds, while in a reducing atmosphere, $[Fe_{Fe}^{\cdot}] \ll [Fe_{Fe}']$. The electroneutrality condition for the defects in the solid solution is given by:

$$[Sr'_{La}] + [Fe'_{Fe}] = 2[V_{O}^{\cdot\cdot}] + [Fe_{Fe}^{\cdot}] \quad (1.2)$$

The value of $[Sr'_{La}]$ is given by the nominal A-site composition x , that is, $[Sr'_{La}] = x$. Because this solid solution is an oxygen deficient type, we have $[V_{O}^{\cdot\cdot}] = \delta$. Thus, the electroneutrality condition is expressed by: $x + [Fe'_{Fe}] = 2\delta + [Fe_{Fe}^{\cdot}]$, and in an oxidizing atmosphere this condition can be simplified to:

$$x \cong 2\delta + [Fe_{Fe}^{\cdot}] \quad (1.3)$$

With decreasing oxygen partial pressure (pO_2), $[Fe_{Fe}^{\cdot}]$ becomes sufficiently low so that $x \cong 2\delta$. In a reducing atmosphere, the electroneutrality condition can be simplified to:

$$x + [Fe'_{Fe}] \cong 2\delta. \quad (1.4)$$

The Fe^{3+} ions (Fe_{Fe}^{\times}) disproportionate into Fe^{2+} (Fe'_{Fe}) and Fe^{4+} (Fe_{Fe}^{\cdot}). The reaction between oxygen gas and defects in $La_{1-x}SrFeO_{3-\delta}$ is expressed as follow:

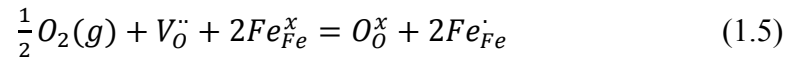


Figure 1.2 shows a diagram of the defect concentration as a function of $\log pO_2$ reported by Mizusaki *et al.* [12]. The plateau in Region II corresponds to $\delta \cong x/2$. At the minimum $\partial\delta/\partial \log pO_2$ in Region II, the stoichiometric composition holds for the electronic defects, that is, $Fe_{Fe}^{\cdot} = Fe'_{Fe}$. The electroneutrality conditions for Region I and Region III are given by eqn. (1.3) and (1.4), respectively.

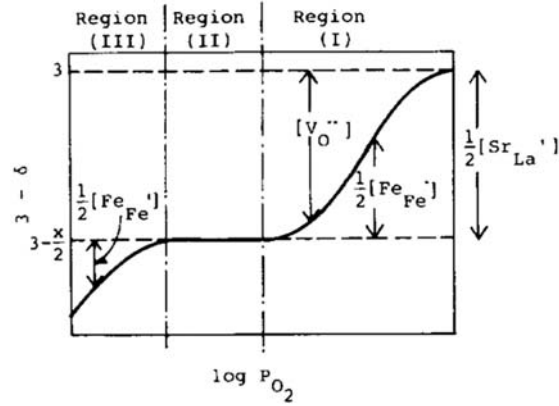
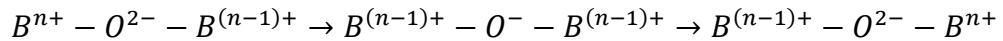


Fig. 1.2 A schematic diagram for the concentrations of the defects $[V_O^{..}]$, $[Sr'_{La}]$, $[Fe'_{Fe}]$, and $[Fe_{Fe}]$ as a function of $\log p_{O_2}$ for $La_{1-x}SrFeO_{3-\delta}$ [12].

In addition, the conductivity in ABO_3 perovskite can be explained by the point defect chemistry. The ionic and electronic conductivity are based on $V_O^{..}$ and h^{\cdot} , respectively [14]. The ionic conductivity is mainly related to the crystal structure which should provide pathway for ion movements, whereas the electronic conductivity depends more on the properties of the ions in the compounds and determined by the electronic bandgap. Electronic conductivity in ABO_3 is considered to occur by electron hopping, which is due to the overlap between the filled 2p orbitals of oxygen and neighboring empty or partially filled d-orbitals of the transition B cations [15]. The hopping mechanism is schematically written as following [16-17]:



1.4.2 Electrical Conductivity

The electrical properties of materials are categorized into several groups as summarized in Table 1.1. This study only focuses on oxygen ionic conduction and electronic conduction in mixed conducting oxides.

Table 1.1 Typical values of electrical conductivity [10].

	Material	σ (Scm⁻¹)
Ionic conduction	Ionic crystals	$<10^{-18} - 10^{-4}$
	Solid electrolytes	$10^{-3} - 10^1$
	Strong (liquid) electrolytes	$10^{-3} - 10^{-1}$
Electronic conduction	Metals	$10^{-1} - 10^5$
	Semiconductors	$10^{-5} - 10^2$
	Insulators	$<10^{-12}$

The conductivity (σ) is generally expressed in terms of the number of current-carriers (n), their charge (e), and their mobility (μ) according to:

$$\sigma = ne\mu \quad (1.6)$$

In metals, the number of the mobile electrons is large and essentially constant, but their mobility decreases with increasing temperature due to electron-phonon collisions. Consequently, the conductivity gradually decreases as the temperature increases. In semiconductors, the number of mobile electrons is not as large as in metals. This number may be increased, either by doping with impurities that provide electrons or holes, or by increasing the temperature to promote more electrons from the valence band to the conduction band. With increasing temperature, the number of mobile electrons increases following [10]:

$$n = n_0 \exp(-E/kT) \quad (1.7)$$

where, n_0 is a constant (the total number of electrons), E is the activation energy or promotion energy, k is Boltzmann's constant, T is temperature (in K).

The total conductivity of (σ_T) of mixed conducting oxides is given by the sum of ionic conductivity and electronic conductivity as follows [18]:

$$\sigma_{Total} = \sigma_{ionic} + \sigma_{electronic} \quad (1.8)$$

where electronic carriers are electrons and holes, and ionic charge carriers are typically anionic or cationic defects. In mixed conductors, the total conductivity is usually predominantly given by electronic contribution with negligible ionic conductivity, although the concentration of ionic carriers is much higher than that of electronic ones. This is because electronic mobility is at least three orders of magnitude greater than ionic mobility.

The total conductivity is also defined as $\sigma_T = R^{-1}$, and plotted against reciprocal temperature in Arrhenius model [19]:

$$\sigma_T = A \cdot \exp\left(-\frac{E_a}{RT}\right) \quad (1.9)$$

where, A is the pre-exponential factor, E_a is the activation energy, and R is the gas constant. The activation energy can be extracted from the slope of $\log \sigma_T$ vs. $1/T$ plot. The unit of conductivity and activation energy are $S \text{ cm}^{-1}$ and eV (or kJ mol^{-1}), respectively.

1.4.3 Thermodynamic Quantities

The Gibbs function (G) is defined as $G = H - TS$, where H , S , and T are the enthalpy, entropy, and temperature (in K) of the system, respectively. The Gibbs function gives information about whether a reaction will proceed spontaneously at constant temperature and pressure. When $(dG)_{T,P} \leq 0$ at constant temperature and pressure, the chemical reactions occur spontaneously in the direction of decreasing Gibbs energy. The Gibbs function can be expressed by various forms as [10, 20]:

$$\Delta G = \Delta H - T\Delta S \quad (1.10)$$

$$\Delta G = \Delta G^\circ + RT \ln K \quad (1.11)$$

$$\Delta G = -nFE \quad (1.12)$$

where, K is the equilibrium constant, E is the cell potential, n is number of moles of electrons transferred in the reaction, and F is Faraday constant.

When there are infinitesimal changes of the state in the system, G may change due to changes of H , S , and T as follows: $dG = dH - T \cdot dS - S \cdot dT$. As $H = U + pV$, where U , p , and V are the internal energy, pressure, and volume of the system, respectively, $dH = dU + p \cdot dV + V \cdot dp$. Thus, for a closed system in which there is no change of composition and no P - V work, dG is given as following:

$$dG = V \cdot dp - SdT \quad (1.13)$$

At constant temperature, eqn. (1.13) can be reduced to $\left(\frac{\partial G}{\partial p}\right)_T = V$. Since the molar volume of gases strongly depends on p , V can be substituted by nRT/p for an ideal gas. Therefore,

$$\mu = \mu^\circ + RT \cdot \ln(p/p^\circ) \quad (1.14)$$

where, $\mu = G(p)/n$ is the chemical potential, and μ° is the chemical potential at the standard state, $p^\circ = 1$ atm.

In an open system, the variations in composition may occur, and the Gibbs function varies with composition. Consequently, $G = G(p, T, n_1, n_2, \dots, n_j)$, where n_1, n_2, \dots, n_j are the number of moles for the component 1, 2, \dots, j . At constant p and T , a change of G is given as below:

$$dG = \sum_j \left(\frac{\partial G}{\partial n_j} \right)_{p, T, n_1, n_2, \dots, n_{j-1}, n_{j+1}} \cdot dn_j \quad (1.15)$$

From eqn. (1.15), the partial molar Gibbs free energy of a j -component is defined by its chemical potential as the following:

$$\mu_j = \left(\frac{\partial G}{\partial n_j} \right)_{p,T,n_1,n_2,\dots,n_{j-1},n_{j+1}} \quad (1.16)$$

The chemical potential (μ_j) provides the information about how the overall free energy of a mixture changes when a j -component is added to the system, and depends on the composition, T , and p of the system.

The chemical potential of oxygen (μ_{O_2}) in solid oxides can be defined by using the oxygen partial pressure (pO_2) in the surrounding gas. When an oxide is in equilibrium with a certain pO_2 in the surrounding gas, the chemical potential of oxygen in solid phase is equal to that in the gas phase as below [21]:

$$\mu_{O_2,solid} = \mu_{O_2,gas} = \mu^{\circ}_{O_2,gas} + RT \cdot \ln pO_2 \quad (1.17)$$

where, $\mu_{O_2,solid}$ and $\mu_{O_2,gas}$ are the chemical potentials of oxygen in the solid and in the gas phase, respectively, and $\mu^{\circ}_{O_2,gas}$ is the chemical potential of the gas in the standard state, $pO_2 = 1$ atm. Since the equilibrium pO_2 of the surrounding gas at a specific oxygen stoichiometry (δ) is obtained from the experiments, the partial molar free energy of oxygen in the solid can be determined by using eqn. (1.17). The values of the chemical potential of oxygen in the gas phase in the standard state ($\mu^{\circ}_{O_2,gas}$) are temperature dependent, and were reported by Lankhorst *et al.* [21] as follows:

$$\mu^{\circ}_{O_2,gas} = RT \left[n_1 + n_2 \cdot \frac{1}{T} + n_3 \cdot \ln(T) + n_4 \cdot \ln \left\{ 1 - \exp \left(-\frac{n_5}{T} \right) \right\} \right] \quad (1.18)$$

where, $n_1 = -1.225$, $n_2 = -1.045 \times 10^3$ K, $n_3 = -3.500$, $n_4 = 1.013$, and $n_5 = 2.242 \times 10^3$ K.

The partial molar enthalpy (h_{O_2}) and the partial molar entropy (s_{O_2}) of oxygen can be calculated from the temperature dependence of μ_{O_2} using the Gibbs-Helmholtz relation, as given below [22]:

$$s_{O_2} = -\frac{\partial \mu_{O_2}}{\partial T} \quad (1.19)$$

$$h_{O_2} = \frac{\partial(\mu_{O_2}/T)}{\partial(1/T)} \quad (1.20)$$

And, the h_{O_2} can be calculated by using the relation: $\mu_{O_2} = h_{O_2} - Ts_{O_2}$ when s_{O_2} is known from eqn. (1.19), and vice versa.

1.5 References

1. Muller, U., *Inorganic Structural Chemistry*. 2nd ed.; Wiley Press: 1992.
2. Bhalla, A. S.; Guo, R.; Roy, R. *Mater. Res. Innovations* **2000**, *4*, 3-26.
3. Zhu, L.; Ran, R.; Tadé, M.; Wang, W.; Shao, Z. *Asia-Pac. J. Chem. Eng.* **2016**, *11*, 338-369.
4. Darriet, J.; Subramanian, M. A. *J. Mater. Chem.* **1995**, *5* (4), 543-552.
5. Goldschmidt, V. M. *Akad. Oslo.* **1946**, *A42*, 224.
6. Shannon, R. D. *Acta Cryst.* **1976**, *A 32*, 751-767.
7. Maier, J. **1993**, *76*, 1212-1217.
8. Roosmalen, J. M. A. V.; Cordfunke, E. H. P. *J. Solid State Chem.* **1991**, *93*, 212-219.
9. Wagner, J. B.; Wagner, C. *J. Chem. Phys.* **1957**, *26* (6), 1597-1601.
10. West, A. R., *Basic Solid State Chemistry*. 2nd ed.; Wiley Press: 1999.
11. Mrowec, S. *Ceramurgia Int.* **1978**, *4*, 47.
12. Mizusaki, J.; Yoshihiro, M.; Yamauchi, S.; Fueki, K. *J. Solid State Chem.* **1985**, *58*, 257-266.

13. Kroger, F. A.; Vink, H. J. *Solid State Physics* **1956**, *3*, 307.
14. Sengodan, S.; Kim, J.; Shin, J.; Kim, G. *J. Electrochem. Soc.* **2011**, *158* (11), B1373-B1379.
15. Mizusaki, J.; Hasegawa, M.; Yashiro, K.; Matsumoto, H.; Kawada, T. *Solid State Ionics* **2006**, *177*, 1925-1928.
16. Zener, C. *Phys. Rev.* **1951**, *82* (3), 403-405.
17. Rupasov, D. Oxygen Diffusion Studies in Mixed Ionic Electronic Conducting Compounds. Ph.D. Dissertation, University of Houston, Houston, TX, USA, 2014.
18. Dieckmann, R. *Solid State Ionics* **1984**, *12*, 1.
19. Stevenson, J. W.; Armstrong, T. R.; Carneim, R. D.; Pederson, L. R.; Weber, W. *J. J. Electrochem. Soc.* **1996**, *143* (9), 2722.
20. Kosuge, K., *Chemistry of Non-stoichiometric compounds*. Oxford University Press: Oxford, 1994.
21. Lankhorst, M. H. R.; Bouwmeester, H. J. M.; Verweij, H. *J. Solid State Chem.* **1997**, *133*, 555-567.
22. Park, C. Y. The Electrical Conductivity Behavior of Perovskite Metal Oxides at High Temperature. Ph.D. Dissertation, University of Houston, Houston, TX, USA, 2003.

CHAPTER 2

Synthesis, Crystal Structure and Oxygen-Storage Properties of the Double-Perovskites $\text{LnBaMn}_2\text{O}_{5+\delta}$ (Ln = Y, Gd, Eu, Sm, Nd, and Pr)

2.1 Introduction

Non-stoichiometric oxides which show rapid and reversible oxygen uptake/release behavior at moderate temperatures are called oxygen-storage materials (OSMs). These materials have recently attracted interest for a wide range of oxygen-related applications in which a precise control of oxygen partial pressure ($p\text{O}_2$) in redox reactions is required, for example in automotive-exhaust catalysts, oxygen enrichment, oxygen separation, catalytic oxidation of hydrocarbons, electrodes in solid oxide electrolysis cells and fuel cells, as well as for oxy-fuel and chemical looping combustion processes used for air separation, clean coal combustion, and syngas production via the partial oxidation of methane [1-24].

An ideal oxygen-storage material should have the following properties: 1) a large oxygen-storage capacity (OSC) stored as mobile oxygen ions in the crystal lattice; 2) fast and reversible oxygen uptake/release processes over a narrow temperature range; 3) adequate phase stability under operating conditions; 4) sufficiently low operating temperature [14, 25]. The best known and most widely used OSMs are the fluorite structure $\text{Ce}_{1-x}\text{Zr}_x\text{O}_{2-\delta}$ oxides with oxygen-storage capacities as high as $\sim 1500 \mu\text{mol-O/g}$ [26]. Ceria-zirconia compositions have been evaluated for three-way catalysts, air separation, selective oxidation of methane, and solar thermochemical water splitting [23, 27-32]. The properties of a number of other oxides have been investigated recently as

candidate materials for oxygen storage with reference to the criteria outlined above. Some of these materials along with their cycling conditions are given in Table 2.1. Of these, $\text{YBaCo}_4\text{O}_{7+\delta}$ has a markedly higher oxygen-storage capacity than that of the $\text{Ce}_{1-x}\text{Zr}_x\text{O}_{2-\delta}$, but decomposes on heating in an oxygen-containing atmosphere above 600 °C. Its phase stability can be improved by partial substitution of Co with Al and Ga, though with a decrease in the oxygen-storage capacity [25].

Table 2.1 Structure type, oxygen-storage capacity (OSC) and oxygen uptake/release conditions of some oxygen-storage materials.

Compound	Type of structure	OSC ($\mu\text{mol-O/g}$)	Temperature and atmosphere for oxygen uptake/release processes
$\text{Ce}_{1-x}\text{Zr}_x\text{O}_{2-\delta}$ [26]	Fluorite	~1500	Oxidation in 50% O_2/N_2 and reduction in 20% H_2/N_2 at 500 °C
$\text{YBaCo}_4\text{O}_{7+\delta}$ [33]	Hexagonal	~2700	Oxidation in 100 atm O_2 at 200~390 °C and reduction in N_2 at 350 °C
$\text{Dy}_{0.7}\text{Y}_{0.3}\text{MnO}_{3+\delta}$ [34]	Hexagonal	1200	Oxygen uptake at 200-300 °C and release at 275-375 °C in O_2
$\text{Ca}_2\text{AlMnO}_{5+\delta}$ [3]	Brownmillerite	~1900	Reversible oxygen intake/release at 500~700 °C in O_2
$\text{LuFe}_2\text{O}_{4+x}$ [35]	Layered structure of alternating $[\text{LuO}_2]$ and $[\text{Fe}_2\text{O}_4]$ layers	~1400	Oxidation at 200-500 °C under an oxygen pressure of $\sim 2 \times 10^{-4}$ atm and reduction in H_2 from 500 °C
$\text{La}_{1-x}\text{Sr}_x\text{FeO}_{3+\delta}$ [19]	Perovskite	1400	Oxidation in air and reduction in 15% methane at 600-835 °C
$\text{La}_{0.5}\text{Sr}_{0.5}\text{Co}_{0.5}\text{Fe}_{0.5}\text{O}_{3-\delta}$ [21]	Perovskite	2200	Oxidation in air and reduction in 5% H_2/Ar at 500 °C
$\text{YBaMn}_2\text{O}_{5+\delta}$ [36]	Double Perovskite	~2400	Oxidation at 200~390 °C in O_2 and reduction at 200~490 °C under 5% $\text{H}_2/95\%$ Ar atmosphere

As reported by Motohashi *et al.* [36], the double-perovskite YBaMn₂O₅-YBaMn₂O₆ system has the next-highest oxygen-storage capacity reaching ~2400 μmol-O/g (3.75 wt. %) during change of the atmosphere between O₂ and 5% H₂/95% Ar, and show good reversible oxygen uptake/release characteristics with fast kinetics below 500 °C. The cyclic performance of YBaMn₂O_{5+δ} upon switching the atmosphere between O₂ and 5% H₂/95% Ar at 500 °C showed no detectable decrease in efficiency after 100 cycles. YBaMn₂O_{5+δ} also has significant catalytic activity for combustion of hydrocarbons. Based on this previous work, YBaMn₂O_{5+δ} may be useful in chemical looping technology, oxygen separation, and for oxidation reactions.

The structure of YBaMn₂O_{5+δ} can be described as an A-site ordered double-perovskite with layers of smaller yttrium and larger barium ions in the A-site alternating along [100] [37]. This oxide has three distinct phases on oxidation/reduction with $\delta \approx 0$, 0.5 and 1 (i.e. O₅, O_{5.5}, and O₆ phases, respectively), which differ in the occupancy of the oxygen sites within the yttrium-oxygen atom layers as illustrated in Fig. 2.1 [36, 38-40]. Taking into account the structural features of YBaMn₂O_{5+δ}, substitutions of trivalent lanthanides (Ln³⁺) at the yttrium site could be interesting because yttrium neighbors the oxygen active site for oxygen uptake/release processes. In relation to oxygen-storage properties, recent reports on the partially and completely Ln-substituted derivatives (Ln = Er, Dy, Gd, Sm, Nd, and Pr) of YBaMn₂O_{5+δ} indicated that their properties are related to the ionic size of the substituted lanthanides, and the effects of Ln-substitution on the operating temperatures and the kinetics of oxidation/reduction were also discussed [41-48]. Besides, the LnBaMn₂O_{5+δ} (Ln = La, Nd, and Gd) compounds were found to be useful as reductants in thermochemical hydrogen production from water [49].

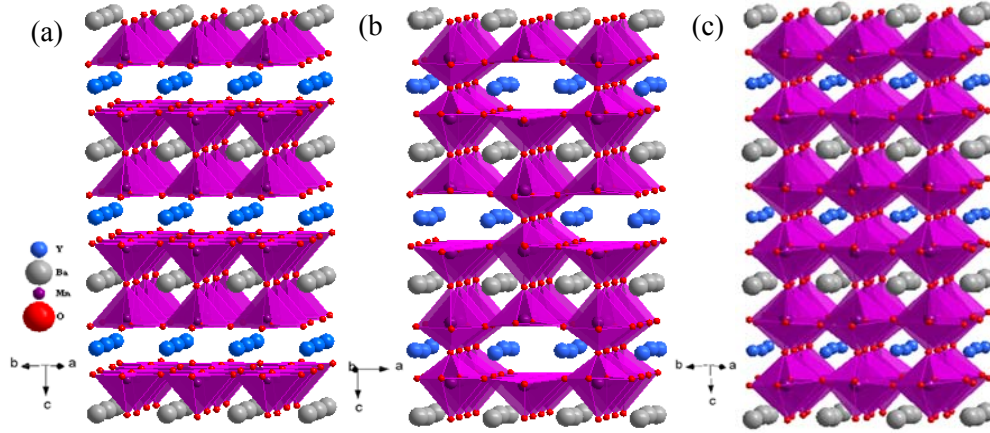


Fig. 2.1 Crystal structures of $\text{YBaMn}_2\text{O}_{5+\delta}$: (a) fully-reduced O_5 phase ($\delta = 0$), (b) half-reduced $\text{O}_{5.5}$ phase ($\delta = 0.5$), and (c) fully-oxidized O_6 phase ($\delta = 1$).

Typically, the $\text{LnBaMn}_2\text{O}_{5+\delta}$ compound system is first synthesized in the fully-reduced $\text{LnBaMn}_2\text{O}_5$ phase which requires a control of the oxygen partial pressure to avoid formation of stable binary phases, $\text{BaMnO}_{3-\delta}$ and LnMnO_3 [38, 50-51]. The fully-oxidized $\text{LnBaMn}_2\text{O}_6$ phase is then obtained by oxidation of O_5 phase in air or oxygen [52]. The electronic phase diagram of $\text{LnBaMn}_2\text{O}_6$ is known for $\text{Ln} = \text{Y}$ and La-Ho lanthanides [53], and recently the synthesis, crystal structure and electrical properties of $\text{ErBaMn}_2\text{O}_5$ and $\text{ErBaMn}_2\text{O}_6$ compounds have been reported [42]. The half-reduced $\text{LnBaMn}_2\text{O}_{5.5}$ phase has been reported for $\text{Ln} = \text{La}$ [54], Y [39-40], Tb [55], Pr [56], and Nd [56-58], but not for the other lanthanides.

In the present work, the double-perovskite $\text{LnBaMn}_2\text{O}_{5+\delta}$ ($\text{Ln} = \text{Y}, \text{Gd}, \text{Eu}, \text{Sm}, \text{Nd}, \text{and Pr}$) compounds were synthesized and studied to clarify the effect of A-site cationic substitution on the oxidation/reduction characteristics. The crystal structure at room temperature was investigated by X-ray diffraction. Thermogravimetric analysis was used to study the oxygen uptake/release behavior of $\text{LnBaMn}_2\text{O}_{5+\delta}$. Some of the data presented in this chapter were already published by Jeamjumnunja *et al.* [59-60].

2.2 Experimental Section

2.2.1 Synthesis of $\text{LnBaMn}_2\text{O}_{5+\delta}$

The fully-reduced double-perovskite $\text{LnBaMn}_2\text{O}_{5+\delta}$ ($\text{Ln} = \text{Y, Gd, Eu, Sm, Nd, and Pr}$) oxides with $\delta \approx 0$ were synthesized *via* a solid-state reaction under low oxygen partial pressure to avoid the formation of the stable oxides, $\text{BaMnO}_{3-\delta}$ and LnMnO_3 [38, 50-52]. BaCO_3 (Aldrich 99.999%), Mn_2O_3 (Aldrich 99%), and oxides of lanthanides; Y_2O_3 (Aldrich 99.99%), Gd_2O_3 (Aldrich 99.9%), Eu_2O_3 (Alfa Aesar 99.9%), Sm_2O_3 (Alfa Aesar 99.9%), Nd_2O_3 (Aldrich 99.9%), and Pr_6O_{11} (Aldrich 99.9%) were used as starting materials. Eu_2O_3 and Nd_2O_3 powders were heated in air at 1000 °C prior to weighing to remove absorbed CO_2 and moisture. As a precursor, stoichiometric mixtures of starting materials were ball-milled in isopropanol for 24 h and then oven-dried at 80 °C for 48 h. About 200 mg of the $\text{LnBaMn}_2\text{O}_{5+\delta}$ ($\text{Ln} = \text{Y and Gd}$) ball-milled precursor was heated in a tube furnace at 1050 °C for 22 h with a heating rate of 5 °C/min under a flow of dry N_2 and a water-saturated 5% H_2 /95% Ar gas mixture ($p_{\text{O}_2} \approx 10^{-12}$ atm), and then rapidly cooled to room temperature. Samples of $\text{LnBaMn}_2\text{O}_{5+\delta}$ ($\text{Ln} = \text{Eu, Sm, and Nd}$) with $\delta \approx 0$ were prepared under a flow of water-saturated 5% H_2 /95% Ar gas ($150 \text{ cm}^3 \text{ min}^{-1}$) at the same heating/cooling conditions as for $\text{Ln} = \text{Y and Gd}$. In case of $\text{PrBaMn}_2\text{O}_{5+\delta}$, the fully-reduced ($\delta \approx 0$) sample was synthesized by heating the precursor at 1000 °C for 17 h in an atmosphere containing ~1% H_2 , obtained by mixing of dry N_2 gas ($120 \text{ cm}^3 \text{ min}^{-1}$) and dry 5% H_2 /95% Ar gas ($30 \text{ cm}^3 \text{ min}^{-1}$), and then rapidly cooled to room temperature. The sample was reheated at the same conditions for two more times with intermediate grinding. The fully-oxidized samples of $\text{LnBaMn}_2\text{O}_{5+\delta}$ ($\text{Ln} = \text{Y, Gd, Eu, Sm, Nd, and Pr}$) with $\delta \approx 1$ were obtained by annealing the $\text{LnBaMn}_2\text{O}_5$ samples at 800 °C for 12 h in

flowing O₂ gas with 2 °C/min heating and cooling rates. The half-reduced samples of LnBaMn₂O_{5+δ} (Ln = Y, Gd, Eu, and Sm) with δ ≈ 0.5 were prepared by annealing the LnBaMn₂O₆ powder under a N₂ atmosphere with 1°C/min heating rate, followed by fast cooling to room temperature (>20 °C/min). The nitrogen-annealing conditions of each sample are summarized in Table 2.2. The preparation of half-reduced PrBaMn₂O_{5+δ} sample (δ ≈ 0.5) was not successful by annealing under N₂ atmosphere, however, it was made by heating a stoichiometric mixture of PrBaMn₂O₅ and PrBaMn₂O₆ powders in an evacuated quartz tube at 800 °C for 18 h. The synthesis of NdBaMn₂O_{5.5} is ongoing and not reported here.

Table 2.2 The nitrogen-annealing conditions for preparing half-reduced LnBaMn₂O_{5+δ} (δ = 0.5) compounds for Ln = Y, Gd, Eu, and Sm.

Ln element in LnBaMn ₂ O _{5+δ}	Nitrogen-annealing condition	
	Temperature (°C)	Time (hour)
Y	700	12
Gd	800	24
Eu	900	15
Sm	900	24

2.2.2 Crystal Structure Analysis

The crystal structure and phase purity of all LnBaMn₂O_{5+δ} (Ln = Y, Gd, Eu, Sm, Nd, and Pr) samples were checked using powder X-ray diffraction in the range 10 ≤ 2θ° ≤ 90 with Cu Kα radiation (λ = 1.54046 Å) on a Phillips PANalytical X’Pert PRO diffractometer at room temperature. The unit cell parameters of the samples were obtained through Le Bail refinement using the GSAS/EXPGUI set of software.

2.2.3 Chemical Analysis

The precise oxygen contents ($5+\delta$) of the $\text{LnBaMn}_2\text{O}_{5+\delta}$ samples were obtained by iodometric titration [39, 61-62]. Approximately 30 mg of the finely ground sample powder was dissolved in 20 ml of 20% KI solution and 2 ml of concentrated HCl under a N_2 atmosphere. The amount of I_2 formed in the reduction reaction of Mn^{3+} and/or Mn^{4+} to Mn^{2+} ion was titrated with 0.02 M $\text{Na}_2\text{S}_2\text{O}_3$ solution in the presence of a starch indicator. Without the sample, the same amount of KI solution and concentrated HCl was used in a control experiment. Oxygen stoichiometry was calculated with the following equation:

$$\delta = \frac{CVM_r}{2000W - 15.9994CV} - 0.5 \quad (2.1)$$

where, W is weight of the double-perovskite sample (g), C is concentration of $\text{Na}_2\text{S}_2\text{O}_3$ solution (mol/L), V is volume of $\text{Na}_2\text{S}_2\text{O}_3$ solution used (ml), and M_r is molecular weight of the double-perovskite sample where all B-cations are in oxidation state of +2 (g/mol).

For each composition, the titrations were performed 3 times with good reproducibility and average oxygen contents were calculated.

2.2.4 Thermogravimetric Analysis (TGA)

The oxygen uptake/release characteristics of the $\text{LnBaMn}_2\text{O}_{5+\delta}$ ($\text{Ln} = \text{Y, Gd, Eu, Sm, Nd, and Pr}$) products were studied by means of thermogravimetric analysis (TA; Hi-Res 2950 thermogravimetric analyzer). The measurements were carried out on ~40 mg of finely ground $\text{LnBaMn}_2\text{O}_{5+\delta}$ powders. For the oxygen uptake study, the samples were heated and then cooled in a platinum sample pan between room temperature and 800 °C at 2 °C/min in flowing O_2 or air. In case of the oxygen-release process, the reduction experiments were investigated in two different atmospheres, N_2 and 1.99% H_2/Ar . The

oxidized $\text{LnBaMn}_2\text{O}_{5+\delta}$ samples obtained from the oxidation experiments were subsequently heated and cooled under a flowing N_2 atmosphere between room temperature and up to 980°C with rates of $2^\circ\text{C}/\text{min}$ and $20^\circ\text{C}/\text{min}$, respectively. For another set of reduction experiments, the samples after oxidation were subsequently heated and cooled in an alumina sample pan between room temperature and 700°C in $1.99\% \text{H}_2/\text{Ar}$ with rates of $2^\circ\text{C}/\text{min}$ and $20^\circ\text{C}/\text{min}$, respectively.

2.3 Results and Discussion

2.3.1 Synthesis and Crystal structure of $\text{LnBaMn}_2\text{O}_{5+\delta}$ at room temperature

The control of the oxygen partial pressure and temperature is known to be a crucial factor for the synthesis of $\text{LnBaMn}_2\text{O}_{5+\delta}$ with $\delta \approx 0$. This oxide is formed only under strong reducing conditions. In this study, the $\text{LnBaMn}_2\text{O}_{5+\delta}$ ($\delta \approx 0$) samples were synthesized by solid-state reaction in an atmosphere of a water-saturated $5\% \text{H}_2/95\% \text{Ar}$ and dry N_2 gas mixture ($p\text{O}_2 \approx 10^{-12} \text{atm}$) for $\text{Ln} = \text{Y}$ and Gd , in a flow of water-saturated $5\% \text{H}_2/95\% \text{Ar}$ gas for $\text{Ln} = \text{Eu}$, Sm , and Nd , and in an $\sim 1\%$ of dry H_2 atmosphere for $\text{Ln} = \text{Pr}$. The compounds with larger Ln cations were prepared under stronger reducing conditions. Powders of fully-reduced $\text{LnBaMn}_2\text{O}_{5+\delta}$ ($\delta \approx 0$) were used for study oxygen uptake/release behavior in the thermogravimetry (TG) experiments which will be discussed in the next section. In comparison with the thermogravimetry data, the fully-reduced $\text{LnBaMn}_2\text{O}_{5+\delta}$ ($\text{Ln} = \text{Y}$, Gd , Eu , Sm , Nd , and Pr) samples were annealed at 800°C in a tube furnace under an O_2 atmosphere to obtain fully-oxidized (O_6) phases [39, 52]. Subsequently, the half-reduced $\text{LnBaMn}_2\text{O}_{5.5}$ phase was obtained by annealing O_6 phase under a N_2 atmosphere ($p\text{O}_2 \approx 10^{-4} \text{atm}$) [39]. The nitrogen-annealing conditions of

$\text{LnBaMn}_2\text{O}_6$ compounds were experimentally varied, and are summarized in Table 2.2. However, $\text{PrBaMn}_2\text{O}_{5.5}$ was not obtained by annealing in N_2 (see Chapter 3 for further discussion) but could be prepared by heating a stoichiometric mixture of $\text{PrBaMn}_2\text{O}_5$ and $\text{PrBaMn}_2\text{O}_6$ at $800\text{ }^\circ\text{C}$ in evacuated sealed quartz tube. The iodometric titration were done on the selected samples, and the oxygen content ($5+\delta$) values were close to 5.00, 5.50 and 6.00 for respectively O_5 , $\text{O}_{5.5}$ and O_6 phases for $\text{LnBaMn}_2\text{O}_{5+\delta}$ ($\text{Ln} = \text{Y, Gd, and Pr}$) samples (Table 2.3).

Room temperature X-ray diffraction data indicated that the three phases (O_5 , $\text{O}_{5.5}$, and O_6) of all $\text{LnBaMn}_2\text{O}_{5+\delta}$ samples were single phase, except that very weak diffraction peaks attributed to the traces of Y_2O_3 , Eu_2O_3 , and Nd_2O_3 purities were observed on the data of samples with $\text{Ln} = \text{Y, Eu, and Nd}$, respectively. Structural data for $\text{LnBaMn}_2\text{O}_{5+\delta}$ samples obtained by Le Bail refinement are summarized in Table 2.3. All fully-reduced $\text{LnBaMn}_2\text{O}_5$ ($\text{Ln} = \text{Y, Gd, Eu, Sm, Nd, and Pr}$) compounds were refined using tetragonal P4/nmm symmetry, consistent with reports [39, 41, 44-45, 57-58]. For the fully-oxidized (O_6) sample with the small Y^{3+} cation, the literature data reported either monoclinic P2 or triclinic $\text{P}\bar{1}$ space groups [39, 63-64]. The reported structural data of YBaMn_2O_6 in this work were refined in the triclinic symmetry. The structures of $\text{LnBaMn}_2\text{O}_6$ with bigger (Gd^{3+} , Eu^{3+} , and Sm^{3+}) cations were indexed in the tetragonal P4/nmm space group, as reported in the literatures [45, 53, 65]. In the case of larger Nd^{3+} cation, the structure of $\text{NdBaMn}_2\text{O}_6$ was reported in tetragonal P4/mmm space group [58, 65], however, other studies reported a lowering symmetry in either orthorhombic Pmmm [57] or triclinic $\text{P}\bar{1}$ [45] due to an indication of a split of (220) diffraction peak at $2\theta \sim 46.5^\circ$. The refinement of the $\text{NdBaMn}_2\text{O}_6$ data in the present study was obtained using Pmmm space group,

giving lattice parameters in good agreement with those in the literature [57]. The structure of $\text{PrBaMn}_2\text{O}_6$ was indexed based on a tetragonal $P4/mmm$ space group, consistent with previous reports [44, 65]. The diffraction pattern of half-reduced $\text{YBaMn}_2\text{O}_{5.5}$ was refined based on an orthorhombic $Icma$ structure, as previously reported in the literature [40]. For the half-reduced compounds with larger cations, the orthorhombic $Ammm$ space group was reported for the neutron diffraction of $\text{LaBaMn}_2\text{O}_{5.5}$ [54], and adopted for the recent neutron diffraction data at high temperature for $\text{LnBaMn}_2\text{O}_{5.5}$ with $\text{Ln} = \text{Nd}$ and Pr [56]. While Tonas *et al.* [57] reported the high-temperature neutron patterns of $\text{NdBaMn}_2\text{O}_{5.5}$ fitted with the orthorhombic $Icma$ model. The structural data are no available in the literature for $\text{LnBaMn}_2\text{O}_{5.5}$ with Gd^{3+} , Eu^{3+} , and Sm^{3+} cations. The diffraction patterns of all $\text{LnBaMn}_2\text{O}_{5.5}$ samples in this work were well fitted with the orthorhombic $Icma$ space group. The refined data for $\text{GdBaMn}_2\text{O}_{5+\delta}$ are shown in Fig. 2.2 as representative examples (see Appendix for the refined data of all other samples).

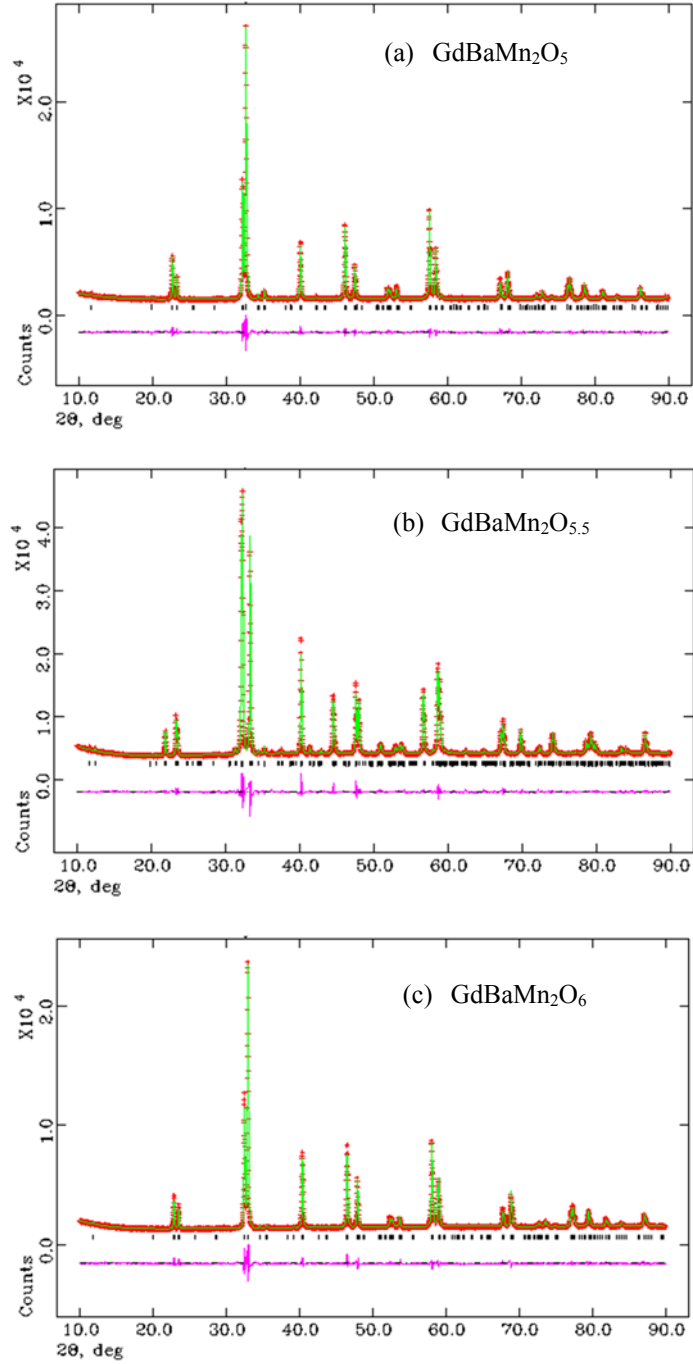


Fig. 2.2 X-ray data for (a) GdBaMn₂O₅, (b) GdBaMn₂O_{5.5}, and (c) GdBaMn₂O₆. The measured data are shown in red, the calculated data are shown in green, and the difference is shown in pink. Bragg reflections are shown by vertical tick marks.

Table 2.3 LnBaMn₂O_{5+δ} (Ln = Y, Gd, Eu, Sm, Nd, and Pr) summary: ionic radius of Ln³⁺ (CN = 8), excess oxygen content (δ) determined by iodometric titration, and structural parameters.

Composition	Ionic Ln ³⁺ Radius (CN = 8)/Å	Excess oxygen Content δ	Space group	a (Å)	b (Å)	c (Å)	Volume (Å ³)	χ ²	wRp (%)
YBaMn ₂ O ₅	1.019	-0.002(1)	P4/nmm	5.5494(1)		7.6522(1)	235.66(1)	2.12	6.14
YBaMn ₂ O _{5.5}		0.482(6)	Icma	8.1590(1)	7.5452(1)	15.2731(2)	940.29(2)	3.65	6.66
YBaMn ₂ O ₆		0.943(2)	P $\bar{1}$	5.5248(1)	5.5192(1)	7.6087(1)	232.01(1)	1.57	3.72
				$\alpha = 89.982(2)$ $\beta = 90.299(0)$ $\gamma = 90.017(2)$					
GdBaMn ₂ O ₅	1.053	0.023(6)	P4/nmm	5.5790(1)		7.6825(1)	239.12(1)	2.09	5.40
GdBaMn ₂ O _{5.5}		0.437(6)	Icma	8.1504(2)	7.5909(1)	15.3049(2)	946.89(3)	4.20	5.49
GdBaMn ₂ O ₆		0.972(9)	P4/nmm	5.5349(1)		7.6074(1)	233.05(1)	2.33	6.08
EuBaMn ₂ O ₅	1.066		P4/nmm	5.5843(0)		7.6887(1)	239.77(0)	1.79	9.33
EuBaMn ₂ O _{5.5}			Icma	8.1492(1)	7.6047(1)	15.3051(2)	948.50(1)	1.70	6.79
EuBaMn ₂ O ₆			P4/nmm	5.5400(1)		7.6130(1)	233.66(1)	1.30	5.81
SmBaMn ₂ O ₅	1.079		P4/nmm	5.5950(1)		7.7059(1)	241.22(0)	2.30	7.50
SmBaMn ₂ O _{5.5}			Icma	8.1443(1)	7.6167(1)	15.3066(3)	949.51(1)	1.89	8.62
SmBaMn ₂ O ₆			P4/nmm	5.5433(0)		7.6202(1)	234.15(0)	1.50	6.51
NdBaMn ₂ O ₅	1.109		P4/nmm	5.6134(0)		7.7338(1)	243.70(0)	2.40	9.59
NdBaMn ₂ O ₆			Pmmm	3.9042(1)	3.8925(1)	7.7285(1)	117.45(0)	1.52	5.26
PrBaMn ₂ O ₅	1.126	-0.006(2)	P4/nmm	5.6259(1)		7.7550(2)	245.45(1)	2.39	7.76
PrBaMn ₂ O _{5.5}		0.435(6)	Icma	8.1635(2)	7.6863(2)	15.3295(4)	961.89(3)	3.92	6.51
PrBaMn ₂ O ₆		0.930(4)	P4/mmm	3.8996(1)		7.7506(1)	117.86(0)	1.81	5.58

Figure 2.3 shows a plot of unit cell volumes for $\text{LnBaMn}_2\text{O}_{5+\delta}$ as a function of Ln^{3+} ionic radius. As expected, the unit cell volumes for O_5 , $\text{O}_{5.5}$, and O_6 phases linearly increase (but with different slopes) with increasing Ln^{3+} radius in the order of Y, Gd, Eu, Sm, Nd, and Pr. In $\text{LnBaMn}_2\text{O}_6$, the Ln^{3+} ion is smaller than the cubo-octahedral void (12-fold coordination), and consequently only a small change in the cell volume is observed as the Ln^{3+} radius increases [42, 45]. Note that results are presented taking the Ln ionic radius for 8-coordination as in the reduced O_5 compounds because the data for 12-fold coordination are not directly available [66]. The unit cell volume decreases when going from O_5 to O_6 phase as a consequence of a change in the average Mn oxidation state from 2.5+ to 3.5+, but the unit cell increases substantially when going from O_6 to the $\text{O}_{5.5}$ phase where all the Mn ions are 3+. The relative changes in the unit cell volume between O_6 , O_5 , and $\text{O}_{5.5}$ phases increase as the ionic radius of Ln^{3+} increases.

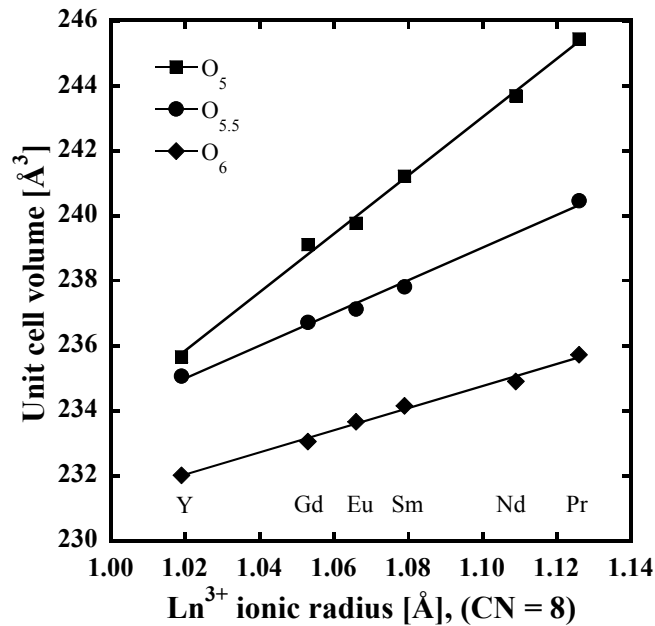


Fig. 2.3 Unit cell volumes of the $\text{LnBaMn}_2\text{O}_{5+\delta}$ phases (normalized to $Z = 2$) as a function of Ln^{3+} ionic radius.

2.3.2 Oxygen-Storage Properties

The oxygen uptake/release behavior of $\text{LnBaMn}_2\text{O}_{5+\delta}$ ($\text{Ln} = \text{Y, Gd, Eu, Sm, Nd, Pr}$) compounds determined by thermogravimetry are presented in Fig. 2.4, and a summary of oxygen uptake/release data is given in Table 2.4. For oxygen uptake, as-synthesized samples of $\text{LnBaMn}_2\text{O}_5$ were heated and then cooled in O_2 or air between room temperature and $800\text{ }^\circ\text{C}$ at a rate of $2\text{ }^\circ\text{C}/\text{min}$. As shown in Fig. 2.4 (a-b), all samples exhibit a large weight gain in a single sharp step both in air and oxygen attributed to the increase in oxygen content. The magnitude of the weight gains for all samples is in a good agreement with the value expected for the O_5 -to- O_6 inter-conversion. The oxygen uptake/release reaction can be expressed as $\text{YBaMn}_2\text{O}_5 (\text{s}) + 1/2\text{O}_2 (\text{g}) \leftrightarrow \text{YBaMn}_2\text{O}_6 (\text{s})$. The small differences of the weight gains in oxygen and air most probably due to differences in surface H_2O or CO_3^{2-} ; it is noticeable in the data for $\text{YBaMn}_2\text{O}_{5+\delta}$ in O_2 that a small weight loss occurs below $300\text{ }^\circ\text{C}$ indicative of some surface adsorption. If this is taken into account then the weight gains in air and oxygen are the same. Apparently, the $\text{YBaMn}_2\text{O}_{5+\delta}$ sample has the highest weight gain due to its lowest molar mass. For oxidation in oxygen, the weight of Y-containing sample increases at $\sim 250\text{ }^\circ\text{C}$, and then saturates above $\sim 400\text{ }^\circ\text{C}$, whereas the samples with larger Pr, Nd, Sm, Eu, and Gd cations show that the oxygen uptake starts at lower temperatures, namely $\sim 160, 180, 200, 210,$ and $220\text{ }^\circ\text{C}$, respectively (Fig. 2.4 (a)), indicating a systematic relationship between the Ln^{3+} ionic radius and the onset temperatures. This behavior may be explained on the basis of the coordination tendency of Ln^{3+} . The oxidation of $\text{LnBaMn}_2\text{O}_5$ to $\text{LnBaMn}_2\text{O}_6$ increases the coordination number at Ln site from 8 to 12,

which is favored by a larger Ln cation. The energetics associated with the oxidation of $\text{LnBaMn}_2\text{O}_{5+\delta}$ will be discussed further in Chapter 3.

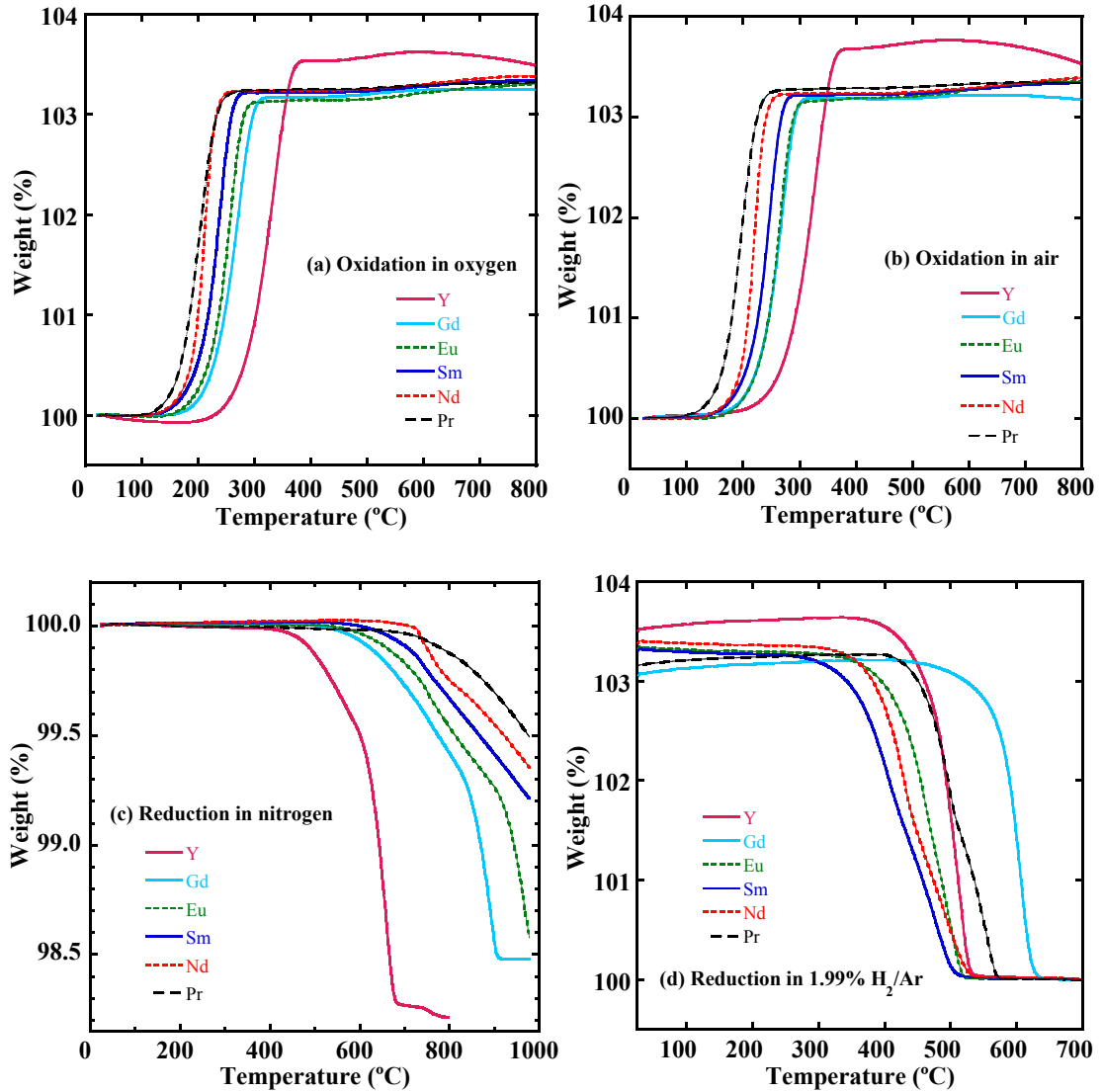


Fig. 2.4 Thermogravimetric analysis of $\text{LnBaMn}_2\text{O}_{5+\delta}$ ($\text{Ln} = \text{Y, Gd, Eu, Sm, Nd}$ and Pr) compounds under: (a) oxygen, (b) air, (c) nitrogen, and (d) 1.99% H_2/Ar .

For oxygen release, the $\text{LnBaMn}_2\text{O}_6$ samples obtained by oxidation were subsequently heated up to 980 °C under N_2 at a 2 °C/min heating rate, followed by fast cooling (20 °C/min) to room temperature. The weight loss of samples with $\text{Ln} = \text{Y}$ and Gd occurs in the temperature range of ~400-800 °C and ~520-920 °C, respectively, and corresponds to a change of oxygen content close to 5.5 (Fig. 2.4 (c)). In the case of samples with $\text{Ln} = \text{Eu}, \text{Sm}, \text{Nd},$ and Pr , the reduction under N_2 ($p\text{O}_2 \approx 10^{-4}$ atm) to $\text{O}_{5.5}$ phase was not complete at 980 °C. Thermogravimetric analysis of the reduction of $\text{LnBaMn}_2\text{O}_6$ in 1.99% H_2/Ar , however, show that all of the $\text{LnBaMn}_2\text{O}_6$ compounds were fully reduced to $\text{LnBaMn}_2\text{O}_5$ below 700 °C with a weight loss corresponding to a release of ~1 oxygen atom per formula unit (see Fig. 2.4 (d) and Table 2.4). For samples with larger Ln cations (Sm^{3+} , Nd^{3+} , and Pr^{3+}), an inflection on the reduction curves in H_2 was observed, indicating the formation of half-reduced $\text{LnBaMn}_2\text{O}_{5.5}$. The reduction temperature of these materials under 1.99% H_2/Ar does not show the dependence on the Ln^{3+} ionic radius, similar to previous report [45]. As the oxygen uptake/release processes involve redox reactions at the powder surface; reduction of O_2 to form O^{2-} for oxygen uptake, and reaction between H_2 and O^{2-} to form H_2O for oxygen release [67], the oxygen uptake/release kinetics should depend on the grain size. Therefore, apart from chemical composition, the differences in grain size of samples, and in water content of each studied system should have an influence on the reaction kinetics and the onset temperature for oxygen release in H_2 .

Table 2.4 Oxygen-storage properties of $\text{LnBaMn}_2\text{O}_{5+\delta}$ (Ln = Y, Gd, Eu, Sm, Nd, and Pr) compounds. (Reduction in 1.99% H_2/Ar (N_2) obtained after oxidation in air (oxygen) for Ln = Y, Gd, and Pr, and after oxidation in oxygen (air) for Ln = Eu, Sm, and Nd)

Ln	Theoretical weight change between O_5 and O_6 (wt. %)	Oxidation of $\text{LnBaMn}_2\text{O}_5$: $\text{LnBaMn}_2\text{O}_5 + \delta\text{O} \rightarrow \text{LnBaMn}_2\text{O}_{5+\delta}$				Reduction of $\text{LnBaMn}_2\text{O}_{5+\delta}$: $\text{LnBaMn}_2\text{O}_{5+\delta} - x\text{O} \rightarrow \text{LnBaMn}_2\text{O}_{(5+\delta)-x}$			
		O_2		Air		1.99% H_2/Ar		N_2	
		Weight change (wt.%)	Change of δ (mol mol^{-1})	Weight change (wt.%)	Change of δ (mol mol^{-1})	Weight change (wt.%)	Change of x (mol mol^{-1})	Weight change (wt.%)	Change of x (mol mol^{-1})
Y	3.85	3.59	0.93	3.67	0.95	3.63	0.94	1.79	0.47
Gd	3.30	3.23	0.98	3.18	0.96	3.20	0.97	1.52	0.46
Eu	3.34	3.33	1.00	3.34	1.00	3.33	1.00	1.43	0.43
Sm	3.35	3.34	1.00	3.34	1.00	3.32	0.99	0.79	0.24
Nd	3.39	3.39	1.00	3.39	1.00	3.39	1.00	0.65	0.19
Pr	3.42	3.32	0.97	3.33	0.97	3.27	0.96	0.51	0.15

2.4 Conclusions

The A-site ordered double-perovskite $\text{LnBaMn}_2\text{O}_{5+\delta}$ oxides ($\text{Ln} = \text{Y, Gd, Eu, Sm, Nd, and Pr}$) with $\delta = 0$ were synthesized by solid-state reaction under reducing atmospheres. The fully-reduced $\text{LnBaMn}_2\text{O}_6$ ($\text{Ln} = \text{Y, Gd, Eu, Sm, Nd, and Pr}$) compounds were made by oxidation of $\text{LnBaMn}_2\text{O}_5$ in an oxygen atmosphere. The half-reduced $\text{LnBaMn}_2\text{O}_{5.5}$ phase was successfully prepared for $\text{Ln} = \text{Y, Gd, Eu, Sm, and Pr}$. The unit cell volume for the three phases (O_5 , $\text{O}_{5.5}$, and O_6) of $\text{LnBaMn}_2\text{O}_{5+\delta}$ was found to be linearly dependent on the ionic radius of Ln^{3+} . Only three distinct phases of $\text{LnBaMn}_2\text{O}_{5+\delta}$ with $\delta \approx 0, 0.5, \text{ and } 1$ were observed during the oxidation/reduction process. Thermogravimetric measurements show good oxygen uptake/release ability at moderate temperatures with oxygen-storage capacity (OSC) exceeding 3 wt. % for all $\text{LnBaMn}_2\text{O}_{5+\delta}$ compounds. The oxygen uptake/release behavior of the $\text{LnBaMn}_2\text{O}_{5+\delta}$ compounds are strongly influenced by A-site cationic substitution. $\text{LnBaMn}_2\text{O}_5$ with a larger Ln^{3+} ion starts to take up oxygen at a lower temperature in both air and oxygen atmospheres. These oxides exhibit almost complete and reversible oxygen uptake/release between fully-reduced $\text{LnBaMn}_2\text{O}_5$ and fully-oxidized $\text{LnBaMn}_2\text{O}_6$ during changes of the oxygen partial pressure between oxygen (or air) and 1.99% H_2/Ar .

2.5 References

1. He, H.; Dai, H. X.; Au, C. T. *Catal. Today* **2004**, *90*, 245-254.
2. Tsinoglou, D. N.; Koltsakis, G. C. *Ind. Eng. Chem. Res.* **2002**, *41* (5), 1152-1165.
3. Motohashi, T.; Hirano, Y.; Masubuchi, Y.; Oshima, K.; Setoyama, T.; Kikkawa, S. *Chem. Mater.* **2013**, *25*, 372-377.
4. Yang, Z.; Lin, Y. S.; Zeng, Y. *Ind. Eng. Chem. Res.* **2002**, *41*, 2775-2784.

5. Chen, X.; Jung, T.; Park, J.; Kim, W.-S. *J. Mater. Chem. A* **2015**, *3*, 258-265.
6. Shin, T. H.; Myung, J.-H.; Verbraeken, M.; Kim, G.; Irvine, J. T. S. *Faraday Discuss.* **2015**, *182*, 227-239.
7. Sengodan, S.; Choi, S.; Jun, A.; Shin, T. H.; Ju, Y.-W.; Jeong, H. Y.; Shin, J.; Irvine, J. T. S.; Kim, G. *Nat. Mater.* **2015**, *14* (2), 205-209.
8. Brett, D. J. L.; Atkinson, A.; Brandon, N. P.; Skinner, S. J. *Chem. Soc. Rev.* **2008**, *37*, 1568-1578.
9. Shafiefarhood, A.; Hamill, J. C.; Neal, L. M.; Li, F. *Phys. Chem. Chem. Phys.* **2015**, *17*, 31297-31307.
10. Neal, L.; Shafiefarhood, A.; Li, F. *Appl. Energy* **2015**, *157*, 391-398.
11. Neal, L. M.; Shafiefarhood, A.; Li, F. *ACS Catal.* **2014**, *4* (10), 3560-3569.
12. Bhavsar, S.; Vesper, G. *RSC Adv.* **2014**, *4*, 47254-47267.
13. Wang, K.; Yu, Q.; Qin, Q. *Therm. Anal. Calorim.* **2013**, *112*, 747-753.
14. Li, K.; Wang, H.; Wei, Y. *J. Chem.* **2013**, 1-8.
15. Adanez, J.; Abad, A.; Garcia-Labiano, F.; Gayan, P.; de Diego, L. F. *Prog. Energy Combust. Sci.* **2012**, *38* (2), 215-282.
16. Wei, Y.; Wang, H.; He, F.; Ao, X.; Zhang, C. *J. Nat. Gas Chem.* **2007**, *16* (1), 6-11.
17. Ryde'n, M.; Lyngfelt, A.; Mattisson, T. *Fuel* **2006**, *85*, 1631-1641.
18. Adanez, J.; de Diego, L. F.; Garcia-Labiano, F.; Gayan, P.; Abad, A. *Energy Fuels* **2004**, *18*, 371-377.
19. Taylor, D. D.; Schreiber, N. J.; Levitas, B. D.; Xu, W.; Whitfield, P. S.; Rodriguez, E. E. *Chem. Mater.* **2016**, *28*, 3951-3960.
20. Dabrowski, B.; Remsen, S.; Mais, J.; Kolesnik, S. *Funct. Mater. Lett.* **2011**, *4* (2), 147-150.
21. Klimkowicz, A.; Świerczek, K.; Takasaki, A.; Dabrowski, B. *Solid State Ionics* **2014**, *257*, 23-28.
22. Lai, K.-Y.; Manthiram, A. *Chem. Mater.* **2016**, *28*, 9077-9087.
23. Sugiura, M. *Catal. Surv. Asia* **2003**, *7* (1), 77-87.

24. Kašpar, J.; Fornasiero, P.; Hickey, N. *Catal. Today* **2003**, *77*, 419-449.
25. Parkkima, O.; Yamauchi, H.; Karppinen, M. *Chem. Mater.* **2013**, *25* (4), 599-604.
26. Nagaia, Y.; Yamamoto, T.; Tanaka, T.; Satohiro Yoshida, B.; Nonaka, T.; Okamoto, T.; Suda, A.; Sugiura, M. *Catal. Today* **2002**, *74*, 225-234.
27. Damyanova, S.; Pawelec, B.; Arishtirova, K.; Huerta, M. V. M.; Fierro, J. L. G. *Appl. Catal. A Gen.* **2008**, *337*, 86-96.
28. Di Monte, R.; Fornasiero, P.; Graziani, M.; Kašpar, J. *J. Alloys Compd.* **1998**, *275-277*, 877-885.
29. Kašpar, J.; Fornasiero, P. *J. Solid State Chem.* **2003**, *171*, 19-29.
30. Otsuka, K.; Wang, Y.; Nakamura, M. *Appl. Catal. A Gen.* **1999**, *183*, 317-324.
31. Pantu, P.; Kimb, K.; Gavalas, G. R. *Appl. Catal. A Gen.* **2000**, *193*, 203-214.
32. Hao, Y.; Yang, C.-K.; Haile, S. M. *Chem. Mater.* **2014**, *26*, 6073-6082.
33. Karppinen, M.; Yamauchi, H.; Otani, S.; Fujita, T.; Motohashi, T.; Huang, Y.-H.; Valkeapää, M.; Fjellvåg, H. *Chem. Mater.* **2006**, *18* (2), 490-494.
34. Remsen, S.; Dabrowski, B. *Chem. Mater.* **2011**, *23*, 3818-3827.
35. Hervieu, M.; Guesdon, A.; Bourgeois, J.; Elkaïm, E.; Poienar, M.; Damay, F.; Rouquette, J.; Maignan, A.; Martin, C. *Nat. Mater.* **2014**, *13*, 74-80.
36. Motohashi, T.; Ueda, T.; Masubuchi, Y.; Takiguchi, M.; Setoyama, T.; Oshima, K.; Kikkawa, S. *Chem. Mater.* **2010**, *22* (10), 3192-3196.
37. King, G.; Woodward, P. M. *J. Mater. Chem.* **2010**, *20*, 5785-5796.
38. Chapman, J. P.; Attfield, J. P.; Molgg, M.; Friend, C. M.; Beales, T. P. *Angew. Chem. Int. Ed. Engl.* **1996**, *35* (21), 2482-2484.
39. Karppinen, M.; Okamoto, H.; Fjellvåg, H.; Motohashi, T.; Yamauchi, H. *J. Solid State Chem.* **2004**, *177*, 2122-2128.
40. Perca, C.; Pinsard-Gaudart, L.; Daoud-Aladine, A.; Fernández-Díaz, M. T.; Rodríguez-Carvajal, J. *Chem. Mater.* **2005**, *17* (7), 1835-1843.
41. Klimkowicz, A.; Zheng, K.; Fiolka, G.; Świerczek, K. *Chemik* **2013**, *67* (12), 1199-1206.
42. Świerczek, K.; Klimkowicz, A.; Zheng, K.; Dabrowski, B. *J. Solid State Chem.* **2013**, *203*, 68-73.

43. Świerczek, K.; Klimkowicz, A.; Niemczyk, A.; Olszewska, A.; Rząsa, T.; Molenda, J.; Takasaki, A. *Funct. Mater. Lett.* **2014**, 7 (6), 1440004.
44. Klimkowicz, A.; Świerczek, K.; Zheng, K.; Baranowska, M.; Takasaki, A.; Dabrowski, B. *Solid State Ionics* **2014**, 262, 659-663.
45. Klimkowicz, A.; Świerczek, K.; Takasaki, A.; Molenda, J.; Dabrowski, B. *Mater. Res. Bull.* **2015**, 65, 116-122.
46. Motohashi, T.; Kimura, M.; Inayoshi, T.; Ueda, T.; Masubuchi, Y.; Kikkawa, S. *Dalton Trans.* **2015**, 44, 10746-10752.
47. Klimkowicz, A.; Świerczek, K.; Rząsa, T.; Takasaki, A.; Dabrowski, B. *Solid State Ionics* **2016**, 288, 43-47.
48. Klimkowicz, A.; Świerczek, K.; Yamazaki, T.; Takasaki, A. *Solid State Ionics* **2016**, 298, 66-72.
49. Motohashi, T.; Kimura, M.; Masubuchi, Y.; Kikkawa, S.; George, J.; Dronskowski, R. *Chem. Mater.* **2016**, 28 (12), 4409-4414.
50. Beales, T. P.; Molgg, M.; Jutson, J.; Friend, C. M. *Phys. Stat. Sol. A* **1997**, 161 (1), 271-282.
51. McAllister, J. A.; Attfield, J. P. *J. Mater. Chem.* **1998**, 8 (5), 1291-1294.
52. Millange, F.; Caignaert, V.; Domenge's, B.; Raveau, B. *Chem. Mater.* **1998**, 10 (7), 1974-1983.
53. Nakajima, T.; Kageyama, H.; Yoshizawa, H.; Ueda, Y. *J. Phys. Soc. Jpn.* **2002**, 71 (12), 2843-2846.
54. Caignaert, V.; Millange, F.; Domengès, B.; Raveau, B.; Suard, E. *Chem. Mater.* **1999**, 11 (4), 930-938.
55. Castillo-Martínez, E.; Williams, A. J.; Attfield, J. P. *J. Solid State Chem.* **2006**, 179 (11), 3505-3510.
56. Klimkowicz, A.; Świerczek, K.; Zheng, K.; Wallacher, D.; Takasaki, A. *J. Mater. Sci.* **2017**, 52 (11), 6476-6485.
57. Tonus, F.; Bahout, M.; Dorcet, V.; Gauthier, G. H.; Paofai, S.; Smith, R. I.; Skinner, S. J. *J. Mater. Chem. A* **2016**, 4 (30), 11635-11647.
58. Pineda, O. L.; Moreno, Z. L.; Roussel, P.; Świerczek, K.; Gauthier, G. H. *Solid State Ionics* **2016**, 288, 61-67.

59. Jeamjumnunja, K.; Gong, W.; Makarenko, T.; Jacobson, A. J. *J. Solid State Chem.* **2015**, *230*, 397-403.
60. Jeamjumnunja, K.; Gong, W.; Makarenko, T.; Jacobson, A. J. *J. Solid State Chem.* **2016**, *239*, 36-45.
61. Karppinen, M.; Fukuoka, A.; Niinisto, L.; Yamauchi, H. *Supercond. Sci. Technol.* **1996**, *9*, 121-135.
62. Georgieva, S.; Nedeltcheva, T.; Stoyanova-Ivanova, A. *Am. Chem. Sci. J.* **2016**, *13* (1), 1-15.
63. Nakajima, T.; Kageyama, H.; Ueda, Y. *J. Phys. Chem. Solids* **2002**, *63*, 913-916.
64. Williams, A. J.; Attfield, J. P. *Phys. Rev. B* **2005**, *72* (2), 024436.
65. Ueda, Y.; Nakajima, T. *J. Phys.: Condens. Matter* **2004**, *16*, S573-S583.
66. Shannon, R. D. *Acta Cryst.* **1976**, *A 32*, 751-767.
67. Motohashi, T.; Ueda, T.; Masubuchi, Y.; Kikkawa, S. *J. Ceram. Soc. Jpn.* **2011**, *119* (11), 894-897.

Appendix

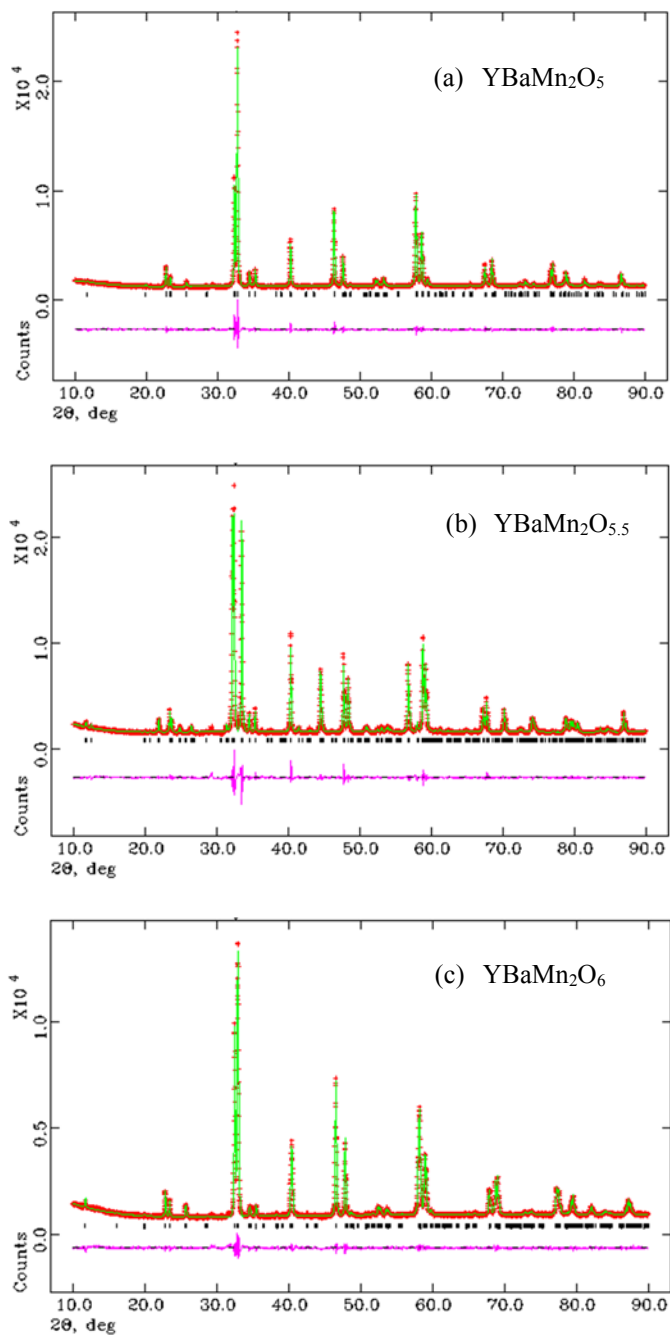


Fig. A-2.1 X-ray data for (a) YBaMn_2O_5 , (b) $\text{YBaMn}_2\text{O}_{5.5}$, and (c) YBaMn_2O_6 . The measured data are shown in red, the calculated data are shown in green, and the difference is shown in pink. Bragg reflections are shown by vertical tick marks.

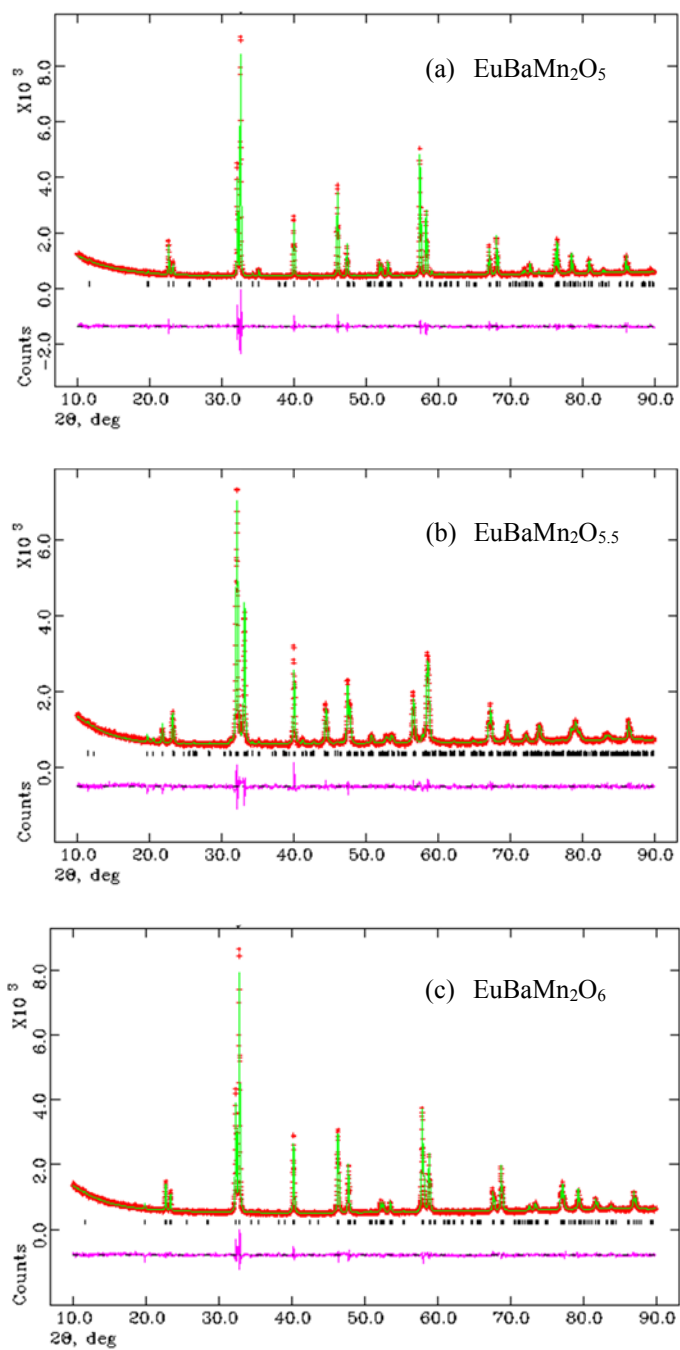


Fig. A-2.2 X-ray data for (a) $\text{EuBaMn}_2\text{O}_5$, (b) $\text{EuBaMn}_2\text{O}_{5.5}$, and (c) $\text{EuBaMn}_2\text{O}_6$. The measured data are shown in red, the calculated data are shown in green, and the difference is shown in pink. Bragg reflections are shown by vertical tick marks.

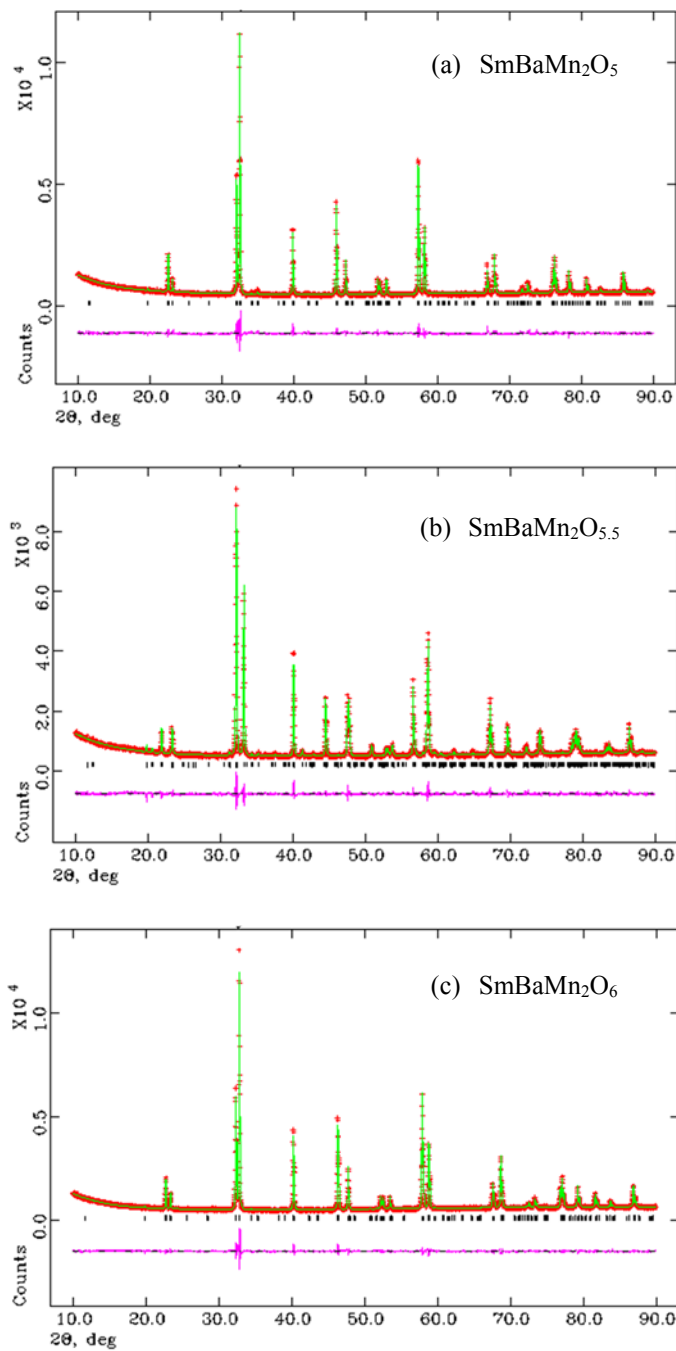


Fig. A-2.3 X-ray data for (a) $\text{SmBaMn}_2\text{O}_5$, (b) $\text{SmBaMn}_2\text{O}_{5.5}$, and (c) $\text{SmBaMn}_2\text{O}_6$. The measured data are shown in red, the calculated data are shown in green, and the difference is shown in pink. Bragg reflections are shown by vertical tick marks.

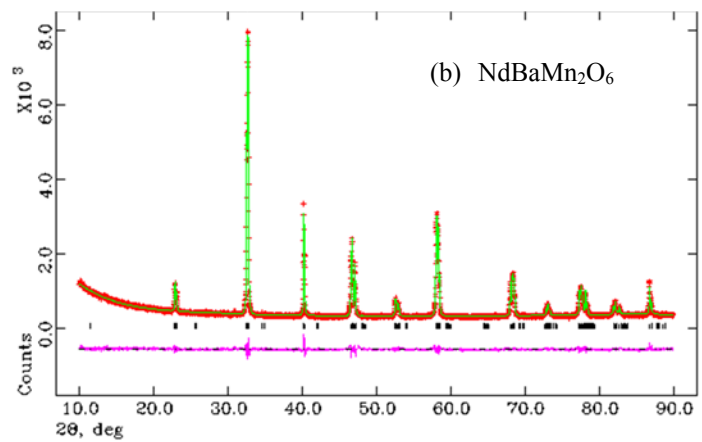
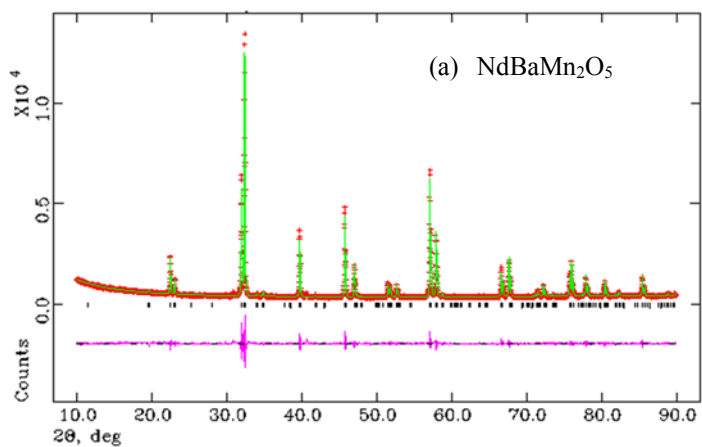


Fig. A-2.4 X-ray data for (a) $\text{NdBaMn}_2\text{O}_5$ and (b) $\text{NdBaMn}_2\text{O}_6$. The measured data are shown in red, the calculated data are shown in green, and the difference is shown in pink. Bragg reflections are shown by vertical tick marks.

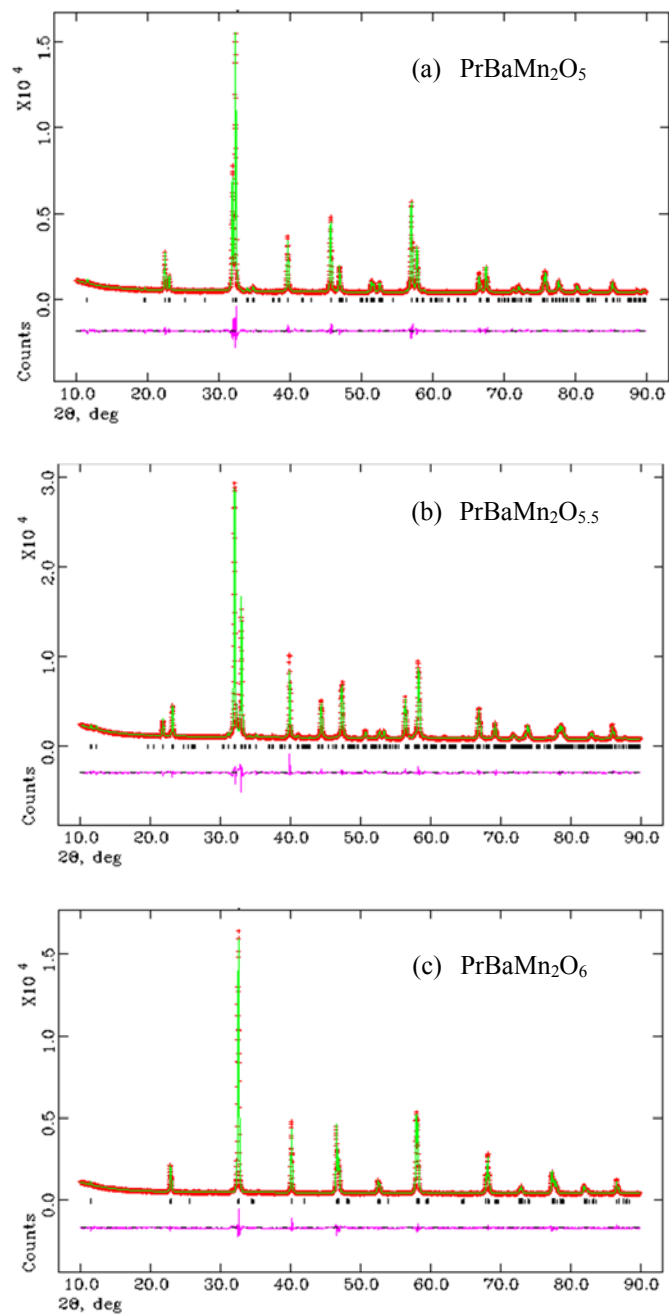


Fig. A-2.5 X-ray data for (a) $\text{PrBaMn}_2\text{O}_5$, (b) $\text{PrBaMn}_2\text{O}_{5.5}$, and (c) $\text{PrBaMn}_2\text{O}_6$. The measured data are shown in red, the calculated data are shown in green, and the difference is shown in pink. Bragg reflections are shown by vertical tick marks.

CHAPTER 3

Oxygen Non-stoichiometry of the Oxygen-Storage Materials

$\text{LnBaMn}_2\text{O}_{5+\delta}$ (Ln = Y, Gd, and Pr)

3.1 Introduction

Non-stoichiometric oxides which are capable of rapidly and reversibly storing and releasing large amounts of oxygen are called oxygen-storage materials (OSMs). They have recently attracted interest for their wide applicability in oxygen-related technology [1-10]. As discussed in Chapter 2, the series of $\text{LnBaMn}_2\text{O}_{5+\delta}$ (Ln = Y, Gd, Eu, Sm, Nd, and Pr) show good oxygen intake/release characteristics. These oxides have the potential ability to precisely control redox reactions. The oxygen site in lanthanide-oxygen layers is filled/unfilled in response to the variations of temperature and the surrounding atmosphere, resulting in a large oxygen stoichiometry ranging from $0 \leq \delta \leq 1$. The $\text{LnBaMn}_2\text{O}_{5+\delta}$ oxides have three distinct phases on oxidation/reduction with $\delta \approx 0, 0.5$ and 1 (i.e. $\text{O}_5, \text{O}_{5.5}$, and O_6 forms, respectively).

In addition to the study of their oxygen-storage behavior and oxygen-storage capacity, understanding the oxygen non-stoichiometry and phase stability of $\text{LnBaMn}_2\text{O}_{5+\delta}$ under near-equilibrium conditions during redox reactions at different oxygen partial pressure ($p\text{O}_2$) and temperatures is needed to evaluate their use in practical oxygen-related applications. Motohashi *et al.* have recently reported the oxygen non-stoichiometry of $\text{LnBaMn}_2\text{O}_{5+\delta}$ (Ln = Y, Gd, Nd, and La) [11-12]. The $p\text{O}_2$ dependence of the inter-conversion of $\text{LnBaMn}_2\text{O}_{5.5}$ and $\text{LnBaMn}_2\text{O}_{-6}$ in the $p\text{O}_2$ range 10 Pa to 10^5 Pa (10^{-4} to 1 atm) and the range of composition of 'O₆' was determined by

thermogravimetric analysis. The oxygen uptake/release kinetics of $\text{YBaMn}_2\text{O}_{5+\delta}$, and the effects of Ln-substitution on the operating temperatures and the reaction kinetics were studied [13-20]. To our knowledge, no data have been reported for $\text{LnBaMn}_2\text{O}_{5+\delta}$ compound systems in term of thermodynamics and reversibility under near-equilibrium conditions.

In the present work, the oxygen non-stoichiometry (δ) of $\text{LnBaMn}_2\text{O}_{5+\delta}$ (Ln = Y, Gd, and Pr) was determined by solid-state Coulometric titration in sealed electrochemical cells under near-equilibrium conditions. Oxygen non-stoichiometry (δ) was measured over a wide range of oxygen partial pressures ($\sim 10^{-25} \leq p\text{O}_2 \text{ (atm)} \leq \sim 1$) at 600, 650, 700, and 750 °C, providing both thermodynamic and kinetic data. The effect of cationic substitution on oxygen non-stoichiometric behavior was investigated by using Y, Gd and Pr ions as representative systems with rare earth ions of different sizes. The data in this chapter were published by Jeamjumnunja *et al.* [21-22].

3.2 Experimental Section

3.2.1 Sample Preparation

The synthesis of the double-perovskite $\text{LnBaMn}_2\text{O}_{5+\delta}$ oxides must be performed at low oxygen partial pressure to avoid the formation of the stable oxides $\text{BaMnO}_{3-\delta}$ and LnMnO_3 [23-26]. As described in Chapter 2, samples of polycrystalline $\text{LnBaMn}_2\text{O}_5$ (Ln = Y, Gd, and Pr) were synthesized *via* a solid-state reaction under a mixture of N_2 and 5% $\text{H}_2/95\%$ Ar gas. BaCO_3 (Aldrich 99.999%), Mn_2O_3 (Aldrich 99%), and the appropriate lanthanide oxide (Y_2O_3 , Aldrich, 99.99%; Gd_2O_3 , Aldrich, 99.9%; Pr_6O_{11} , Aldrich 99.9%; for Ln: Y, Gd and Pr, respectively) were used as starting precursors. The

stoichiometric mixtures of precursors were ball-milled in isopropanol for 24 h and then oven dried at 80 °C for 48 h. The fully-reduced YBaMn₂O₅ and GdBaMn₂O₅ were obtained by sintering the ball-milled precursor powder in a tube furnace at 1050 °C for 22 h in flowing dry N₂ and a water-saturated 5% H₂/95% Ar gas mixture ($p_{\text{O}_2} \approx 10^{-12}$ atm), and then rapidly cooled to room temperature. In the synthesis of fully-reduced PrBaMn₂O₅, the sample was obtained by heating the precursor at 1000 °C for 17 h in an atmosphere containing ~ 1% H₂, obtained by mixing of dry N₂ gas (120 cm³ min⁻¹) and dry 5% H₂/95% Ar gas (30 cm³ min⁻¹), and then rapidly cooled to room temperature. The sample was reheated at the same conditions for two more times with intermediate grinding.

The as-synthesized LnBaMn₂O_{5+ δ} of each compound was a pure phase of the fully-reduced “O₅” form, which was checked using powder X-ray diffraction in the range $10 \leq 2\theta \leq 90$ with Cu K α radiation ($\lambda = 1.54046$ Å) on a Phillips PANalytical X’Pert PRO diffractometer at room temperature. As reported in Chapter 2, all reflections in the powder X-ray diffraction patterns of Y-, Gd-, and Pr-sample were indexed on the cell reported in references [19-20, 27], thus confirming the powder to be single-phase. The precise oxygen content (5+ δ) of all compounds determined by iodometric titration was close to 5.0.

3.2.2 Solid-State Coulometric Titration

3.2.2.1 Theoretical background

Oxygen non-stoichiometry is one of the most important properties of oxide materials. There are a variety of techniques used to determine the oxygen content in the

materials including thermogravimetry [28-36], iodometric titration [37-42], and Coulometric titration [43-64]. The unique feature of the Coulometric titration is that the measurement can be run at very low oxygen partial pressures. The data acquisition consists in measurement of currents and voltages, and the experiment is easily computerized. The measurement of electrical quantities makes Coulometric titration a high precision technique, more than other techniques such as thermogravimetry.

In this thesis, the oxygen non-stoichiometry of the oxide samples at elevated temperature was determined by solid-state Coulometric titration technique by measuring the oxygen partial pressure (p_{O_2}) as a function of temperature. The experiment was carried out with a gas-tight electrochemical cell consisting of an electrolyte (8-wt % polycrystalline yttria-stabilized zirconia, YSZ, disc), two alumina rings, three glass rings and sample alumina container as shown in Figure 3.1. The top of the cell was covered with the YSZ disc connected to Pt wires and Pt meshes. This YSZ disc was used for pumping oxygen in/out of the titration cell and as an oxygen sensor. The Pt wires connected to the YSZ disc were brought out of the cell via glass rings. The electrochemical cell was placed in a furnace and spring-loaded at the top of the apparatus to help the sealing process. An R-type thermocouple was installed just above the cell for monitoring temperature. Figure 3.2 illustrates the complete apparatus of Coulometric titration technique. The gas-tight seals were made by heating the cell above the softening temperature of the glass rings (~ 750 °C). The height of cell was ~ 15 mm after sealing. A Keithley 2400 SourceMeter was used to provide the current for the oxygen pump and to monitor the YSZ sensor voltage. The overall experiments were controlled by LabView software.

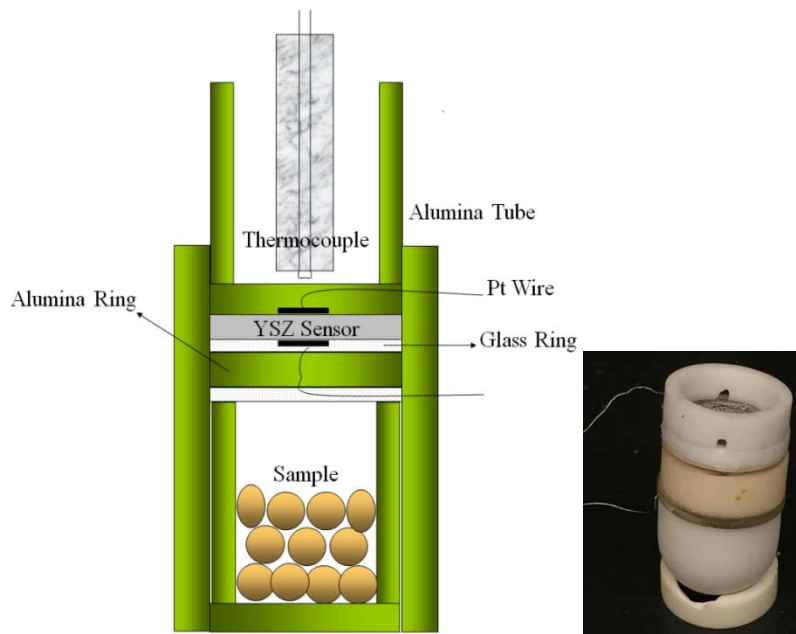


Fig. 3.1 An electrochemical cell for Coulometric titration.

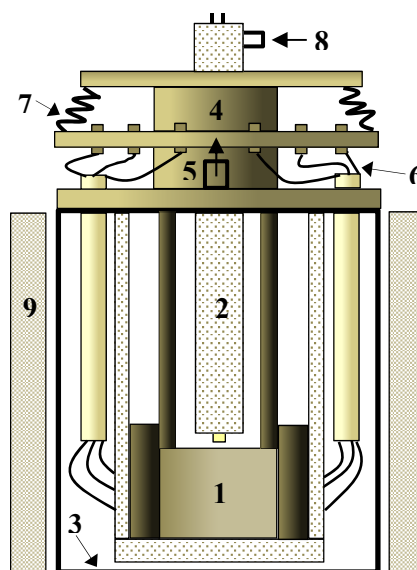


Fig. 3.2 The complete apparatus of Coulometric titration: (1) a titration cell, (2) thermocouple, (3) quartz tube, (4) metal frame, (5) gas out, (6) Pt wires, (7) spring, (8) gas in, (9) furnace.

The electrochemical cell using a solid oxide electrolyte can be used to quantitatively control the oxygen flux going into/out of the cell by applying a constant current for a given time [65-67]. Therefore, the oxygen stoichiometry of the sample inside the cell can be adjusted. The variation of number of moles of oxygen transferred by pumping is given by Faraday's law:

$$\Delta n_{O_2, total} = \frac{i \cdot t}{4F} \quad (3.1)$$

where, i is the applied current, t is the pumping time, F is the Faraday constant, and $\Delta n_{O_2, total}$ is the number of moles of oxygen transferred by pumping. When equilibrium is reached after pumping, the oxygen partial pressure (pO_2) inside the cell can be determined by reading the *EMF* developed across the cell with a known pO_2 reference on the outside of the cell. The oxygen partial pressure (pO_2) inside the cell is given by the Nernst equation:

$$pO_2^{cell} = pO_2^{ref} \cdot e^{\left(\frac{4FE}{RT}\right)} \quad (3.2)$$

where, pO_2^{cell} and pO_2^{ref} are the oxygen partial pressure inside the cell and of the reference gas, respectively, F is the Faraday constant, E is the cell *EMF*, and R is the gas constant. Air was used as the reference gas. At equilibrium, the oxygen molecules pumped into the cell are distributed between both the free space of the cell and the sample. Therefore, the change in the total number of moles of oxygen is the sum of the changes in number of moles in the sample and the free space:

$$\Delta n_{O_2, total} = \Delta n_{O_2, sample} + \Delta n_{O_2, space} \quad (3.3)$$

where, $\Delta n_{O_2, sample}$ and $\Delta n_{O_2, space}$ are the change of the number of moles of oxygen in the sample and in the free space of the cell, respectively. The value of $\Delta n_{O_2, space}$ was

calculated assuming ideal gas behavior. The cell volume is made as small as possible to minimize the correction.

The change of oxygen stoichiometry ($\Delta\delta$) of the sample is expressed by the following equation:

$$\Delta\delta = \frac{2M}{W} \cdot \Delta n_{O_2, sample} \quad (3.4)$$

where, M and W are the molecular weight and the weight of the sample. The change of oxygen stoichiometry ($\Delta\delta$) of the sample is then given by:

$$\Delta\delta = \frac{2M}{W} \cdot \Delta n_{O_2, sample} = \frac{2M}{W} \cdot (\Delta n_{O_2, total} - \Delta n_{O_2, space}) = \frac{2M}{W} \left\{ \left(\frac{it}{4F} \right) - \left(\frac{\Delta PV}{RT} \right) \right\} \quad (3.5)$$

In addition, a small correction is made for the oxygen leakage flux (J_O) through 8-mol % YSZ due to a small electronic contribution to the conductivity at low pO_2 . From previous results [68], the oxygen leakage flux (J_O) of 8-mole % YSZ is dependent on both pO_2 gradient and temperature according to:

$$J_O = \frac{RT}{FL} \cdot \left[\sigma_h(pO_2^{ref}) \cdot \left\{ \left(\frac{pO_2^{cell}}{pO_2^{ref}} \right)^{1/4} - 1 \right\} + \sigma_e(pO_2^{ref}) \cdot \left\{ 1 - \left(\frac{pO_2^{cell}}{pO_2^{ref}} \right)^{-1/4} \right\} \right] \quad (3.6)$$

where L is the thickness of the 8-mol % YSZ, $\sigma_h(pO_2)$ and $\sigma_e(pO_2)$ are pO_2 -dependent conductivities of the holes and electrons as followings:

$$\sigma_h(pO_2^{ref}) = (2.35 \times 10^2) \cdot e^{\left(\frac{-1.67 eV}{kT} \right)} \cdot pO_2^{1/4} \quad (3.7)$$

$$\sigma_e(pO_2^{ref}) = (1.31 \times 10^7) \cdot e^{\left(\frac{-3.88 eV}{kT} \right)} \cdot pO_2^{-1/4} \quad (3.8)$$

3.2.2.2 Experimental details of solid-state coulometric titration

The non-stoichiometry changes ($\Delta\delta$) of $LnBaMn_2O_{5+\delta}$ ($Ln = Y, Gd, \text{ and } Pr$) were determined in the pO_2 range of $\sim 10^{-25} \leq pO_2 \text{ (atm)} \leq \sim 1$ at four temperatures 600, 650,

700, and 750 °C. The fully-reduced O_5 sample of each compound was used as the starting material in the electrochemical cell setup. At the beginning of the experiment, the sample was allowed to equilibrate with the pO_2 inside the cell. A variation in the YSZ sensor voltage of less than $0.001\% \text{ min}^{-1}$ (for the Y-sample), $0.005\% \text{ min}^{-1}$ (for the Pr-sample at 650 °C, and the Gd-sample at all temperatures), and $0.01\% \text{ min}^{-1}$ (for the Pr-sample at the other temperatures) was chosen as the criteria for equilibrium. During the measurements, a known amount of oxygen was pumped into (or out of) the cell by continuously applying a current for a given time. The approach of the cell EMF to equilibrium at each cycle of pumping current was monitored, and the pO_2 inside the cell and $\Delta\delta$ were determined. All titration experiments at each temperature were performed on both decreasing and increasing pO_2 . At least three different cells for each sample were used to confirm the reproducibility.

3.3 Results and Discussion

3.3.1 Coulometric Titration of $YBaMn_2O_{5+\delta}$

3.3.1.1 Oxygen non-stoichiometry

The oxygen non-stoichiometry (δ) of $YBaMn_2O_{5+\delta}$ was measured as a function of oxygen partial pressure (pO_2) using Coulometric titration. Measurements were made in sealed electrochemical cells at $\sim 10^{-20} \leq pO_2 \text{ (atm)} \leq \sim 1$ on both decreasing and increasing pO_2 . At the beginning of the experiment, the electrochemical cell was heated up to 750 °C for 2 h in the sealing process, and then to the targeted temperature. During that time, the sample of $YBaMn_2O_{5+\delta}$ (with $\delta \approx 0$) was equilibrated and oxidized with air trapped inside the cell to the most oxidized phase ($\delta \approx 1$). The starting sensor voltage was

monitored. The change in the sensor voltage of $0.001\% \text{ min}^{-1}$ was chosen as a criterion for equilibrium for all temperatures. The measurement was started with reduction of a composition of $\text{O}_{5.6}$ to O_5 , and then the system was re-oxidized. Figure 3.3 (a-c) presents the dependence of the oxygen non-stoichiometry of $\text{YBaMn}_2\text{O}_{5+\delta}$ on $p\text{O}_2$ at 650, 700, and 750 °C, respectively. As expected, three distinct phases are apparent in the variation of the oxygen content with $p\text{O}_2$. At 650 °C, two phases have narrow ranges of composition with oxygen content $(5+\delta) = 4.99\text{-}5.02$ and $5.46\text{-}5.54$. The most oxidized phase has a significant range of composition from $5.84\text{-}5.95$ at 650 °C as shown in Fig. 3.3 (a). Similar behavior in $\text{YBaMn}_2\text{O}_{5+\delta}$ also occurs at higher temperatures, 700 and 750 °C, as presented in Fig. 3.3 (b-c), but the transitions between the phases shift to higher $p\text{O}_2$ at higher temperature. The results also indicate that the system is not completely reversible. On re-oxidation, there are unusual steps in the data that occur at $-\log p\text{O}_2 = 7.35, 7.71,$ and 7.77 at 650, 700, and 750 °C (Fig. 3.3 (a-c)), respectively, with very slow kinetics. The origin of this effect involves phase separation (see below for further discussion).

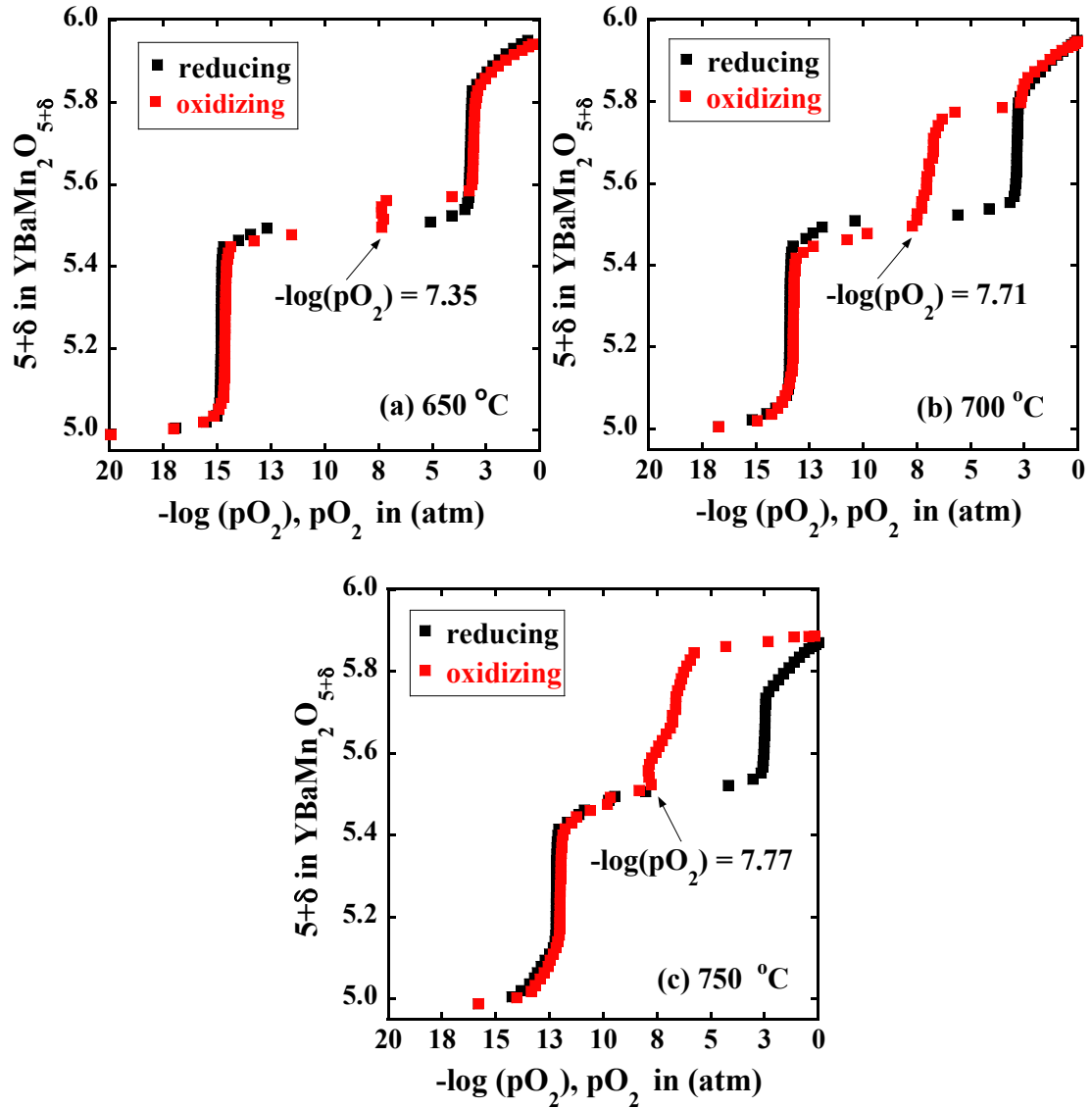


Fig 3.3 The $p\text{O}_2$ dependence of oxygen non-stoichiometry measured on reduction and re-oxidation of $\text{YBaMn}_2\text{O}_{5+\delta}$ at (a) 650 °C, (b) 700 °C, and (c) 750 °C.

Table 3.1 summarizes the composition ranges of each phase and the $p\text{O}_2$ of phase inter-conversion in $\text{YBaMn}_2\text{O}_{5+\delta}$. In the most oxidized O_6 phase, the oxygen content ($5+\delta$) is less than 6 at high temperature. This is not related to phase separation, but is expected because the degree of non-stoichiometry is altered by the increasing importance of $T\Delta s_0$. This is most evident for the compositions close to $\delta = 1.0$ where the enthalpy of

oxidation is smallest. While, final compositions ($5+\delta$) obtained in TGA experiments are very close to 6, as reported in Chapter 2, that depend on the atmosphere (air or oxygen) and how fast the sample was cooled. They do not represent the true equilibrium compositions at high temperature. Moreover, the pO_2 at which $O_{5.5+\delta}$ converts to $O_{5.5}$ is not effected by the phase separation. The temperature dependence of the pO_2 corresponding to the transition of O_5 to $O_{5.5}$ and $O_{5.5}$ to $O_{5.5+\delta}$ is shown in Figure 3.4. The values scale linearly with temperature.

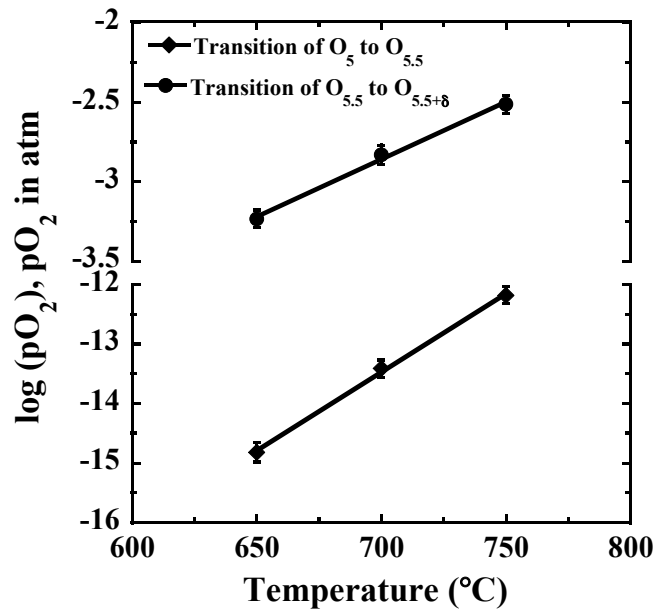


Fig. 3.4 The temperature dependence of pO_2 corresponding to the transitions from O_5 to $O_{5.5}$ and $O_{5.5}$ to $O_{5.5+\delta}$ for $YBaMn_2O_{5+\delta}$. The data were collected on reduction.

Table 3.1 Composition ranges of each phase and the pO_2 of phase inter-conversion in $YBaMn_2O_{5+\delta}$ at 650, 700, and 750 °C.

Temperature (°C)	O ₅ phase composition range	-log pO ₂ of the transition between O ₅ and O _{5.5}	O _{5.5} phase composition range	-log pO ₂ of the transition between O _{5.5} and O ₆	O ₆ phase composition range
650	4.99 - 5.02	14.82 ± 0.06	5.46 - 5.54	3.23 ± 0.06	5.84 - 5.95
700	5.00 - 5.07	13.41 ± 0.05	5.47 - 5.55	2.83 ± 0.06	5.83 - 5.95
750	4.99 - 5.11	12.18 ± 0.05	5.43 - 5.54	2.51 ± 0.06	5.75 - 5.87

In comparison, Motohashi *et al.*[11] recently reported the results for the pO_2 of the transition between $O_{5.5}$ and O_6 phases in $YBaMn_2O_{5+\delta}$ using the TGA measurements. Their results show that the transition between $O_{5.5}$ and O_6 phases occurred approximately at $-\log pO_2 = 3.40, 2.71, 2.46$ at 650, 700 and 750 °C, respectively, which are in good agreement with the present data given in Table 3.1.

3.3.1.2 Kinetics effect and phase stability

The kinetic regimes during oxidation and reduction in $YBaMn_2O_{5+\delta}$ were observed from coulometric titration experiments. As an example, Figure 3.5 presents equilibrium times for oxidation and reduction as a function of oxygen non-stoichiometry at 650 °C. The chosen criterion for equilibrium was 0.001% change in the sensor voltage per minute.

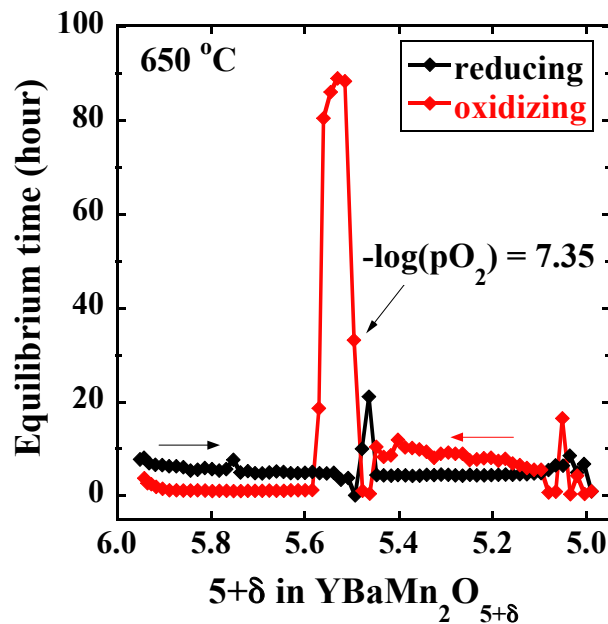


Fig. 3.5 Equilibrium times as a function of non-stoichiometry for $YBaMn_2O_{5+\delta}$ at 650 °C.

On reduction, the equilibrium times were ~ 5 h per point except near the inter-conversion of O_5 and $O_{5.5}$ where they were much longer (~ 15 h per point). This is consistent with the observation that $O_{5.5}$ is not observed on rapid oxidation of O_5 in oxygen or air due to the slow inter-conversion between O_5 and $O_{5.5}$, as seen in the thermogravimetric data in Chapter 2. On re-oxidation, the equilibrium times for $YBaMn_2O_{5+\delta}$ during the transition between O_5 and $O_{5.5}$ were varied between ~ 5 -10 h per point. Until the system reached to an unusual step that occurs at $-\log pO_2 = 7.35$ at 650 °C (Fig. 3.3 (a)), at which the data are in the vicinity of $O_{5.5}$ phase, the kinetics associated with these discontinuities are extremely slow (up to ~ 90 h per point). This unusual feature was also observed at higher temperatures, 700 and 750 °C, in the data occurring at $-\log pO_2 = 7.71$ and 7.77 (Fig. 3.3 (b-c)), respectively. The higher the temperature is; the longer range of the discontinuities is detected. Eventually, the data rejoin the curve obtained on reduction at 650 and 700 °C, but at 750 °C it was necessary to relax the criterion for equilibrium to obtain a fully oxidized sample. The system is not completely reversible on re-oxidation due to phase separation as evidenced by the slow kinetics. The products after the experiments at 700 and 750 °C were collected and analyzed by powder X-ray diffraction. The diffraction patterns confirmed that partial and complete decomposition to $BaMnO_{3-\delta}$ and $YMnO_3$ occurred at 700 and 750 °C, respectively, as shown in Figure 3.6.

At higher temperature (800 °C), it was not possible to reach equilibrium in the reduction reaction starting at a composition of O_6 because phase separation to $BaMnO_{3-\delta}$ and $YMnO_3$ occurred at the high pO_2 and temperature. According to literature data [69], we expect $\delta \approx 0$ for $BaMnO_{3-\delta}$, and consequently the average Mn oxidation state and total

oxygen content are the same for YBaMn_2O_6 and for the phase separated products at high $p\text{O}_2$ (~ 1 atm).

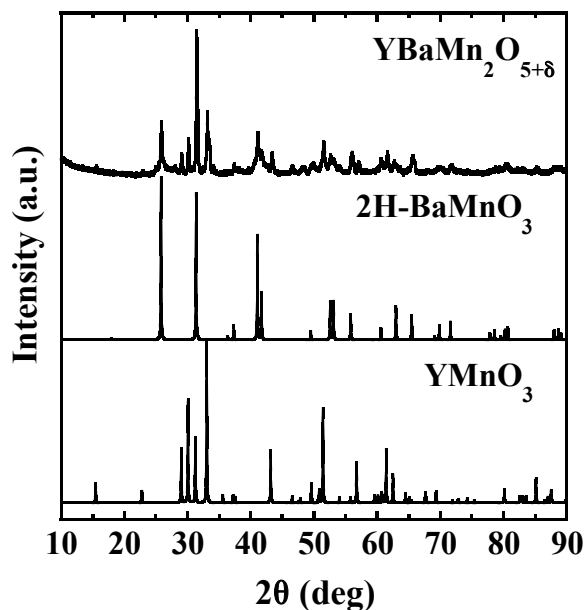


Fig. 3.6 X-ray data for $\text{YBaMn}_2\text{O}_{5+\delta}$ collected after re-oxidation by Coulometric titration at 750 °C, compared with the X-ray diffraction patterns of 2H-BaMnO_3 and YMnO_3 obtained from the ICSD database.

3.3.2 Coulometric titration of $\text{GdBaMn}_2\text{O}_{5+\delta}$

3.3.2.1 Oxygen non-stoichiometry

The stoichiometry changes ($\Delta\delta$) of $\text{GdBaMn}_2\text{O}_{5+\delta}$ were determined in the $p\text{O}_2$ range of $\sim 10^{-23} \leq p\text{O}_2$ (atm) $\leq \sim 1$ at four temperatures 600, 650, 700, and 750 °C. The initial experiments on Gd-sample showed some decomposition at certain $p\text{O}_2$ values during re-oxidation with very slow kinetics similar to that observed in $\text{YBaMn}_2\text{O}_{5+\delta}$, as previously discussed (see below for further discussion). Consequently, separate experiments were made in low and high- $p\text{O}_2$ regions in order to avoid decomposition that occurs in the middle $p\text{O}_2$ range. The measurements were made on both decreasing and

increasing pO_2 . A variation in the YSZ sensor voltage of less than 0.005% min^{-1} was chosen as the criteria for equilibrium.

In the low- pO_2 region, the data were obtained starting with a composition (δ) = 0. Before measurements, the cell was pumped out to ensure that there was no oxidation occurred during the sealing process, and the composition $\delta = 0$ was the real starting point. In the measurements, oxygen was pumped in until the composition reached the plateau where $\delta = 0.5$. At this point the oxygen was pumped out to go back to $\delta = 0$. The oxidation-reduction process was reversible indicating no decomposition, and the change in δ was 0.5. The high- pO_2 data were obtained beginning with a composition (δ) close to 1.0. On reduction, oxygen was then pumped out until the plateau at $\delta = 0.5$ was reached, and the data overlapped the low- pO_2 data. There is no decomposition observed on reduction. On re-oxidation, however, some decomposition at high pO_2 was indicated by slow kinetics (see below). Consequently, only the reduction data of $\text{GdBaMn}_2\text{O}_{5+\delta}$ in low and high- pO_2 regions are presented in Figure 3.7.

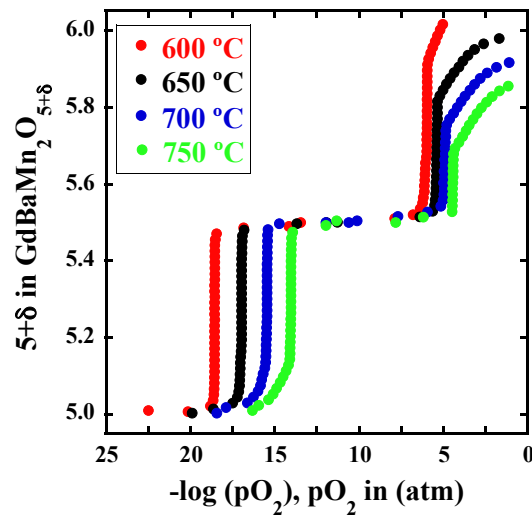


Fig. 3.7 The dependence of oxygen non-stoichiometry on pO_2 measured on reduction at different temperatures for $\text{GdBaMn}_2\text{O}_{5+\delta}$.

The results show that three phases clearly are present in the variation of the oxygen content with pO_2 . At 600 °C, two phases have narrow ranges of composition with oxygen contents $(5+\delta) = 5.00-5.01$ and $5.49-5.52$. The most oxidized phase has a significant range of composition from $5.94-6.02$ at 600 °C. Similar behavior also occurs at 650, 700, and 750 °C, but the phases inter-convert at higher pO_2 as the temperature increases. Table 3.2 summarizes the composition ranges of each phase, and the pO_2 of phase inter-conversion at different temperatures. In the most oxidized phase, the range of stoichiometry, (δ) , in $GdBaMn_2O_{5.5+\delta}$ increases with temperature. The oxygen contents $(5+\delta)$ vary from $5.94-6.02$ at 600 °C to $5.71-5.86$ at 750 °C. The pO_2 values for phase inter-conversion of O_5 to $O_{5.5}$ and of $O_{5.5}$ to $O_{5.5+\delta}$ are linearly with the temperature, as shown in Figure 3.8.

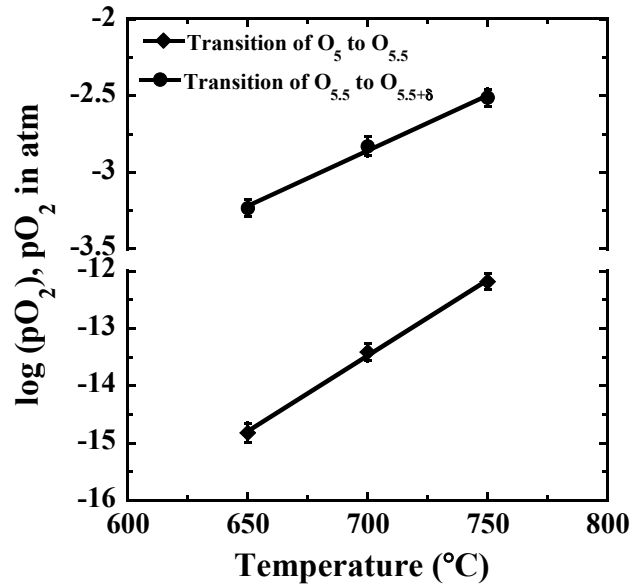


Fig. 3.8 The temperature dependence of pO_2 corresponding to the transitions from O_5 to $O_{5.5}$ and $O_{5.5}$ to $O_{5.5+\delta}$ for $GdBaMn_2O_{5+\delta}$. The data were measured on reduction.

Table 3.2 Composition ranges of each phase and the pO_2 of phase inter-conversion in $GdBaMn_2O_{5+\delta}$ at 600, 650, 700, and 750 °C.

Temperature (°C)	O ₅ phase composition range	-log pO ₂ for the transition between O ₅ and O _{5.5}	O _{5.5} phase composition range	-log pO ₂ for the transition between O _{5.5} and O ₆	O ₆ phase composition range
600	5.00 - 5.01	18.57 ± 0.05	5.49 - 5.52	6.03 ± 0.11	5.94 - 6.02
650	5.00 - 5.01	17.00 ± 0.11	5.50 - 5.51	5.41 ± 0.08	5.85 - 5.98
700	5.00 - 5.09	15.48 ± 0.06	5.50 - 5.52	4.92 ± 0.05	5.77 - 5.92
750	5.01 - 5.11	14.05 ± 0.04	5.49 - 5.51	4.44 ± 0.04	5.71 - 5.86

In addition, the present results for $\text{GdBaMn}_2\text{O}_{5+\delta}$ in the high- $p\text{O}_2$ region at 700 °C can be compared with the data presented by Taskin *et al.* [70]. Based on their results, the equilibrium oxygen content of $\text{GdBaMn}_2\text{O}_{5+\delta}$ decreased approximately from 5.99 to 5.84 with a change in $-\log p\text{O}_2$ from 0.006 to 5.01 at 700 °C. The upper value of oxygen content with $p\text{O}_2$ value at 700 °C reported in the present data is in a good agreement, but the data at 700 °C given in Fig. 3.7 show the phase inter-conversion from $\text{O}_{5.5+\delta}$ to $\text{O}_{5.5}$ begins at $-\log p\text{O}_2 = 4.81$, and is complete at an oxygen content of 5.56 at $-\log p\text{O}_2 = 5.02$. The sharp change in composition to $\text{O}_{5.5}$ was not observed by Taskin *et al.* [70].

3.3.2.2 Kinetics and phase stability

As an example, the equilibrium times for oxidation and reduction of $\text{GdBaMn}_2\text{O}_{5+\delta}$ at 650 °C in the low- $p\text{O}_2$ region are shown in Figure 3.9 as a function of oxygen non-stoichiometry. The chosen criterion for equilibrium was 0.005% change in the sensor voltage per minute. Equilibrium times for $\text{GdBaMn}_2\text{O}_{5+\delta}$ during the transition between O_5 and $\text{O}_{5.5}$ were ~3 h per point on reduction, and ~1 h per point on oxidation. They were significantly longer in the vicinity of $\text{O}_{5.5}$ (up to ~23 h per point on both reduction and oxidation), indicating slow inter-convert between O_5 and $\text{O}_{5.5}$. The results show that the reaction kinetics of reduction are slower than that of oxidation. In addition, very slow kinetics were observed near a single phase of O_5 , where equilibrium times for reduction and oxidation were ~29 and ~10 h, respectively.

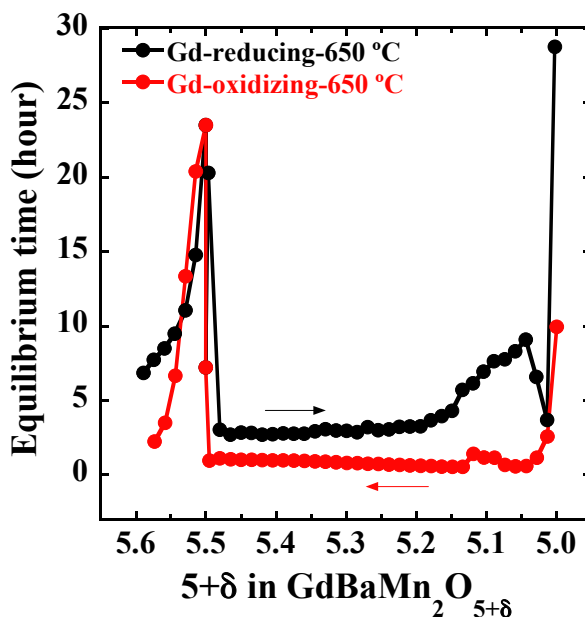


Fig. 3.9 Equilibrium times as a function of oxygen non-stoichiometry at 650 °C for GdBaMn₂O_{5+δ}. The criterion for equilibrium was 0.005% min⁻¹.

Decomposition of GdBaMn₂O_{5+δ} at high pO₂ was also observed as found in YBaMn₂O_{5+δ} previously reported. Figure 3.10 (a) show the results in initial experiments for GdBaMn₂O_{5+δ} at 700 °C measured on reduction/oxidation over the whole region of pO₂. During re-oxidation, an unusual step occurs at -log pO₂ = 6.75. The kinetics associated with this step are extremely slow. As discussed above, in subsequent experiments the low and high-pO₂ regions were measured separately to avoid decomposition. The equilibrium times of GdBaMn₂O_{5+δ} at 700 °C in the initial experiments are shown in Figure 3.10 (b) as a function of oxygen non-stoichiometry. With a criterion of 0.008% min⁻¹, on reduction the equilibrium times were ~2 h per point, except in the vicinity of the inter-conversion of O₅ and O_{5.5} where they were significantly longer (up to ~45 h per point). On re-oxidation, the equilibrium times were slow starting at -log pO₂ = 6.75, and varied between ~20 to 40 h per point above that step. The system

is not reversible on re-oxidation due to phase separation as indicated by the slow kinetics. The product after the experiment was analyzed by powder X-ray diffraction. The diffraction patterns confirmed that complete decomposition to $\text{BaMnO}_{3-\delta}$ and GdMnO_3 occurred at 700 °C, as shown in Figure 3.11.

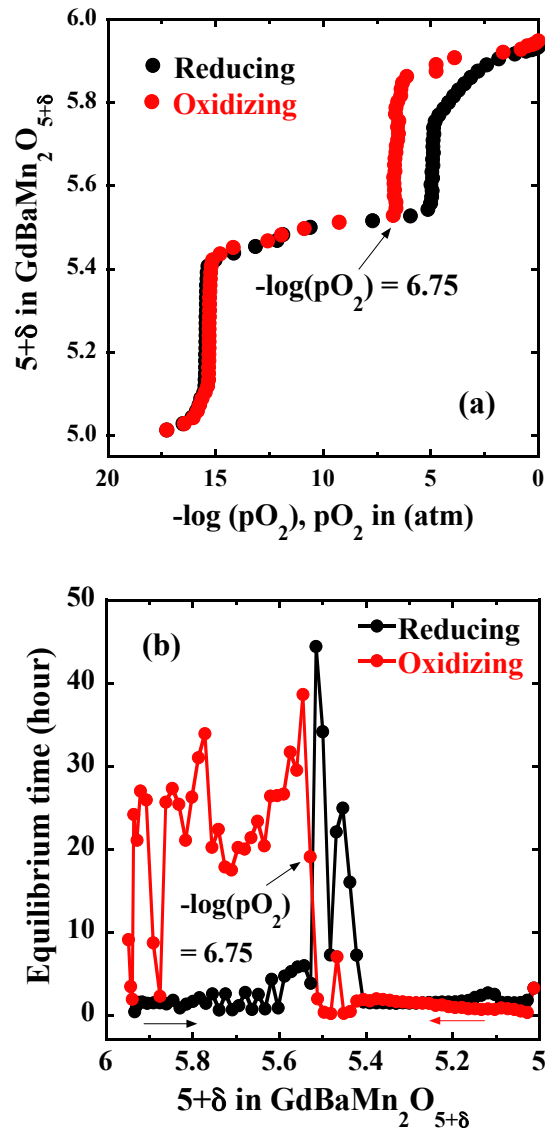


Fig. 3.10 (a) The oxygen non-stoichiometry of $\text{GdBaMn}_2\text{O}_{5+\delta}$ as a function of $p\text{O}_2$ obtained on reduction/oxidation at 700 °C in the initial experiments; (b) Equilibrium times as a function of oxygen non-stoichiometry at 700 °C. The criterion for equilibrium was $0.008\% \text{ min}^{-1}$.

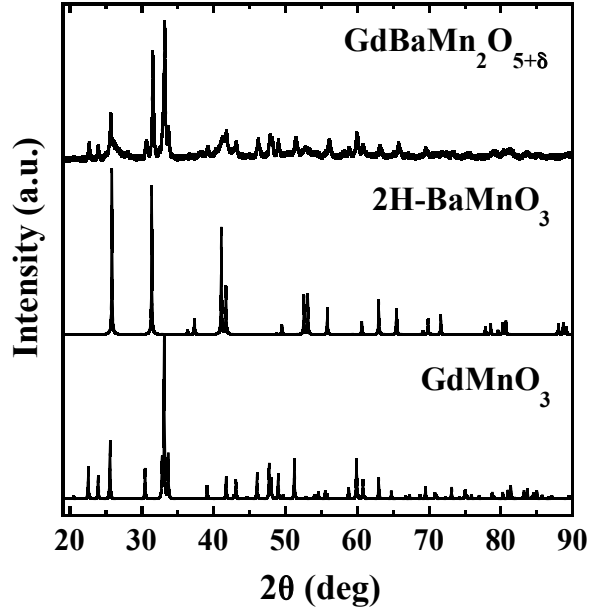


Fig. 3.11 X-ray data for $\text{GdBaMn}_2\text{O}_{5+\delta}$ collected after re-oxidation by Coulometric titration at $700\text{ }^\circ\text{C}$, and the corresponding data for 2H-BaMnO_3 and GdMnO_3 obtained from the ICSD database.

3.3.3 Coulometric titration of $\text{PrBaMn}_2\text{O}_{5+\delta}$

3.3.3.1 Oxygen non-stoichiometry

The coulometric titration experiments of $\text{PrBaMn}_2\text{O}_{5+\delta}$ were also carried out separately at low and high- $p\text{O}_2$ regions in order to avoid the occurrence of decomposition as previously observed in $\text{YBaMn}_2\text{O}_{5+\delta}$. Measurements were done in sealed electrochemical cells on both decreasing and increasing $p\text{O}_2$ at 600, 650, 700, and 750 $^\circ\text{C}$. A variation in the YSZ sensor voltage of less than $0.005\% \text{ min}^{-1}$ (at 650 $^\circ\text{C}$) and $0.01\% \text{ min}^{-1}$ (at 650, 700, and 750 $^\circ\text{C}$) was chosen as the criterion for equilibrium. However, the decomposition is more pronounced, especially at high $p\text{O}_2$ ($\sim 1 \text{ atm}$), in $\text{PrBaMn}_2\text{O}_{5+\delta}$. Consequently, only low- $p\text{O}_2$ data were considered reliable, and presented here.

The $p\text{O}_2$ dependence of oxygen non-stoichiometry for $\text{PrBaMn}_2\text{O}_{5+\delta}$ at 600, 650, 700, and 750 $^\circ\text{C}$ in low- $p\text{O}_2$ region are illustrated in Fig. 3.12. The experiments in low-

pO_2 region were done the same way as for $GdBaMn_2O_{5+\delta}$ previously discussed. The data were obtained starting with a sample of oxygen content $(5+\delta) = 5.0$. The cell was pumped out before the measurements to ensure that no oxidation occurred during the sealing process. In the measurements, oxygen was pumped in until the data reached the plateau where the oxygen content $(5+\delta) = 5.5$, then the oxygen was pumped out to go back to oxygen content $(5+\delta) = 5.0$. The oxidation-reduction was reversible without the occurrence of decomposition, and the change in δ was 0.5. From Fig. 3.12, at 600 °C two distinct phases exist in low- pO_2 region with oxygen content $(5+\delta) = 5.00$ - 5.02 and 5.48 - 5.49 . Similar behavior was observed at higher temperatures, but the transition between these two phases moves to higher pO_2 with increasing temperature. The results for $PrBaMn_2O_{5+\delta}$ at 600, 650, 700, and 750 °C are summarized in Table 3.3. The pO_2 value at which O_5 converts to $O_{5.5}$ is linearly dependent on temperature, as shown in Fig. 3.13.

Table 3.3 Composition ranges of each phase and the pO_2 of phase inter-conversion in $PrBaMn_2O_{5+\delta}$ at 600, 650, 700, and 750 °C in low- pO_2 region.

Temperature (°C)	O_5 phase composition range	$-\log pO_2$ for the transition between O_5 and $O_{5.5}$	$O_{5.5}$ phase composition range
600	5.00 - 5.02	22.05 ± 0.08	5.48 - 5.49
650	5.00 - 5.07	20.21 ± 0.06	5.47 - 5.49
700	4.99 - 5.11	18.45 ± 0.07	5.48 - 5.50
750	5.00 - 5.15	16.85 ± 0.05	5.49 - 5.52

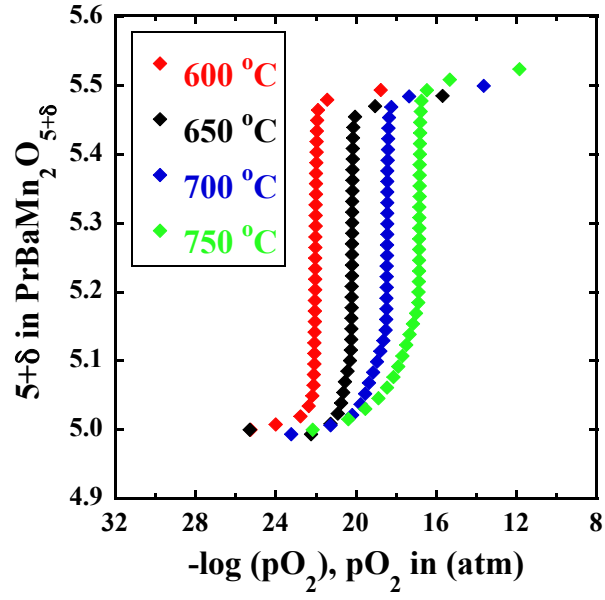


Fig. 3.12 The pO_2 dependence of oxygen non-stoichiometry in the low- pO_2 region for $PrBaMn_2O_{5+\delta}$ measured on reduction at different temperatures.

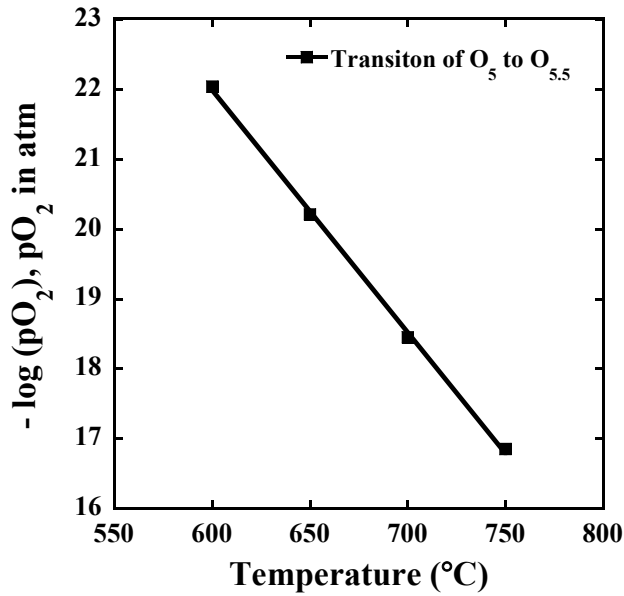


Fig. 3.13 The temperature dependence of pO_2 corresponding to the transitions from O_5 to $O_{5.5}$ for $PrBaMn_2O_{5+\delta}$. The data were measured on reduction.

Due to decomposition at high pO_2 (~ 1 atm), reduction experiments starting with the most oxidized $PrBaMn_2O_{5+\delta}$ were not successful at any temperature. At high pO_2 ; decomposition was indicated by very long equilibrium times. However, $PrBaMn_2O_6$ was observed on rapid oxidation of $PrBaMn_2O_5$ in air or oxygen using TGA experiments, as previously reported in Chapter 2.

In comparison, a report on the oxygen non-stoichiometry of $PrBaMn_2O_{5+\delta}$ as a function of pO_2 at 650, 700, and 750 °C was recently published by Sengodan *et al.* [2]. Base on their results, the oxygen content changed from ~ 5.74 to 5.00 during reduction in the $-\log pO_2$ range between ~ 1.25 and ~ 24 without indication of the phase transition step between O_5 and $O_{5.5}$, whereas the current data at 650, 700 and 750 °C illustrated in Fig. 3.12 clearly show the inter-conversion step between O_5 and $O_{5.5}$ phases on reduction.

3.3.3.2 Kinetics and phase stability

The regime of reaction kinetics in $PrBaMn_2O_{5+\delta}$ was observed in low- pO_2 region. As an example, the equilibrium times for oxidation and reduction of $PrBaMn_2O_{5+\delta}$ at 650 °C are shown in Figure 3.14 as a function of oxygen non-stoichiometry. A criterion for equilibrium was 0.005% of change in the sensor voltage per minute.

Equilibrium times for $PrBaMn_2O_{5+\delta}$ during the transition between O_5 and $O_{5.5}$ were ~ 3 and ~ 1 h per point on reduction and oxidation, respectively. They were longer near the phase boundary of $O_{5.5}$ (up to ~ 4.5 h per point on both reduction and oxidation), and significantly longer near a single phase of O_5 (~ 12.5 h per point on reduction, and ~ 4 h per point on oxidation). The results show that the reduction is slower than oxidation.

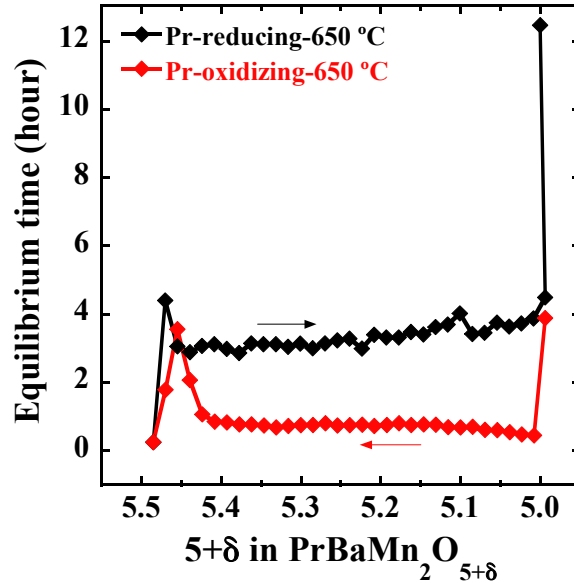


Fig. 3.14 Equilibrium times as a function of oxygen non-stoichiometry at 650 °C for $\text{PrBaMn}_2\text{O}_{5+\delta}$. The criterion for equilibrium was $0.005\% \text{ min}^{-1}$.

In summary, slow reaction kinetics in the systems of $\text{LnBaMn}_2\text{O}_{5+\delta}$ ($\text{Ln} = \text{Y}, \text{Gd}$, and Pr) are observed under two circumstances. First, when one phase converts to another phase, e.g., $\text{GdBaMn}_2\text{O}_5$ converts to $\text{GdBaMn}_2\text{O}_{5.5}$, or $\text{PrBaMn}_2\text{O}_5$ converts to $\text{PrBaMn}_2\text{O}_{5.5}$. The conversion is slow because it requires nucleation and growth of a different crystal structure. This effect is clearly presented in Fig. 3.9 and Fig. 3.14, which show that the kinetics are slower near phase boundaries. After nucleation occurs, the kinetics speed up again. In contrast, when phase separation occurs, the kinetics behavior is very slow over a wide range of composition. This is illustrated for $\text{GdBaMn}_2\text{O}_{5+\delta}$ in Fig. 3.10. On reduction, the kinetics slow down at the phase boundary, and then speed up again (nucleation). On re-oxidation, above $-\log p\text{O}_2 = 6.75$ (at 700 °C) the kinetics are very slow and remain slow until the final composition is reached (phase separation). The X-ray data show that this effect corresponds to complete phase separation. The kinetic

measurements are thus a very important probe of the phase behavior in these experiments.

3.3.4 Effect of A-site cationic substitution on phase conversion

As above discussed, the variation of the oxygen stoichiometry with pO_2 was investigated for $LnBaMn_2O_{5+\delta}$ series by means of coulometric titration in isothermal experiments at 600, 650, 700, and 750 °C. The pO_2 values corresponding to the transition of O_5 to $O_{5.5}$ for $LnBaMn_2O_{5+\delta}$ ($Ln = Y, Gd, \text{ and } Pr$) were plotted as a function of temperature (Fig. 3.15 (a)), and ionic size of the Ln^{3+} ion (Fig. 3.15 (b)). The values increase linearly with temperature, and a value of $-\log pO_2 = 16.11$ was obtained for Y-compound at 600 °C by extrapolation of the higher temperature values. The pO_2 values at which O_5 converts to $O_{5.5}$ scale nearly linearly with the Ln^{3+} ionic radius, as seen in Fig. 3.15 (b).

In the high- pO_2 region, the values of pO_2 at the transition from $O_{5.5}$ to $O_{5.5+\delta}$ in $PrBaMn_2O_{5+\delta}$ could not be measured because of decomposition at the long times needed to reach equilibrium. An estimate was made by linear extrapolation of the data for Y- and Gd-compounds with ionic radius. The pO_2 values of $O_{5.5}$ -to- $O_{5.5+\delta}$ inter-conversion for $PrBaMn_2O_{5+\delta}$ were predicted to occur approximately at $-\log pO_2 = 10.1, 9.4$ and 8.6 at 650, 700, and 750 °C, respectively. This is in a good agreement with the observation in TGA experiments on $PrBaMn_2O_{5+\delta}$ that $O_{5.5}$ is not observed on rapid reduction of O_6 in N_2 atmosphere ($pO_2 \approx 10^{-4}$ atm); the oxygen partial pressure is not low enough even when the compound was heated to 980 °C (see Chapter 2).

As a result, the data indicate that the reduction occurs at higher pO_2 (is easier) for both transitions on substitution of lanthanides in $LnBaMn_2O_{5+\delta}$ with smaller Ln^{3+} radius, consistent with the TGA experiments.

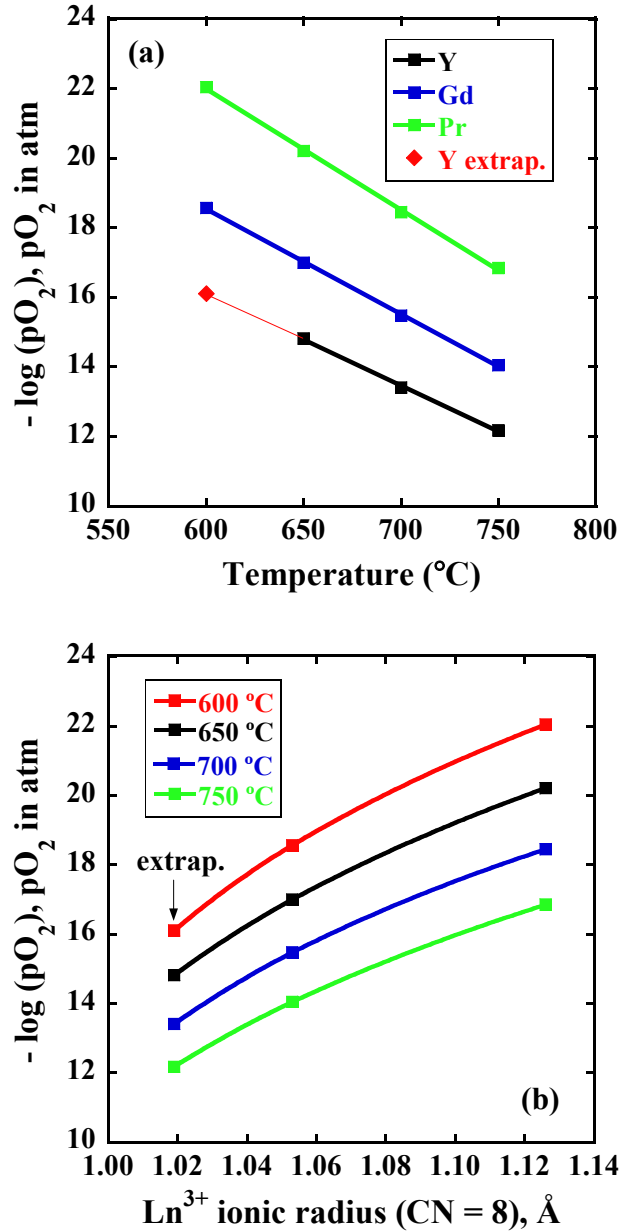


Fig. 3.15 The variation of pO_2 at the transition from O_5 to $O_{5.5}$ for $LnBaMn_2O_{5+\delta}$ (Ln = Y, Gd, and Pr) with (a) temperature, and (b) the Ln^{3+} (CN = 8) ionic size at different temperatures. The data were measured on reduction.

3.3.5 Thermodynamics

Thermodynamic quantity on oxides can be obtained by measuring the equilibrium stoichiometry as a function of the oxygen fugacity, pO_2 , which is in equilibrium with the oxides at different temperatures. Figure 3.16 (a-c) presents the partial molar free energy of oxygen atom ($\Delta\mu_O$) at equilibrium between the solid oxide and the gas phase, calculated from the reduction data of $YBaMn_2O_{5+\delta}$, $GdBaMn_2O_{5+\delta}$, and $PrBaMn_2O_{5+\delta}$ in Fig. 3.3, 3.7, and 3.12, respectively.

The data for the Y-, Gd-, and Pr-compounds in low- pO_2 region show two-phase region corresponding to the reaction: $2LnBaMn_2O_{5.0} (s) + 1/2O_2 (g) \rightarrow 2LnBaMn_2O_{5.5} (s)$, and $LnBaMn_2O_{5.0}$ has a small range of stoichiometry at 700 and 750 °C (~5.0 to 5.1 for the Y- and Gd-compounds, and ~5.0 to 5.2 for the Pr-compound; see Table 3.1-3.3). The average values of partial molar free energy ($\Delta\mu_O$) for the Y-, Gd-, and Pr-compounds in oxidation from $LnBaMn_2O_{5.0}$ to $LnBaMn_2O_{5.5}$ are summarized in Table 3.4. As a function of temperature, the results indicate that the partial molar free energy on oxidation is less negative with increasing temperature for the three compounds, and the oxidation of O_5 to $O_{5.5}$ is exergonic. Comparing between the three compounds, the average values of $\Delta\mu_O$ for the conversion from $O_{5.0}$ to $O_{5.5}$ at 650 °C equal -131.0, -150.2, and -178.6 kJ/mol for the Y-, Gd- and Pr-compounds, respectively. A similar trend is also observed at the higher temperatures, 700 and 750 °C. This indicates the influence of the ionic size of the Ln^{3+} cations in $LnBaMn_2O_{5+\delta}$ on $\Delta\mu_O$; the more negative value of $\Delta\mu_O$ is obtained from the compound with larger Ln^{3+} ionic radius.

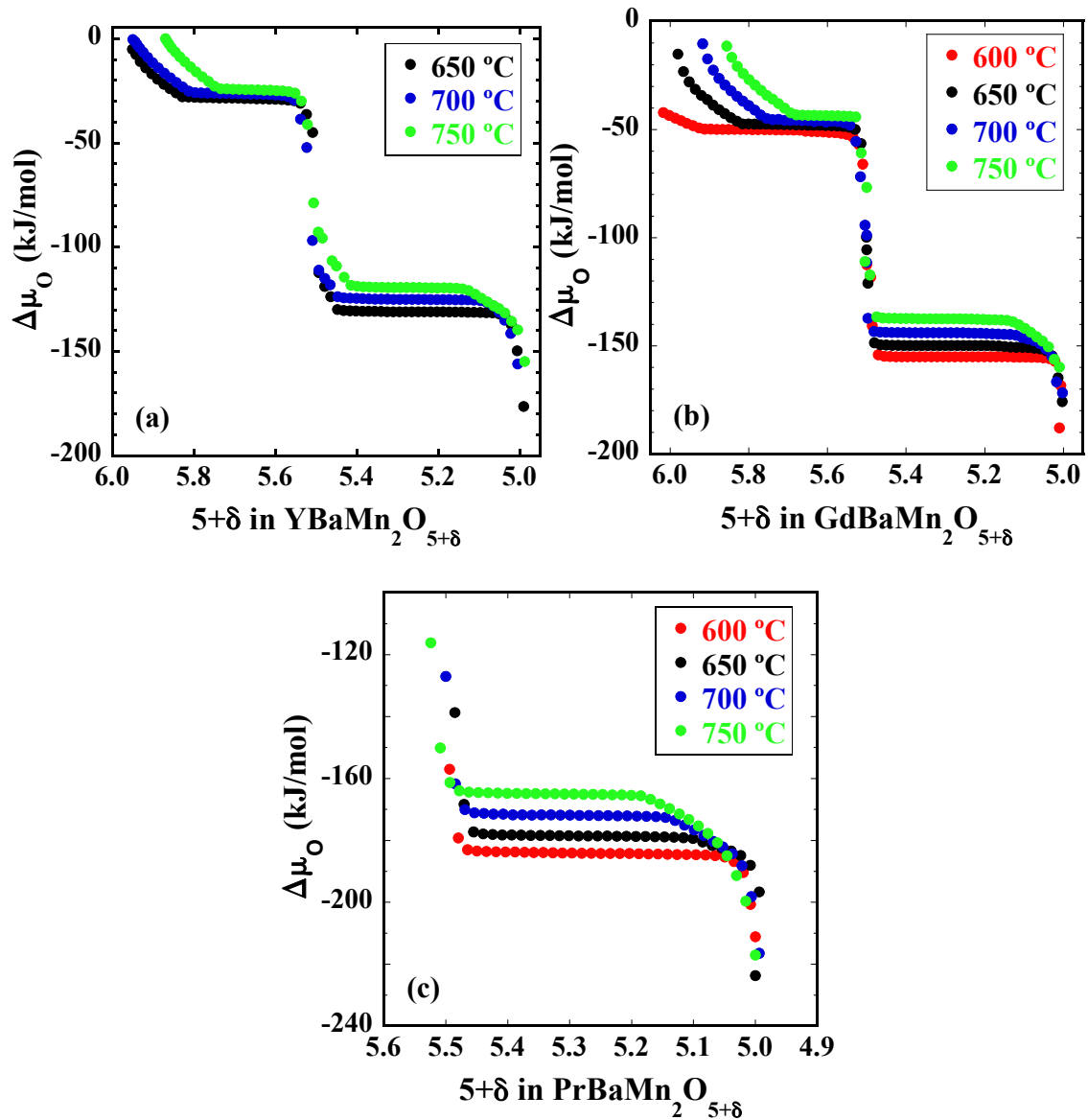


Figure 3.16 Partial molar free energy of oxygen atom ($\Delta\mu_{\text{O}}$) as a function of oxygen content for (a) $\text{YBaMn}_2\text{O}_{5+\delta}$, (b) $\text{GdBaMn}_2\text{O}_{5+\delta}$, and (c) $\text{PrBaMn}_2\text{O}_{5+\delta}$ at 600, 650, 700, and 750 °C.

In high- p_{O_2} region, only data for $\text{YBaMn}_2\text{O}_{5+\delta}$ and $\text{GdBaMn}_2\text{O}_{5+\delta}$ are shown in Fig 3.16 (a-b). The most oxidized phase appears to have a range of stoichiometry for both compounds, and the data clearly show the two-phase region of $\text{O}_{5.5}$ and the most oxidized phase ($\text{O}_{5.5+\delta}$). As shown in Table 3.4, the average values of $\Delta\mu_{\text{O}}$ for oxidation from $\text{O}_{5.5}$

to $O_{5.5+\delta}$ at 650, 700, and 750 °C, are -28.6, -26.4, and -24.6 kJ/mol for $YBaMn_2O_{5+\delta}$, and -47.8, -45.8, and -43.4 kJ/mol for $GdBaMn_2O_{5+\delta}$, respectively. The partial molar free energy becomes less negative as the temperature increases, and this reaction is exergonic. The effect of the size of Ln^{3+} ion substituted in $LnBaMn_2O_{5+\delta}$ on $\Delta\mu_o$ is also observed in high- pO_2 region.

Table 3.4 Partial molar free energy of oxygen atom ($\Delta\mu_o$) in low and high- pO_2 regions for $LnBaMn_2O_{5+\delta}$ ($Ln = Y, Gd, \text{ and } Pr$) at different temperatures.

Temperature (°C)	$\Delta\mu_o$ (kJ/mol)				
	Y		Gd		Pr
	low pO_2	high pO_2	low pO_2	high pO_2	low pO_2
600			-155.2	-50.4	-184.3
650	-131.0	-28.6	-150.2	-47.8	-178.6
700	-125.0	-26.4	-144.2	-45.8	-171.9
750	-119.3	-24.6	-137.6	-43.4	-165.0

As the temperature dependence of $\Delta\mu_o$, the partial molar enthalpy (Δh_o) and entropy (Δs_o) of oxygen atom can be extracted from the plots of $R/2 \times \ln(pO_2)$ versus $1/T$, and $RT/2 \times \ln(pO_2)$ versus T , respectively, as an example of $YBaMn_2O_{5.5+\delta}$ data in low- pO_2 region presented in Figure 3.17. Both plots of the Y-, Gd- and Pr-compounds are linear indicating that the enthalpy and entropy are constant in this narrow temperature range. The values for the changes in enthalpy (Δh_o) and entropy (Δs_o) of the three compounds are listed in Table 3.5.

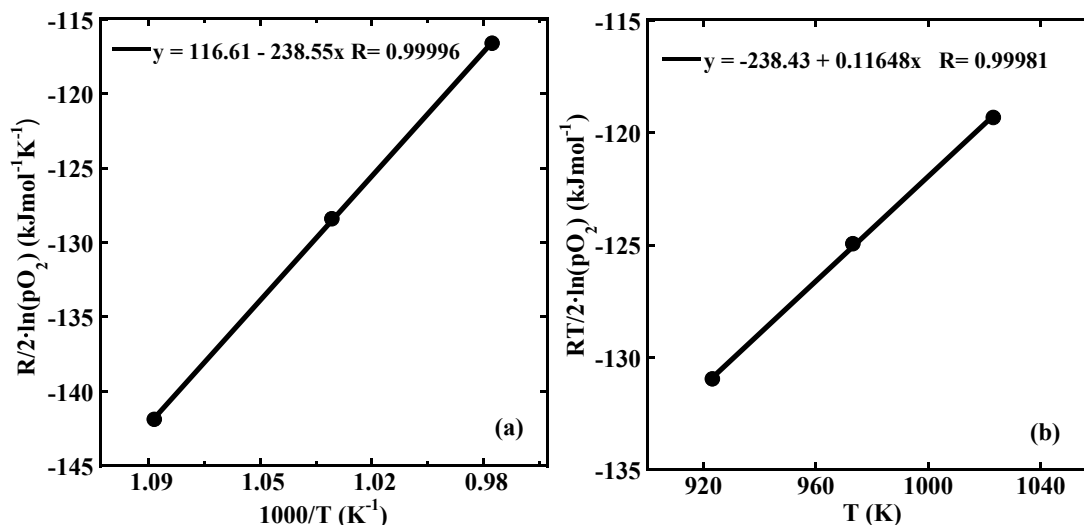


Fig. 3.17 The relation between (a) $R/2 \cdot \ln(pO_2)$ and $1/T$, and (b) between $RT/2 \cdot \ln(pO_2)$ and T of $YBaMn_2O_{5+\delta}$ in low- pO_2 region.

Table 3.5 A comparison of the values of the change in enthalpy (Δh_o) and entropy (Δs_o) for $LnBaMn_2O_{5+\delta}$ ($Ln = Y, Gd, \text{ and } Pr$) in low and high- pO_2 regions.

Data range	Value	Y	Gd	Pr
Low- pO_2 region	Δh_o (kJ mol ⁻¹)	-238.6	-257.7	-296.4
	Δs_o (J mol ⁻¹ K ⁻¹)	116.5	117.7	128.7
High- pO_2 region	Δh_o (kJ mol ⁻¹)	-65.1	-90.0	
	Δs_o (J mol ⁻¹ K ⁻¹)	39.6	45.4	

3.4 Conclusions

The oxygen non-stoichiometries of $LnBaMn_2O_{5+\delta}$ ($Ln = Y, Gd, \text{ and } Pr$) were determined as a function of pO_2 at 600, 650, 700, and 750 °C by Coulometric titration technique. Two distinct phases (with $\delta \approx 0, 0.5$) and a third phase with a range of composition with the δ value approaching to ~ 1 are observed during oxidation/reduction. The phase transition occurs at higher pO_2 with increasing temperature. At constant temperature, the pO_2 for reduction of $LnBaMn_2O_{5+\delta}$ decreases as the size of the Ln^{3+}

cation increases. The thermodynamic quantities corresponding to the oxidation of $\text{LnBaMn}_2\text{O}_5$ to $\text{LnBaMn}_2\text{O}_{5.5}$ and of $\text{LnBaMn}_2\text{O}_{5.5}$ to $\text{LnBaMn}_2\text{O}_{6-x}$ were investigated. The phase instability with respect to the decomposition to $\text{BaMnO}_{3-\delta}$ and LnMnO_3 under some conditions (high $p\text{O}_2$, high temperature, long times) may be an issue of some concern for practical applications in oxygen storage technology.

3.5 References

1. Brett, D. J. L.; Atkinson, A.; Brandon, N. P.; Skinner, S. J. *Chem. Soc. Rev.* **2008**, *37*, 1568-1578.
2. Sengodan, S.; Choi, S.; Jun, A.; Shin, T. H.; Ju, Y.-W.; Jeong, H. Y.; Shin, J.; Irvine, J. T. S.; Kim, G. *Nat. Mater.* **2015**, *14* (2), 205-209.
3. Bhavsar, S.; Vesper, G. *RSC Adv.* **2014**, *4*, 47254-47267.
4. Dabrowski, B.; Remsen, S.; Mais, J.; Kolesnik, S. *Funct. Mater. Lett.* **2011**, *4* (2), 147-150.
5. Kašpar, J.; Fornasiero, P. *J. Solid State Chem.* **2003**, *171*, 19-29.
6. Motohashi, T.; Hirano, Y.; Masubuchi, Y.; Oshima, K.; Setoyama, T.; Kikkawa, S. *Chem. Mater.* **2013**, *25*, 372-377.
7. Shin, T. H.; Myung, J.-H.; Verbraeken, M.; Kim, G.; Irvine, J. T. S. *Faraday Discuss.* **2015**, *182*, 227-239.
8. Wei, Y.; Wang, H.; He, F.; Ao, X.; Zhang, C. *J. Nat. Gas Chem.* **2007**, *16* (1), 6-11.
9. Yang, Z.; Lin, Y. S.; Zeng, Y. *Ind. Eng. Chem. Res.* **2002**, *41*, 2775-2784.
10. Chen, X.; Jung, T.; Park, J.; Kim, W.-S. *J. Mater. Chem. A* **2015**, *3*, 258-265.
11. Motohashi, T.; Takahashi, T.; Kimura, M.; Masubuchi, Y.; Kikkawa, S.; Kubota, Y.; Kobayashi, Y.; Kageyama, H.; Takata, M.; Kitagawa, S.; Matsuda, R. *J. Phys. Chem. C* **2015**, *119*, 2356-2363.
12. Motohashi, T.; Kimura, M.; Inayoshi, T.; Ueda, T.; Masubuchi, Y.; Kikkawa, S. *Dalton Trans.* **2015**, *44*, 10746-10752.

13. Motohashi, T.; Ueda, T.; Masubuchi, Y.; Kikkawa, S. *J. Ceram. Soc. Jpn.* **2011**, *119* (11), 894-897.
14. Motohashi, T.; Ueda, T.; Masubuchi, Y.; Kikkawa, S. *J. Phys. Chem. C* **2013**, *117*, 12560-12566.
15. Świerczek, K.; Klimkowicz, A.; Zheng, K.; Dabrowski, B. *J. Solid State Chem.* **2013**, *203*, 68-73.
16. Świerczek, K.; Klimkowicz, A.; Niemczyk, A.; Olszewska, A.; Rząsa, T.; Molenda, J.; Takasaki, A. *Funct. Mater. Lett.* **2014**, *7* (6), 1440004.
17. Klimkowicz, A.; Świerczek, K.; Rząsa, T.; Takasaki, A.; Dabrowski, B. *Solid State Ionics* **2016**, *288*, 43-47.
18. Klimkowicz, A.; Świerczek, K.; Takasaki, A.; Molenda, J.; Dabrowski, B. *Mater. Res. Bull.* **2015**, *65*, 116-122.
19. Klimkowicz, A.; Świerczek, K.; Zheng, K.; Baranowska, M.; Takasaki, A.; Dabrowski, B. *Solid State Ionics* **2014**, *262*, 659-663.
20. Klimkowicz, A.; Zheng, K.; Fiolka, G.; Świerczek, K. *Chemik* **2013**, *67* (12), 1199-1206.
21. Jeamjumnunja, K.; Gong, W.; Makarenko, T.; Jacobson, A. J. *J. Solid State Chem.* **2015**, *230*, 397-403.
22. Jeamjumnunja, K.; Gong, W.; Makarenko, T.; Jacobson, A. J. *J. Solid State Chem.* **2016**, *239*, 36-45.
23. Millange, F.; Caignaert, V.; Domenge's, B.; Raveau, B. *Chem. Mater.* **1998**, *10* (7), 1974-1983.
24. Beales, T. P.; Molgg, M.; Jutson, J.; Friend, C. M. *Phys. Stat. Sol. A* **1997**, *161* (1), 271-282.
25. Chapman, J. P.; Attfield, J. P.; Molgg, M.; Friend, C. M.; Beales, T. P. *Angew. Chem. Int. Ed. Engl.* **1996**, *35* (21), 2482-2484.
26. McAllister, J. A.; Attfield, J. P. *J. Mater. Chem.* **1998**, *8* (5), 1291-1294.
27. Karppinen, M.; Okamoto, H.; Fjellvåg, H.; Motohashi, T.; Yamauchi, H. *J. Solid State Chem.* **2004**, *177*, 2122-2128.
28. Mizusaki, J.; Yoshihiro, M.; Yamauchi, S.; Fueki, K. *J. Solid State Chem.* **1985**, *58* (2), 257-266.

29. Mizusaki, J.; Mima, Y.; Yamauchi, S.; Fueki, K. *J. Solid State Chem.* **1989**, *80*, 102-111.
30. Kuo, J. H.; Anderson, H. U. *J. Solid State Chem.* **1989**, *83*, 52-60.
31. Osaka, M.; Sato, I.; Namekawa, T.; Kurosaki, K.; Yamanaka, S. *J. Alloys Compd.* **2005**, *397*, 110-114.
32. Mudu, F.; Arstad, B.; Bakken, E.; Fjellvåg, H.; Olsbye, U. *J. Catal.* **2010**, *275*, 25-33.
33. Bakken, E.; Dahl, P. I.; Haavik, C.; Stølen, S.; Larring, Y. *Solid State Ionics* **2011**, *182*, 19-23.
34. Osaka, M.; Miwa, S.; Kurosaki, K.; Uno, M.; Yamanaka, S. *J. Nucl. Mater.* **2011**, *408*, 285-288.
35. Pishahang, M.; Bakken, E.; Stølen, S.; Thomas, C. I.; Dahl, P. I. *Ionics* **2013**, *19*, 869-878.
36. Bulfin, B.; Hoffmann, L.; de Oliveira, L.; Knoblauch, N.; Call, F.; Roeb, M.; Sattler, C.; Schmucker, M. *Phys. Chem. Chem. Phys.* **2016**, *18*, 23147-23154.
37. Park, K.; Cackowski, T.; Markert, J. T. *Physica B* **2008**, *403*, 1561-1563.
38. Inprasit, T.; Wongkasemjit, S.; Skinner, S. J.; Burriel, M.; Limthongkul, P. *RSC Adv.* **2015**, *5*, 2486-2492.
39. Marinescu, C.; Vradman, L.; Tanasescu, S.; Navrotsky, A. *J. Solid State Chem.* **2015**, *230*, 411-417.
40. Sun, J.; Liu, X.; Han, F.; Zhu, L.; Bi, H.; Wang, H.; Yu, S.; Pei, L. *Solid State Ionics* **2016**, *288*, 54-60.
41. Sato, T.; Okiba, T.; Shozugawa, K.; Matsuo, M.; Fujishiro, F.; Niwa, E.; Hashimoto, T. *Solid State Ionics* **2016**, *290*, 71-76.
42. Elkalashy, S. I.; Aksenova, T. V.; Urusova, A. S.; Cherepanov, V. A. *Solid State Ionics* **2016**, *295*, 96-103.
43. Giddings, R. A.; Gordon, R. S. *J. Electrochem. Soc.* **1974**, *121* (6), 793-800.
44. Li-Zi, Y.; Zhi-Tong, S.; Chan-Zheng, W. *Solid State Ionics* **1992**, *50*, 203-208.
45. Li-Zi, Y.; Zhi-Tong, S.; Chan-Zheng, W. *J. Solid State Chem.* **1994**, *113*, 221-224.

46. Lankhorst, M. H. R.; Bouwmeester, H. J. M.; Verweij, H. J. *Solid State Chem.* **1997**, *133*, 555-567.
47. Yoo, J. *Solid State Ionics* **2004**, *175* (1-4), 55-58.
48. Park, C. Y.; Jacobson, A. J. *J. Electrochem. Soc.* **2005**, *152* (7), J65.
49. Park, C. Y.; Azzarello, F. V.; Jacobson, A. J. *J. Mater. Chem.* **2006**, *16*, 3624-3628.
50. Tsipis, E. V.; Patrakeeve, M. V.; Waerenborgh, J. C.; Pivak, Y. V.; Markov, A. A.; Gaczyński, P.; Naumovich, E. N.; Kharton, V. V. *J. Solid State Chem.* **2007**, *180*, 1902-1910.
51. Patrakeeve, M. V.; Leonidov, I. A.; Kozhevnikov, V. L. *J. Solid State Electrochem.* **2011**, *15*, 931-954.
52. Tanasescu, S.; Marinescu, C.; Maxim, F.; Sofronia, A.; Totir, N. *J. Solid State Electrochem.* **2010**, *15* (1), 189-196.
53. Leonidova, E. I.; Leonidov, I. A.; Patrakeeve, M. V.; Kozhevnikov, V. L. *J. Solid State Electrochem.* **2011**, *15* (5), 1071-1075.
54. Sengodan, S.; Kim, J.; Shin, J.; Kim, G. *J. Electrochem. Soc.* **2011**, *158* (11), B1373-B1379.
55. Park, S.; Choi, S.; Shin, J.; Kim, G. *J. Power Sources* **2012**, *210*, 172-177.
56. Pishahang, M.; Bakken, E.; Stølen, S. *Thermochim. Acta* **2012**, *543*, 137-141.
57. Sengodan, S.; Ahn, S.; Shin, J.; Kim, G. *Solid State Ionics* **2012**, *228*, 25-31.
58. Yoo, S.; Choi, S.; Shin, J.; Liu, M.; Kim, G. *RSC Adv.* **2012**, *2* (11), 4648.
59. Jun, A.; Yoo, S.; Gwon, O.-h.; Shin, J.; Kim, G. *Electrochim. Acta* **2013**, *89*, 372-376.
60. Pishahang, M.; Bakken, E.; Stølen, S.; Larring, Y.; Thomas, C. I. *Solid State Ionics* **2013**, *231*, 49-57.
61. Sengodan, S.; Kim, J.; Shin, J.; Kim, G. *ECS Trans.* **2013**, *57* (1), 1647-1654.
62. Lohne, Ø. F.; Phung, T. N.; Grande, T.; Bouwmeester, H. J. M.; Hendriksen, P. V.; Søgaard, M.; Wiik, K. *J. Electrochem. Soc.* **2014**, *161* (3), F176-F184.
63. Niedrig, C.; Wagner, S. F.; Menesklou, W.; Ivers-Tiffée, E. *Solid State Ionics* **2015**, *273*, 41-45.

64. Merkulov, O. V.; Naumovich, E. N.; Patrakeev, M. V.; Markov, A. A.; Bouwmeester, H. J. M.; Leonidov, I. A.; Kozhevnikov, V. L. *Solid State Ionics* **2016**, *292*, 116-121.
65. Steele, B. C. H. *Mater. Sci. Eng.* **1992**, *B13*, 79-87.
66. Ramamoorthy, R.; Dutta, P. K.; Akbar, S. A. *J. Mater. Sci.* **2003**, *38*, 4271-4282.
67. Skinner, S. J.; Kilner, J. A. *Mater. Today* **2003**, *6* (3), 30-37.
68. Park, J.-H.; Blumenthal, R. N. *J. Electrochem. Soc.* **1989**, *136* (10), 2867-2876.
69. Negas, T.; Roth, R. S. *J. Solid State Chem.* **1971**, *3*, 323-339.
70. Taskin, A. A.; Lavrov, A. N.; Ando, Y. *Appl. Phys. Lett.* **2005**, *86*, 091910.

CHAPTER 4

Electrical Conductivity and Thermal Expansion of $\text{YBaMn}_2\text{O}_{5+\delta}$

4.1 Introduction

The $\text{LnBaMn}_2\text{O}_{5+\delta}$ oxides belong to a family of A-site cation ordered perovskite with layer-type ordering which can be used in various applications as oxygen-storage materials [1]. In addition to oxygen-storage properties, these materials have been widely studied in terms of structural phase transitions, electrical and magnetic properties [2-15]. The crystal structure and phase transition of $\text{LnBaMn}_2\text{O}_{5+\delta}$ at elevated temperature were previously reported based on powder X-ray diffraction, neutron diffraction, and synchrotron X-ray diffraction [16-24]. The electronic phase diagram of the A-site ordered $\text{LnBaMn}_2\text{O}_6$ is known for $\text{Ln} = \text{Y}$, and La-Ho lanthanides. Three groups of compounds show different behavior, depending on the Ln^{3+} ionic radius [25-26]. Compounds with small cations (Y^{3+} , Ho^{3+} , Dy^{3+} , and Tb^{3+}) show three phase transitions, namely, structural, charge-ordering (metal-insulator), and antiferromagnetic (AF) transitions [27-29], whereas compounds with larger cations (Gd^{3+} , Eu^{3+} , and Sm^{3+}) have no structural transition [25]. Compounds with Nd^{3+} , Pr^{3+} , and La^{3+} cations exhibit metallic ferromagnetic transition, and followed by an A-type AF transition in $\text{PrBaMn}_2\text{O}_6$ and $\text{NdBaMn}_2\text{O}_6$ [30-32].

To expand the knowledge concerning possible applications, studies of the electrical conductivity and thermal expansion of $\text{LnBaMn}_2\text{O}_{5+\delta}$ oxides are needed to complete the information on this compound system. A literature survey produced data on the electrical conductivity and thermal-expansion data only for Er-, Nd-, and Pr-

containing materials. The electrical conductivity of reduced $\text{ErBaMn}_2\text{O}_5$ in 5 vol. % H_2 in Ar is of the order of $10^{-4} \text{ S cm}^{-1}$ at room temperature, and increases with increasing temperature with an activation energy (E_a) = 0.30(1) eV in the range 50-500 °C. In contrast, oxidized $\text{ErBaMn}_2\text{O}_6$ possesses much higher electrical conductivity in air with values of $\sim 0.2 \text{ S cm}^{-1}$ at room temperature and $\sim 40 \text{ S cm}^{-1}$ at near 500 °C [17]. Relatively low values of electrical conductivity were also found for reduced $\text{NdBaMn}_2\text{O}_5$ with an estimated activation energy (E_a) = 0.52 eV in the range 110-450 °C, and ~ 0.69 eV in range 450-550 °C in 5 vol. % H_2/Ar . The maximum conductivity of $\text{NdBaMn}_2\text{O}_5$ achieved at 550 °C is 0.06 S cm^{-1} , while significantly higher electrical conductivity is observed in oxidized $\text{NdBaMn}_2\text{O}_6$ namely 20 S cm^{-1} at 550 °C in air with $E_a \approx 0.14$ eV in 25-550 °C [22]. The average linear thermal-expansion coefficient determined for $\text{NdBaMn}_2\text{O}_5$ is $14.3 \times 10^{-6} \text{ K}^{-1}$ in 3% H_2/N_2 [22], and $\sim 15 \times 10^{-6} \text{ K}^{-1}$ in 5% H_2/He in 65-800 °C temperature range [21]. The average thermal-expansion value of $\sim 13.0 \times 10^{-6} \text{ K}^{-1}$ was reported for $\text{NdBaMn}_2\text{O}_{5.5}$ in 65-800 °C [21]. The average thermal-expansion coefficient for $\text{NdBaMn}_2\text{O}_6$ in air was found to lie in range of $14.2\text{-}14.8 \times 10^{-6} \text{ K}^{-1}$ in different temperature ranges. [20-22]. In addition, Sengodan *et al.* [33] recently reported the electrical conductivity of layered $\text{PrBaMn}_2\text{O}_{5+\delta}$ to be as high as 8.16 S cm^{-1} in 5% H_2 , and 91.5 S cm^{-1} in air. The thermal-expansion coefficient determined by dilatometry experiments is $17.7(2) \times 10^{-6} \text{ K}^{-1}$ for the reduced form in 5% $\text{H}_2/95\% \text{ Ar}$, and $16.8(2) \times 10^{-6} \text{ K}^{-1}$ for the oxidized form in air.

In this chapter, a preliminary investigation on the electrical conductivity of YBaMn_2O_5 using the four-probe DC method in an electrochemical cell under low- $p\text{O}_2$ region is reported. The linear thermal-expansion behavior of the three phases (O_5 , $\text{O}_{5.5}$,

and O₆) of YBaMn₂O_{5+δ} under different atmospheres was studied by using dilatometry measurements and high-temperature XRD studies. Differential scanning calorimetry (DSC) measurements were made on the LnBaMn₂O₆ (Ln = Y, Gd, Eu, Sm, Nd, and Pr) compounds.

4.2 Experimental Section

4.2.1 Pellet Fabrication and Sample Characterization

The powders of polycrystalline YBaMn₂O_{5+δ} were made *via* a solid-state reaction in a low oxygen partial pressure to prevent the formation of BaMnO_{3-δ}, as described in Chapter 2. The as-synthesized YBaMn₂O₅ powders were finely reground in a mortar with isopropanol medium for 1 h. About 4 grams of these powders were pelletized in a 25-mm diameter die by using hydraulic press (Carver, Inc.) at 2.2 metric tons for 3 min, and then cold isostatic press (Autoclave Engineers, Inc.) at a pressure of 30,000 psi for 2 min. The pellet was sintered at 1300 °C for 24 h under 10.0 ppm H₂/ N₂ gas atmosphere (Certified Master Class Calibration Standard, Air Liquide America Specialty Gases LLC), with a heating and cooling rate of 2 °C/min. After sintering, the circular pellet was polished by using grinder-polisher machine (ECOMET 3; Buehler, Ltd.), until the surface is shiny.

The density of the samples was measured by the Archimedes technique, and compared to the theoretical density. The calculation of the bulk density, δ_{bulk} is given by the following equation:

$$\delta_{bulk} = W_{dry} / (W_{sat} - W_{sus}) \quad (4.1)$$

where, W_{dry} is the dry mass after heating at 150 °C, W_{sat} is the saturated mass, and W_{sus} is the mass suspended in water. The density of the sintered YBaMn₂O₅ pellet in this experiment was ~95% of the theoretical value.

The phase purity of the YBaMn₂O₅ pellet was checked using powder X-ray diffraction in the range $10 \leq 2\theta \leq 90$ with Cu K α radiation ($\lambda = 1.54046 \text{ \AA}$) on a Phillips PANalytical X'Pert PRO diffractometer at room temperature. The lattice parameters were determined through Le Bail refinement using GSAS/EXPGUI software.

The surface morphologies of the YBaMn₂O₅ pellet were evaluated using a LEO-1525 scanning electron microscope (SEM) operating at an accelerating voltage of 15 kV. The chemical compositions of the sample were analyzed by an energy dispersive spectroscopy (EDS; AMETEK EDAX equipped on a JEOL JSM-6330F scanning electron microscope).

4.2.2 Electrical Conductivity

4.2.2.1 Sample preparation

The dense YBaMn₂O₅ pellet was cut into a rectangular bar with a dimension of 1.4 mm \times 1.9 mm \times 21.3 mm. Four Pt wires were used as electrodes for transporting the current and measuring the difference of the voltages across the sample, and attached to the rectangular bar with Pt paste, as presented in Fig. 4.1. L is the distance between two inside electrodes. To avoid the oxidation of YBaMn₂O₅ in air at ~250 °C, the sample bar was only heated at 100 °C for 2-3 h to dry Pt paste and make a good contact between the sample and electrodes.

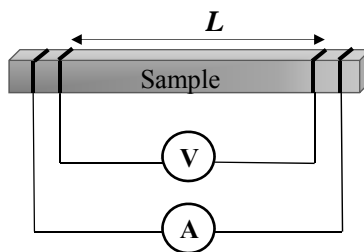


Fig. 4.1 Sample arrangement for the electrical conductivity experiments; L is the distance between two inside electrodes, A is the applied current, V is the measured voltage across the sample.

4.2.2.2 Theoretical background and experimental details

The variation of the electrical conductivity with temperature was measured by using a gas-tight electrochemical cell. As shown in Figure 4.2, the electrochemical cell is composed of an electrolyte (8-wt% polycrystalline yttria-stabilized zirconia, YSZ, disk), five alumina rings, eleven glass rings and an alumina container. The rectangular sample bar linked to four Pt wires was vertically placed in the middle of the cell with the alumina container at the bottom, and small pieces of capillary alumina tubes was placed inside the cell to support the sample bar and reduce the cell volume. The top of the cell was closed with the YSZ disk connected to two Pt wires and Pt meshes. The YSZ disk was used for pumping oxygen in/out of the cell and as a sensor monitoring pO_2 inside the cell with air as the reference gas on the outside. Six Pt wires from both the YSZ disk and the sample bar were brought out of the cell through the glass rings. The cell was then installed in the same apparatus as used for the coulometric titration as illustrated in Fig 3.2. The whole cell was pressed by the springs at the top of the apparatus to help for the sealing process. A thermocouple (R-type) was placed just above the cell to monitor the temperature. The gas-tight seals were made by heating the cell above the softening temperature (~ 750 °C)

of the glass rings. The total height of the cell was less than 35 mm after sealing. A Keithley 2400 Source Meter was used to provide the current for the oxygen pump and to monitor the YSZ sensor voltage. The experiments were controlled by LabView software. The values of oxygen partial pressure were calculated by using Eq. (3.2).

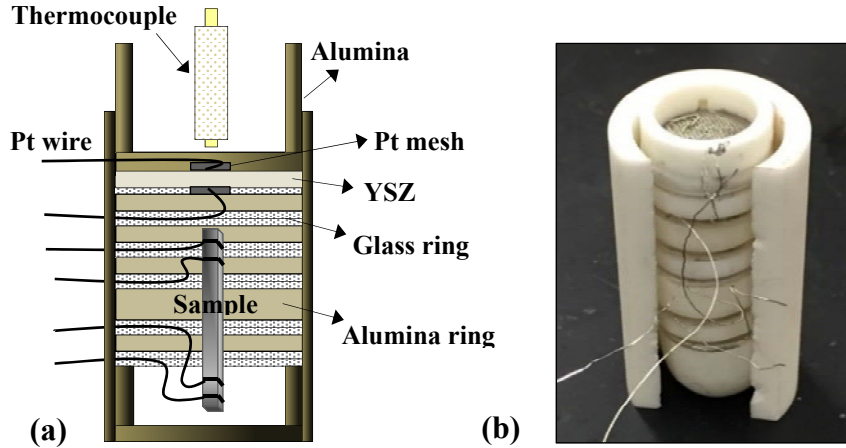


Fig. 4.2 (a) A gas-tight electrochemical cell for electrical conductivity experiments; (b) a photograph of a complete cell.

The electrical conductivity of the dense YBaMn_2O_5 bar were measured by a DC four-probe method using a Schlumberger SI 1260 Impedance/Gain-Phase analyzer, and controlled by CorrWare/CorrView software. The experiments were made on both increasing and decreasing temperature in the range of 500-750 °C at 10 °C intervals. The oxygen partial pressure at each temperature was controlled to ensure that the YBaMn_2O_5 sample was not oxidized during the measurements. According to the data shown in Fig. 3.3, the temperature dependence of the $p\text{O}_2$ for the oxidation from YBaMn_2O_5 to $\text{YBaMn}_2\text{O}_{5.5}$ indicates the appropriate $p\text{O}_2$ values for the electrical conductivity measurements at each temperature. The measurements were performed at the $p\text{O}_2$ values

between less than $\sim 10^{-19}$ atm at 500 °C, and less than $\sim 10^{-13}$ atm at 750 °C. The electrical conductivities were calculated by the following equation:

$$\sigma = (L \times I)/(A \times \Delta V) \quad (4.2)$$

where, σ is the electrical conductivity, L is the distance between two contact points, I is the applied current, A is the area of the cross-section of the rectangular bar, and ΔV is the difference of measured voltage between two probes. The activation energy for the electrical conductivity was calculated by using the standard Arrhenius model as the following:

$$\sigma = A \cdot \exp\left(-\frac{E_a}{RT}\right) \quad (4.3)$$

where, σ is the total conductivity (predominantly electronic), E_a is the activation energy, A is the pre-exponential factor, T is the absolute temperature, and R is the gas constant.

4.2.3 Thermal Expansion

The thermal-expansion behavior of the three phases (O_5 , $O_{5.5}$, and O_6) of $YBaMn_2O_{5+\delta}$ was investigated by dilatometry and high temperature X-ray diffraction under different atmospheres.

4.2.3.1 Dilatometry

Linear thermal-expansion measurements of $YBaMn_2O_{5+\delta}$ were performed using a horizontal push rod dilatometer (Netzsch DIL 402C) with an Al_2O_3 reference. The $YBaMn_2O_5$ samples used for dilatometry were cut into the rectangular bars with a size of $\sim 1.4 \text{ mm} \times 1.9 \text{ mm} \times (12.0\text{-}14.0) \text{ mm}$ from the same sintered circular pellet ($\sim 95\%$ of theoretical density) used in the electrical conductivity experiments. The thermal-

expansion measurements of the YBaMn₂O₅ bar were made in a reducing atmosphere of 1.99% H₂/Ar gas in the temperature range 25-900 °C with a heating/cooling rate of 8 °C min⁻¹. For YBaMn₂O₆, the YBaMn₂O₅ bar was oxidized in the dilatometer in air between room temperature and 800 °C with a heating/cooling rate of 2 °C min⁻¹. Subsequently, the thermal expansion of the oxidized sample was measured in air at 25-830 °C with the same heating/cooling rate. The weight change of the sample was monitored in a parallel TGA study, and shown to correspond to the formation of O₆. Afterwards, a sample of YBaMn₂O_{5.5} was made by reduction of the YBaMn₂O₆ sample bar in the dilatometer under a N₂ atmosphere between room temperature to 800 °C with a heating/cooling rate of 2 °C min⁻¹. The weight change of the reduced sample bar was measured and shown to correspond to the oxygen content (5+δ) ≈ 5.5. The thermal-expansion measurements of the YBaMn₂O_{5.5} sample bar were then carried out in N₂ atmosphere in the temperature range 25-800 °C with a heating/cooling rate of 5 °C min⁻¹. A gas flow of 100 cm³ min⁻¹ was used for all measurements. The parallel TGA experiments for oxidation of O₅ and reduction of O₆ to confirm the changes in oxygen contents under the same conditions used in dilatometry were made on small chunks of the samples from the same sintered dense pellet.

The linear thermal-expansion coefficient (TEC) can be calculated over a temperature range using the following equation:

$$\frac{\Delta L(T)}{L(T_0)} = \frac{L(T) - L(T_0)}{L(T_0)} = \alpha_L \cdot \Delta T \quad (4.4)$$

where, α_L is the linear thermal-expansion coefficient (TEC) between the temperatures T and T_0 , and $\frac{\Delta L(T)}{L(T_0)}$ is length change relative to L at T_0 .

4.2.3.2 High-temperature XRD studies

Only YBaMn₂O₅ and YBaMn₂O₆ powders were studied by high-temperature XRD. The synthesis of both powders was described in Chapter 2. The powder sample was placed on a Pt sample holder in the heating stage on a Phillips PANalytical X'Pert PRO diffractometer with Cu K α radiation ($\lambda = 1.54046 \text{ \AA}$). The measurements were carried out in 1.99% H₂/Ar with a gas flow of 80 cm³ min⁻¹ for YBaMn₂O₅, and in static air for YBaMn₂O₆. The data were measured first at 25 °C, and then on heating from 100 to 800 °C with increments of 100 °C. A heating/cooling rate of 10 °C/min was used. Finally, the data were collected at 25 °C after cooling. On reaching each temperature, the sample was kept for 10 minutes before the XRD measurements were performed. All XRD patterns were fitted through Le Bail refinement using GSAS/EXPGUI software.

4.2.4 Differential Scanning Calorimetry (DSC)

The DSC measurements were carried out on the LnBaMn₂O₆ (Ln = Y, Gd, Eu, Sm, Nd, and Pr) samples using the Mettler Toledo DSC 1. The sample powder (~20 mg) was measured with a heating/cooling rates of 10 °C/min in a negative temperature range from -150 °C up to 200 °C under a N₂ flow of 80 cm³ min⁻¹, and in 25-700 °C temperature range in static air. An aluminum/platinum sample crucible was used for measuring in a negative/high temperature range, respectively.

4.3 Results and Discussion

4.3.1 Characterization of the sample

The XRD pattern of the YBaMn₂O₅ pellet sintered at 1300 °C for 24 h under 10 ppm H₂/N₂ was measured to investigate the phase purity. The sample is single phase with no indication of impurities. The X-ray diffraction data were indexed with a tetragonal space group, P4/nmm, with lattice parameters $a = 5.5529(1) \text{ \AA}$ and $c = 7.6575(2) \text{ \AA}$. The refined X-ray pattern is presented in Fig. 4.3. The density of the pellet measured by the Archimedes method was 95.0(1) % relative to the theoretical value. The SEM microstructures for the polished surface and cross-section of the fresh YBaMn₂O₅ bar shown in Fig. 4.4 show good densifications with small amounts of pores, and were well-sintered.

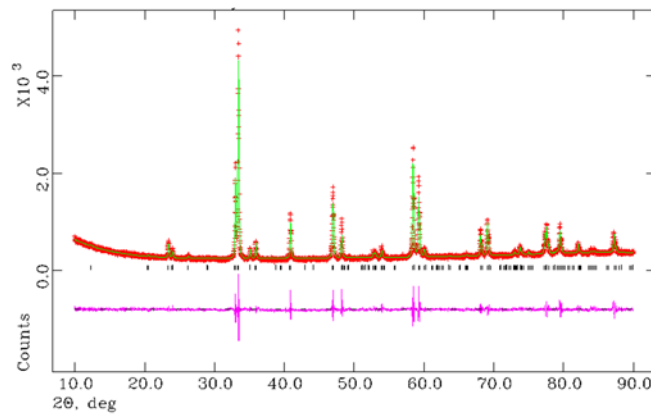


Fig. 4.3 X-ray data for the YBaMn₂O₅ pellet sintered at 1300 °C for 24 h in 10 ppm H₂/N₂. The measured data are shown in red, the calculated data are shown in green, and the difference is shown in pink. Bragg reflections are shown by vertical tick marks.

4.3.2 Electrical Conductivity

The electrical conductivity measurements were conducted in a gas-tight electrochemical cell in the 500–750 °C temperature range on both increasing and

decreasing temperature. The pO_2 values were controlled during the measurements depending on the temperature to avoid the possible oxidation of $YBaMn_2O_5$. The electrical conductivity (σ) for $YBaMn_2O_5$ as a function of temperature measured in the low- pO_2 range of 10^{-16} - 10^{-23} atm was plotted in Figure 4.5 (a).

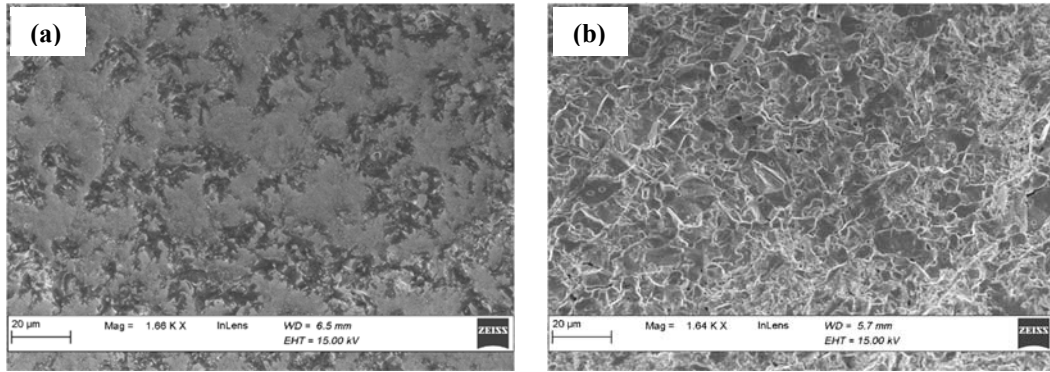


Fig. 4.4 SEM images showing the microstructures of the fresh $YBaMn_2O_5$ bar: (a) at the polished surface, and (b) on the cross-sectional area.

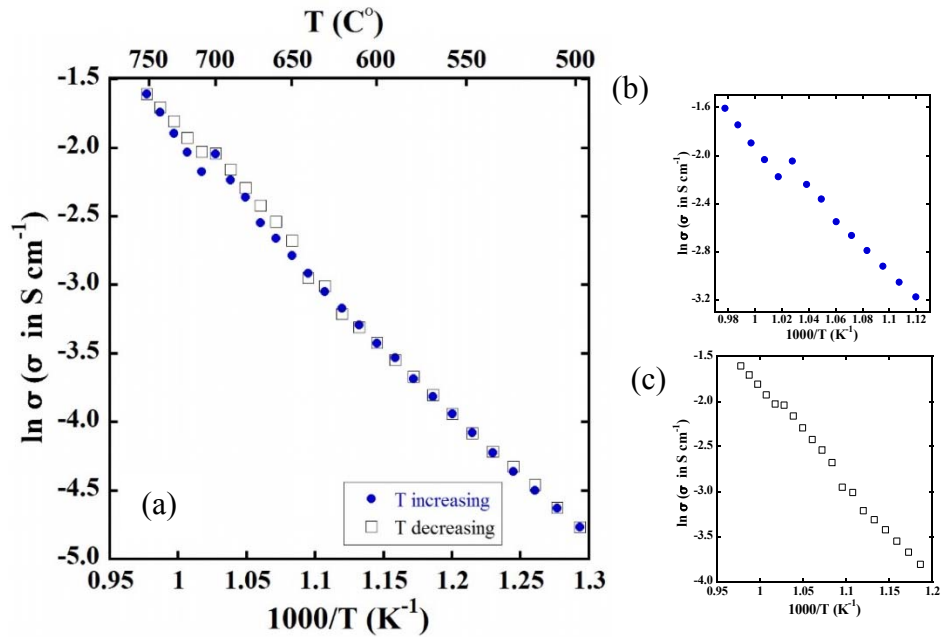


Fig. 4.5 The electrical conductivity of $YBaMn_2O_5$ in low- pO_2 region (a) in 500-750 °C on both increasing and decreasing temperature, (b) in 610-750 °C on increasing temperature, and (c) in 570-750 °C on decreasing temperature.

On increasing temperature, the electrical conductivity linearly increases with increasing temperature in 500-670 °C temperature range. Above 670 °C, the conductivity still increases, but starts to deviate from the linear relationship. The conductivity drops at 710 °C (see Fig 4.5 (b)), and then increases but with a different slope. On decreasing the temperature, the data show an increase at the same temperature (smaller in magnitude than the decrease observed on heating) and remain higher than the data obtained on increasing temperature (Fig 4.5 (c)). At 640 °C the data on increasing and decreasing T again coincide. The origin of the hysteresis and the nature of the transition are not yet completely understood (see below).

The electrical conductivity of YBaMn₂O₅ is relatively low, with an average activation energy (E_a) of 0.87 eV in 500-700 °C temperature range. The average electrical conductivity at 700 °C at $pO_2 \approx 10^{-16}$ atm is 0.13 S cm⁻¹. The present results can be compared with data from a previous study of EuBaMn₂O₅ [17]. The electrical conductivity and Seebeck coefficient were measured from room temperature to 600 °C in 5% H₂ in argon. The conductivity increased from 10⁻⁴ S cm⁻¹ at RT to ~10⁻¹ S cm⁻¹ at 600 °C; the Seebeck coefficient was positive over the whole temperature range indicating that the electronic charge carriers were electron holes. An activation energy of 0.3 eV was reported. At 600 °C, the conductivity of YBaMn₂O₅ is also low (0.03 S cm⁻¹) and the activation energy measured from 500 to 700 °C is higher (0.87 eV). The experiments are, however, not directly comparable because in the case of YBaMn₂O₅, pO_2 is controlled to prevent any oxidation above O₅. Furthermore, ac impedance measurements as a function of frequency show significant dispersion indicating an ionic component to the

conductivity. The magnitude of the activation energy (0.87 eV) is consistent with an ionic contribution.

The experiments were repeated several times on both increasing and decreasing temperature to check the reproducibility of the data. The results indicated that the data are acceptably consistent below 600 °C, but deviate from linearity at higher temperature, (>700 °C). The experiments take a long time (2-3 h/data point) to reach the equilibrium with respect to pO₂ and temperature, and consequently changes in the sample inside the electrochemical cell were suspected to be the reason for the irreproducible data. The sample was pulled out from the apparatus after the long-time experiments (~3 months). The sample bar was fragile and easily broken by hand. The outside color of the bar had changed from black to green with small white particles deposited on the surface, but still was black in the bulk of the sample as seen on the cross-sectional area. Figure 4.6 shows the SEM images of the surface and cross-section of the sample bar after the electrical conductivity experiments. The surface was dramatically affected by the reducing atmosphere and high temperature, and a segregation appeared on the surface, as seen in Fig. 4.6 (a-b), whereas the microstructures on the cross-sectional area before and after the electrical conductivity experiment were no different, as shown in Fig. 4.4 and 4.6 (c). The thickness of the segregated layer measured on the edge of the cross-sectional area in Fig. 4.6 (d) was around 25-27 μm. EDS analysis was carried out to determine the elements in the segregation zone at the surface. The EDS spectra obtained from several spots on the sample surface clearly show that only barium (Ba), oxygen (O) and carbon (C) elements were present at the surface, as shown in the example in Fig. 4.7. The trace of carbon

observed may originate from exposure of the sample to CO₂ present in air after the electrical conductivity experiments.

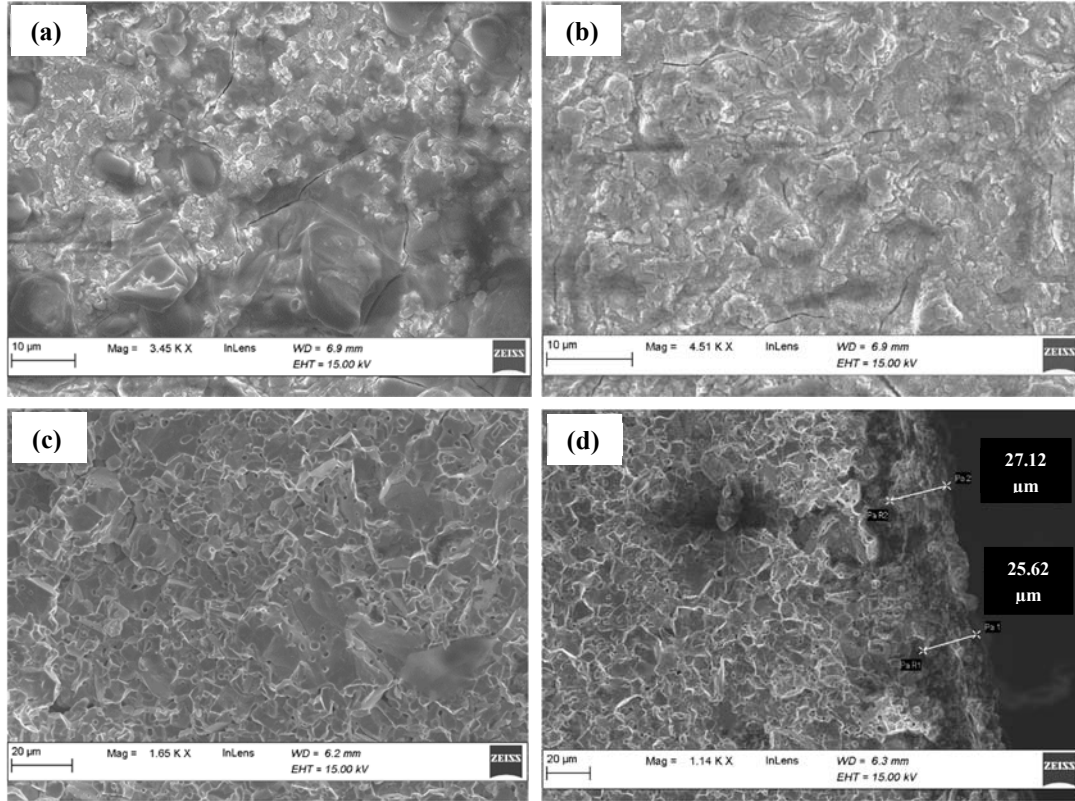


Fig. 4.6 SEM images of (a-b) surface, and (c-d) cross-section of YBaMn₂O₅ microstructure after the electrical conductivity experiments in low pO₂ atmosphere.

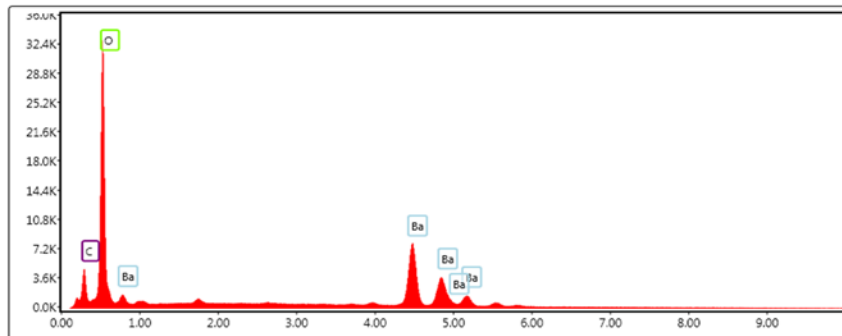


Fig. 4.7 EDS spectrum of the YBaMn₂O₅ surface after the long-time electrical conductivity experiments.

Accordingly, the results suggest that barium segregation occurs at the surface of the sample bar probably in the form of BaO. The cation ion segregation at the surface of perovskite oxides has been observed previously and is known to affect the activity and stability of materials [34-36]. The barium segregation at surface may reduce the oxygen ionic and electronic conductivity due to the presence of the less conductive BaO at the surface, and the possible interactions of Ba and Pt electrode wires at high temperatures.

4.3.3 Thermal Expansion of $\text{YBaMn}_2\text{O}_{5+\delta}$

The thermal-expansion behavior of the three phases (O_5 , O_6 , and $\text{O}_{5.5}$) of $\text{YBaMn}_2\text{O}_{5+\delta}$ were studied by high-temperature XRD (only for O_5 and O_6) and dilatometry measurements. The thermal expansion of mixed conducting perovskite oxides is attributed to crystal expansion from the atomic vibrations caused by increased thermal energy at elevated temperatures that depend on the electrostatic attraction forces within the lattice, and to chemical expansion induced by changes in oxygen stoichiometry [37-38].

4.3.3.1 YBaMn_2O_5

The X-ray diffraction data for YBaMn_2O_5 in high-temperature XRD experiments at 25-800 °C in 1.99% H_2/Ar showed only effects associated with the thermal expansion; no phase transformations were observed. All XRD patterns were indexed with the tetragonal P4/nmm space group, and the unit cell parameters and volume are summarized in Table 4.1. The linear thermal expansion, $\Delta L/L_0$, of YBaMn_2O_5 was calculated from the cubic root of the unit cell volume, and Figure 4.8 shows the temperature dependence of

linear thermal expansion of YBaMn₂O₅ in 1.99% H₂/Ar representing relative elongation of the sample upon heating. The thermal-expansion coefficients (TECs), α , can be extracted from the slope of the plot ($\Delta L/L_0$ vs. temperature) in Fig 4.8.

Table 4.1. Temperature dependences of the unit cell parameters, and volume of YBaMn₂O₅ determined by high-temperature XRD in 1.99% H₂/Ar.

Temperature (°C)	a (Å)	c (Å)	V (Å ³)	$\sqrt[3]{V}$ (Å)
25	5.5476(1)	7.6515(1)	235.48(1)	6.1752
100	5.5734(1)	7.6978(1)	239.12(1)	6.2069
200	5.5813(1)	7.7207(2)	240.50(1)	6.2188
300	5.5871(1)	7.7297(2)	241.28(1)	6.2255
400	5.5950(1)	7.7538(1)	242.72(1)	6.2379
500	5.6013(1)	7.7730(2)	243.88(1)	6.2478
600	5.6090(1)	7.7856(1)	244.94(1)	6.2568
625	5.6092(1)	7.7933(1)	245.20(1)	6.2590
650	5.6133(1)	7.7945(1)	245.42(1)	6.2609
700	5.6211(1)	7.8236(1)	247.20(1)	6.2760
750	5.6358(1)	7.8517(1)	249.39(1)	6.2945
800	5.6502(1)	7.8707(1)	251.27(1)	6.3103

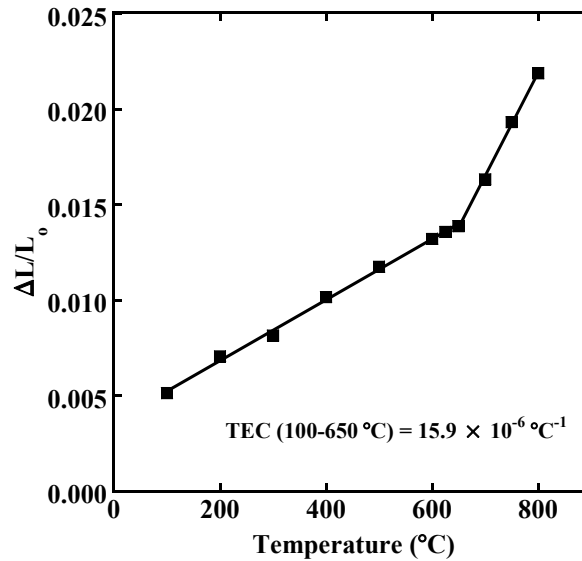


Fig. 4.8 Thermal-expansion data for YBaMn₂O₅ as function of temperature in 1.99% H₂/Ar, calculated from the cubic root of unit cell volume.

Two linear regions of thermal expansion are observed with a change in slope occurring at 650 °C. The TEC value in the temperature range of 650-800 °C is higher than that of the temperature range below 650 °C. In the lower temperature region, the TEC is $15.9 \times 10^{-6} \text{ }^\circ\text{C}^{-1}$. The origin of the discontinuity is discussed further below. A comparison of the unit cell parameters *a* and *c* of YBaMn₂O₅ (Table 4.1) indicates anisotropic thermal expansion. The TEC at 100-650 °C along the *a*-axis is $12.6 \times 10^{-6} \text{ }^\circ\text{C}^{-1}$ and along the *c*-axis is $23.0 \times 10^{-6} \text{ }^\circ\text{C}^{-1}$. This observed anisotropic character is probably associated with the cations ordering in the A-sites alternating along the *c*-axis of double perovskite structures, and consequently the oxygen vacancies are confined to the |YO₆| layers, resulting in the higher thermal expansion observed along the *c*-axis.

The linear thermal expansion of YBaMn₂O₅ obtained from dilatometry measurements in 1.99% H₂/Ar in 25-900 °C temperature range is shown in Figure 4.9. The data show unusual behavior. On heating above ~100 °C the expansion is close to linear and corresponds to a TEC of $15.5 \times 10^{-6} \text{ }^\circ\text{C}^{-1}$ over the temperature interval 100-550 °C in agreement with the result from the high temperature X-ray data. Beginning at ~630 °C, the expansion begins to increase more rapidly than observed at lower temperature and in a similar way to that observed in the high temperature X-ray experiment. The temperatures do not exactly correspond probably as a result of the experiments being carried out in different ways. The dilatometry measurements were obtained on a solid bar with a heating ramp whereas the X-ray data were obtained on a powder in temperature increments with a hold in between each step. On cooling from 900 °C, the expansion behavior is quite different. The TEC between 800 and 650 °C is $15.5 \times 10^{-6} \text{ }^\circ\text{C}^{-1}$ but at 630 °C it changes discontinuously. The origin of the anomalous behavior

is not yet certain. It is clearly not just thermal expansion (the effect is too large) and is unlikely to be due to chemical-composition changes since both experiments are run in a hydrogen gas atmosphere.

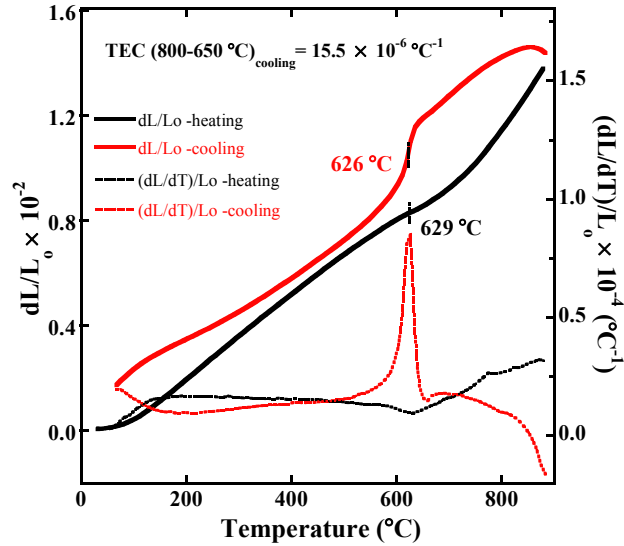


Fig. 4.9 Thermal-expansion behavior of YBaMn₂O₅ in 25-900 °C temperature range in 1.99% H₂/Ar, obtained by dilatometry experiments.

Similar behavior has been previously observed in LaBaCo₂O₅ (Jacobson *et al.*, unpublished) which can be prepared in a cation ordered form by heating in argon at 1050 °C. On heating the ordered form in air, high temperature X-ray diffraction data show that the ordered form is preserved (though oxidized) until about 1000 °C. At this temperature, the c axis length slowly increases until the sample becomes completely disordered at ~1150 °C. On cooling the sample remains disordered because it was oxidized on the heating cycle. A similar explanation is proposed to explain the anomalous thermal expansion observed for YBaMnO₅. On heating above 630 °C, the Y and Ba cations begin to disorder indicated by the increase in the expansion. Unlike the LaBaCo₂O₅ experiment, the YBaMnO₅ expansion measurement is carried out in hydrogen without significant

change in the vacancy content. The presence of vacancies permits the sample to revert to the ordered phase on cooling. This hypothesis requires experimental confirmation by a structural measurement on a sample in the disordered state either at high temperature or on a quenched sample. Model calculations show that the changes in the X-ray data on disordering Y and Ba are small but a neutron diffraction experiment should provide sufficient contrast.

4.3.3.2 YBaMn₂O_{5.5}

The linear thermal-expansion data of YBaMn₂O_{5.5} measured by dilatometry experiments in N₂ are shown in Fig. 4.10. A linear behavior of the linear thermal expansion is observed on both the heating and cooling with an average TEC value of $11.4 \times 10^{-6} \text{ }^\circ\text{C}^{-1}$ over a 100-800 °C temperature range. The results obtained during heating and cooling periods coincide with each other.

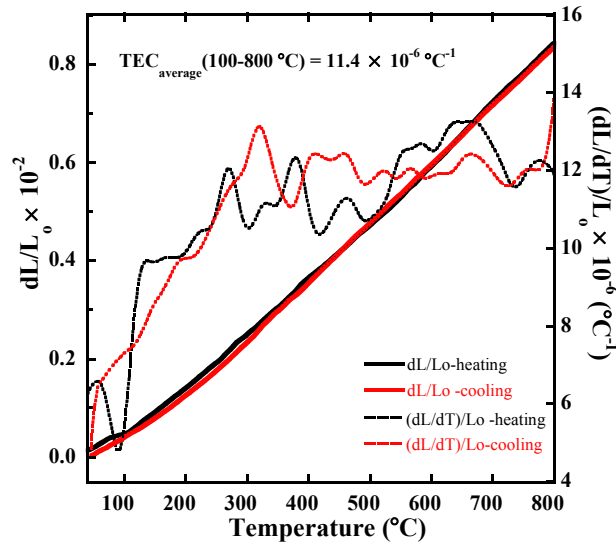


Fig. 4.10 Thermal-expansion behaviors of YBaMn₂O_{5.5} in N₂ in the temperature range of 25-800 °C, obtained by dilatometry experiments.

4.3.3.3 YBaMn₂O₆

The X-ray diffraction patterns recorded at selected temperatures for YBaMn₂O₆ in static air between 25-800 °C are shown in Figure 4.11. In addition to thermal expansion, our investigation indicated structural changes in YBaMn₂O₆ after heating to 300 °C and 500 °C. As reported by Williams *et al.* [16], powder neutron diffraction data for YBaMn₂O₆ showed the presence of two high-temperature phase transitions between room temperature and 500 °C; a charge ordering transition at $T \approx 225$ °C, and a structural transition at $T \approx 437$ °C. The refinement of the present XRD diffraction data at 25-500 °C uses the models developed in this previous work [16]. The diffraction data at 25, 100 and 200 °C show peak shifts due to thermal expansion but no change in symmetry. The data were refined in the triclinic $P\bar{1}$ space group [16, 39]. The data obtained after heating to 300 °C show a structural change which was modelled in the monoclinic space group C2/m. After heating to 400 °C, peak shifts due to the thermal expansion were observed but the symmetry remained C2/m. The diffraction data at 500 °C show another structural change and were fitted well with an orthorhombic Cmmm symmetry model. Only thermal expansion was observed in the diffraction data at higher temperature, 600-800 °C, which were refined in the orthorhombic Cmmm space group [18]. The unit cell parameters and volume of YBaMn₂O₆ at different temperatures are summarized in Table 4.2.

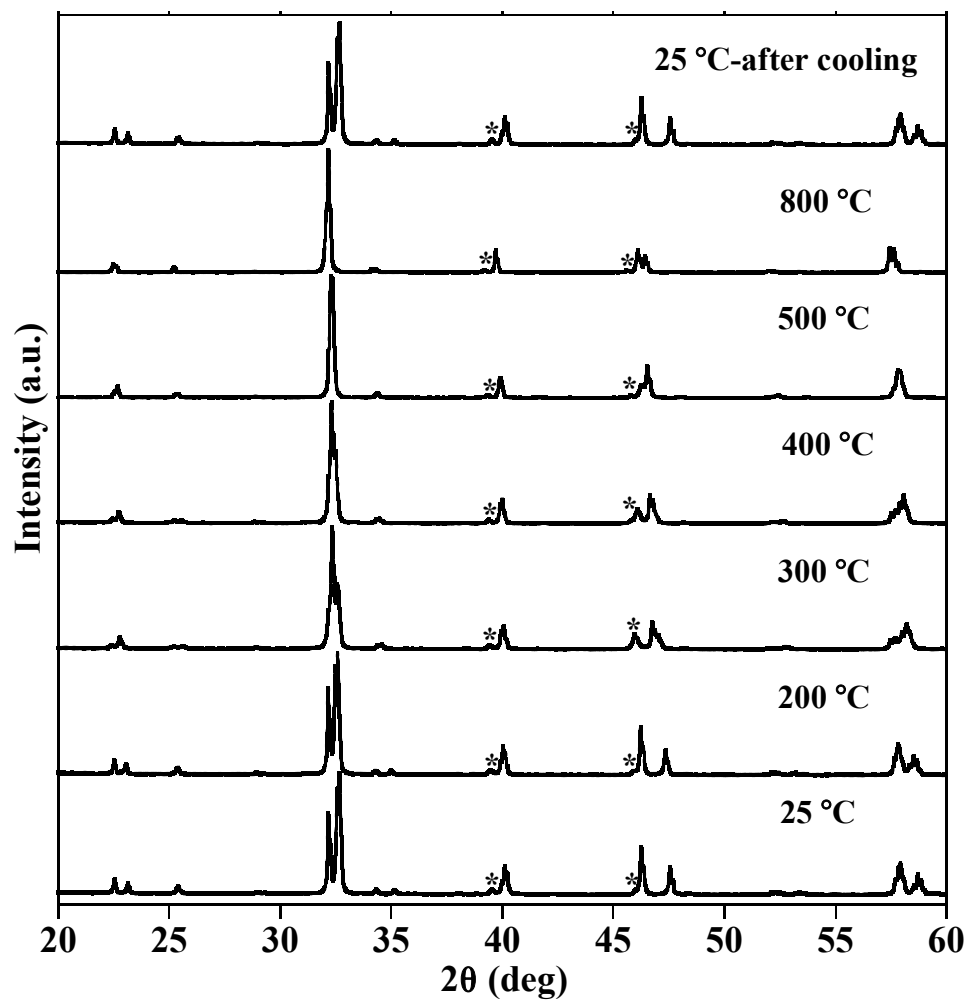


Fig. 4.11 XRD data for YBaMn₂O₆ recorded during heating up to 800 °C in static air and cooling down to room temperature. The asterisk (*) signs indicate Pt peaks from the Pt sample holder. The regions of the data where the Pt peaks occur were excluded during the refinement.

Table 4.2 Thermal evolution of the space group, the unit cell parameters, and the cubic root of the unit cell volume of YBaMn_2O_6 (normalized $Z=1$), obtained from high-temperature XRD studies in static air.

Temp. (°C)	Space group	a (Å)	b (Å)	c (Å)	α (deg.)	β (deg.)	γ (deg.)	V (Å ³)	Normalized V (Å ³)	$\sqrt[3]{V}$ (Å)
25	P $\bar{1}$	5.5239(0)	5.5188(0)	7.6078(0)	90.007(2)	90.301(1)	90.011(3)	231.92(0)	57.980	3.8704
100	P $\bar{1}$	5.5258(0)	5.5142(1)	7.6220(1)	90.003(1)	90.301(1)	90.134(1)	232.24(0)	58.060	3.8722
200	P $\bar{1}$	5.5232(0)	5.5194(1)	7.6386(1)	89.987(1)	90.285(1)	90.044(1)	232.85(1)	58.213	3.8756
300	C2/m	7.7343(1)	7.6951(1)	7.8599(1)		89.695(1)		467.78(1)	58.473	3.8814
400	C2/m	7.7538(1)	7.7284(1)	7.8457(1)		90.248(1)		470.15(1)	58.769	3.8879
500	Cmmm	7.7717(4)	7.7770(4)	7.8190(1)				472.58(1)	59.073	3.8946
600	Cmmm	7.8015(1)	7.8081(1)	7.7841(1)				474.17(1)	59.271	3.8990
700	Cmmm	7.7896(1)	7.8234(1)	7.8165(1)				476.34(1)	59.543	3.9049
800	Cmmm	7.8363(1)	7.8425(1)	7.7869(1)				478.56(1)	59.820	3.9109

The linear thermal expansion of YBaMn_2O_6 in static air at 100-800 °C was calculated from the cubic root of the normalized unit cell volume obtained from the high-temperature XRD studies, and the thermal expansion as a function of temperature is plotted in Fig. 4.12. The average thermal-expansion coefficient of YBaMn_2O_6 in static air in the temperature range of 100-800 °C equals $14.7 \times 10^{-6} \text{ }^\circ\text{C}^{-1}$. The data show, however, significant TEC differences for each of the three phases (15.4 , 17.1 , and $8.8 \times 10^{-6} \text{ }^\circ\text{C}^{-1}$ for Cmmm, C2/m, and P-1 phases, respectively).

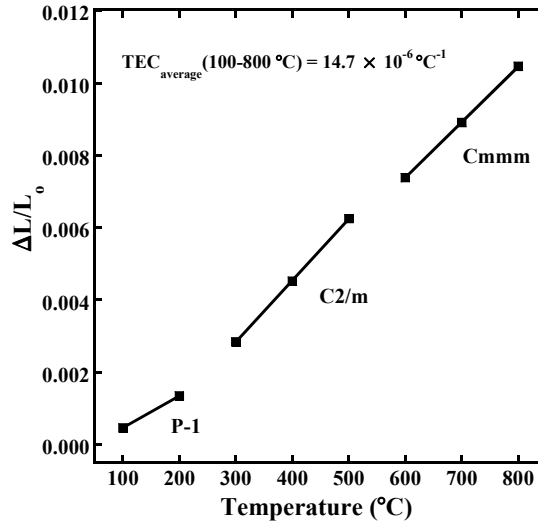


Fig. 4.12 Thermal-expansion data for YBaMn_2O_6 as function of temperature in static air at 25-800 °C, obtained from the high-temperature X-ray diffraction studies.

Results for dilatometry measurements on YBaMn_2O_6 in air at 100-800 °C are presented as dL/L_0 vs. T in Figure 4.13. On heating, the thermal expansion increases as the temperature increases in the low-temperature region (30-150 °C) with a TEC value of $8.3 \times 10^{-6} \text{ }^\circ\text{C}^{-1}$. Then, a small reduction of the thermal expansion occurs at 205 °C, and afterward the thermal expansion shows a steep drop at an inflection point, $T = 240 \text{ }^\circ\text{C}$. In the temperature range of 300-800 °C, linear behavior of thermal expansion is observed

with TEC value of $14.9 \times 10^{-6} \text{ }^\circ\text{C}^{-1}$, which is comparable with the value obtained from the HT-XRD studies (Fig. 4.12). On cooling, similar behavior of the thermal expansion in YBaMn_2O_6 is observed with a small and steep decrease in thermal expansion are found at lower temperature of 200 and 223 $^\circ\text{C}$, respectively.

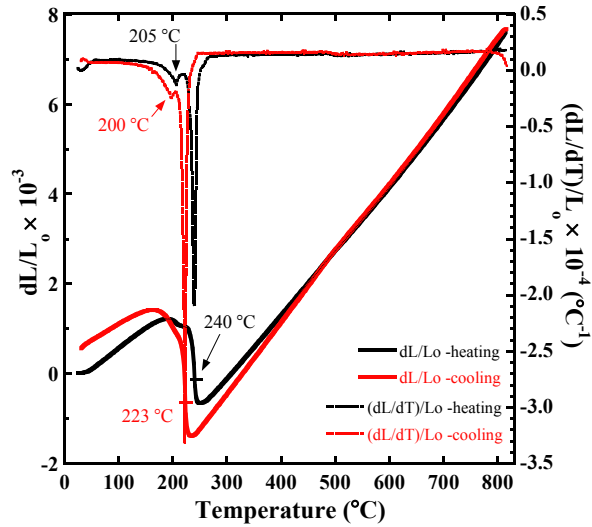


Fig. 4.13 Thermal-expansion behavior of YBaMn_2O_6 from 25-830 $^\circ\text{C}$ in air obtained by dilatometry.

The dilatometry data below 300 $^\circ\text{C}$ agree with the DSC measurements of YBaMn_2O_6 as presented in Fig. 4.14 (a). On heating, two endothermic peaks appear at $T_1 = 247$ and $T_2 = 208$ $^\circ\text{C}$, which correspond to the structural phase transition and the metal-insulator (M-I) transition, respectively [27-28]. On cooling, two exothermic peaks corresponding to both transitions are observed at lower temperatures of 230 and 204 $^\circ\text{C}$ than observed on heating. The transition temperatures from both experiments do not exactly match probably because the dilatometry measurements were done on a solid bar with a 2 $^\circ\text{C}/\text{min}$ ramp in an air flow but the DSC measurements were obtained on a sample powder with a 10 $^\circ\text{C}/\text{min}$ ramp in static air.

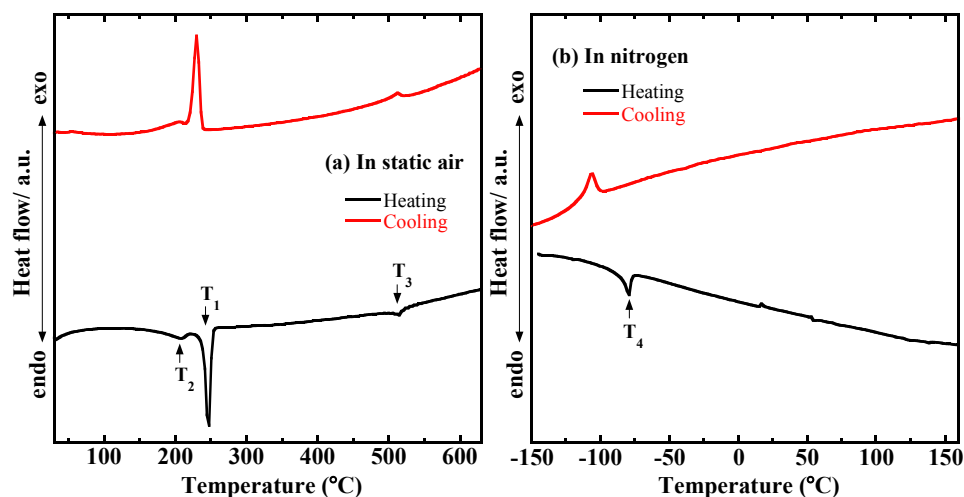


Fig. 4.14 DSC curves of YBaMn_2O_6 measured with a heating/cooling rate of $10\text{ }^\circ\text{C}/\text{min}$ in (a) static air, and (b) nitrogen.

4.3.4 Differential Scanning Calorimetry (DSC) of $\text{LnBaMn}_2\text{O}_6$

The reading of the DSC curves for YBaMn_2O_6 in Fig. 4.14 (a) suggests that besides the already-mentioned two peaks at $T_1 = 247$ and $T_2 = 208\text{ }^\circ\text{C}$ there is a weak endothermic peak at $T_3 = 515\text{ }^\circ\text{C}$ on heating with a corresponding exothermic peak observed at $513\text{ }^\circ\text{C}$ on cooling. In addition, Figure 4.14 (b) shows the DSC curves of YBaMn_2O_6 measured in N_2 flow with a $10\text{ }^\circ\text{C}/\text{min}$ heating/cooling rate over a negative temperature range, revealing an endothermic peak at $T_4 = -79\text{ }^\circ\text{C}$ on heating and a corresponding exothermic peak at lower temperature $-106\text{ }^\circ\text{C}$ on cooling. Reflecting the first-order transitions at T_1 and T_4 , the DSC peaks on cooling are observed at lower temperatures than those in heating, whereas the T_2 - and T_3 -corresponded peaks observed upon cooling are almost identical to those in the heating process indicating that these transitions are most likely second-order. The present DSC data of YBaMn_2O_6 are in good agreement with the DSC measurements in a temperature range of -123 to $327\text{ }^\circ\text{C}$ reported by Nakajima *et al.* [27-28] which show three transitions in YBaMn_2O_6 , namely, from the

structural phase transition (paramagnetic metal PM1 to PM2) at 247 °C, then to the paramagnetic insulator (PI) at 207 °C, and finally to the antiferromagnetic insulator (AFI) at -78 °C. The transition of YBaMn₂O₆ observed at T₃ = 515 °C, has not been reported in the literature. More experiments are needed to explain the high temperature properties.

DSC measurements were also made on the LnBaMn₂O₆ (Ln = Gd, Eu, Sm, Nd, and Pr) samples in static air over a 25-700 °C temperature range and under N₂ flow from -150 up to 200 °C with heating/cooling rates of 10 °C/min. No transition is detected at temperatures above 160 °C in Gd, Eu, Sm, Nd, and Pr samples. The transition temperatures obtained from the DSC curves of all samples are summarized in Table 4.3, and the DSC curves of the SmBaMn₂O₆ and NdBaMn₂O₆ are shown as examples in Fig. 4.15. According to reports on structural and magnetic properties of LnBaMn₂O₆ by Nakajima *et al.* [25, 31], the samples with Gd, Eu, and Sm cations exhibit the charge-ordering transition (MI) and the antiferromagnetic (AF) transition. For Ln = Nd and Pr, the samples show two transitions from paramagnetic metal (PM) to ferromagnetic metal (FM), and then to an A-type antiferromagnetic metal (AFM).

Table 4.3 Transition temperature for LnBaMn₂O₆ (Ln = Y, Gd, Eu, Sm, Nd, and Pr), obtained from the DSC curves upon heating (H) and cooling (C) processes.

	Transition temperature (°C)												
	Y		Gd		Eu		Sm		Nd		Pr		
	H	C	H	C	H	C	H	C	H	C	H	C	
T ₁	247	230											
T ₂	208	204	152	142	135	127	111	104	28	13	31	28	
T ₃	515	513											
T ₄	-79	-106	-72	-90	-70	-88	-74	-94	-32	-45	-28	-59	

H= heating; C= cooling

In comparison with the transition temperatures estimated from the electronic phase diagram of $\text{LnBaMn}_2\text{O}_6$ proposed by Nakajima *et al.* [25], the observed DSC peaks at T_2 and T_4 correspond to the MI and AF transitions respectively for $\text{Ln} = \text{Gd}, \text{Eu},$ and Sm , and to the FM and A-type AFM transitions for $\text{Ln} = \text{Nd}$ and Pr . However, the DSC peaks at negative transition temperature, T_4 , in the present study were found at much lower temperature than those previously reported.

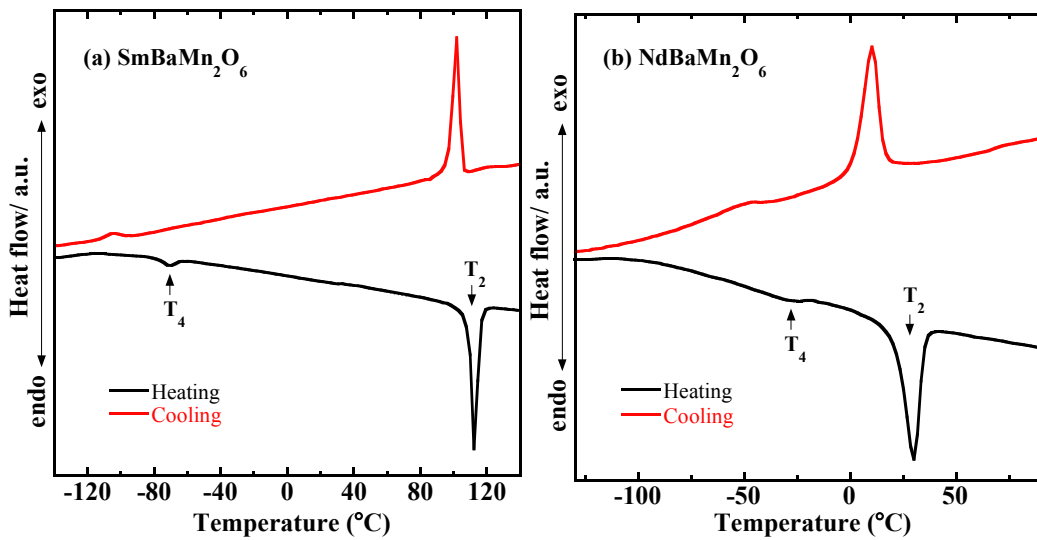


Fig. 4.15 DSC curves of $\text{LnBaMn}_2\text{O}_6$ with (a) $\text{Ln} = \text{Sm}$, and (b) $\text{Ln} = \text{Nd}$, measured under nitrogen flow with a heating/cooling rate of $10\text{ }^\circ\text{C}/\text{min}$.

4.4 Conclusions

A dense pellet of YBaMn_2O_5 was prepared by cold-isostatic pressing a polycrystalline powder and sintering at $1300\text{ }^\circ\text{C}$ under a $10.0\text{ ppm H}_2/\text{N}_2$ gas atmosphere. The density of the pellet was $\sim 95\%$ density of the theoretical value. The electrical conductivity was studied as a function of temperature in the low- $p\text{O}_2$ range of $10^{-16} - 10^{-23}$ atm by using the four-probe DC method in an electrochemical cell. The electrical conductivity of YBaMn_2O_5 in low- $p\text{O}_2$ region linearly increased with increasing

temperature with an average activation energy (E_a) of 0.87 eV in the 500-700 °C temperature range. The barium migration and segregation on the sample surface were observed after the long-period experiments in low-pO₂ atmosphere at high temperatures. The linear thermal expansion for the three phases (O₅, O₆, and O_{5.5}) of YBaMn₂O_{5+δ} was investigated by dilatometry measurements and high-temperature XRD studies under different atmospheres. The thermal-expansion coefficient (TEC) obtained from dilatometry is $15.5 \times 10^{-6} \text{ °C}^{-1}$ for YBaMn₂O₅ in 1.99% H₂/Ar in 100-550 °C, $14.9 \times 10^{-6} \text{ °C}^{-1}$ for YBaMn₂O₆ in air in 300-800 °C, and $11.4 \times 10^{-6} \text{ °C}^{-1}$ for YBaMn₂O_{5.5} in N₂ in 100-800 °C. The structural evolution of YBaMn₂O₆ at elevated temperatures obtained from high-temperature XRD in air was also discussed. DSC measurements are reported for the LnBaMn₂O₆ (Ln = Gd, Eu, Sm, Nd, and Pr) compounds confirming the phase transitions present in these compounds.

4.5 References

1. King, G.; Woodward, P. M. *J. Mater. Chem.* **2010**, *20*, 5785-5796.
2. Karppinen, M.; Okamoto, H.; Fjellvåg, H.; Motohashi, T.; Yamauchi, H. *J. Solid State Chem.* **2004**, *177*, 2122-2128.
3. Chapman, J. P.; Attfield, J. P.; Molgg, M.; Friend, C. M.; Beales, T. P. *Angew. Chem. Int. Ed. Engl.* **1996**, *35* (21), 2482-2484.
4. Perca, C.; Pinsard-Gaudart, L.; Daoud-Aladine, A.; Fernández-Díaz, M. T.; Rodríguez-Carvajal, J. *Chem. Mater.* **2005**, *17* (7), 1835-1843.
5. Beales, T. P.; Molgg, M.; Jutson, J.; Friend, C. M. *Phys. Stat. Sol. A* **1997**, *161* (1), 271-282.
6. Williams, A. J.; Attfield, J. P. *Phys. Rev. B* **2002**, *66*, 220405.
7. Taskin, A. A.; Ando, Y. *Phys. Rev. Lett.* **2007**, *98* (20), 207201.

8. Vidya, R.; Ravindran, P.; Knizek, K.; Kjekshus, A.; Fjellvåg, H. *Inorg. Chem.* **2008**, *47* (15), 6608-6620.
9. Vidya, R.; Ravindran, P.; Kjekshus, A.; Fjellvåg, H. *Phys. Rev. B* **2007**, *76* (19), 195114.
10. Trukhanov, S. V.; Troyanchuk, I. O.; Hervieu, M.; Szymczak, H.; Bärner, K. *Phys. Rev. B* **2002**, *66* (18), 184424.
11. Caignaert, V.; Millange, F.; Domengès, B.; Raveau, B.; Suard, E. *Chem. Mater.* **1999**, *11* (4), 930-938.
12. Troyanchuk, I. O.; Trukhanov, S. V.; Szymczak, G. *Crystallogr. Rep.* **2002**, *47* (4), 716-723.
13. Troyanchuk, I. O.; Trukhanov, S. V.; Chobot, G. M.; Szymczak, H. *Phys. Solid State* **2003**, *45* (2), 276-282.
14. Kageyama, H.; Nakajima, T.; Ichihara, M.; Ueda, Y.; Yoshizawa, H.; Ohoyama, K. *J. Phys. Soc. Jpn.* **2003**, *72* (2), 241-244.
15. Akahoshi, D.; Okimoto, Y.; Kubota, M.; Kumai, R.; Arima, T.; Tomioka, Y.; Tokura, Y. *Phys. Rev. B* **2004**, *70* (6), 064418.
16. Williams, A. J.; Attfield, J. P.; Redfern, S. A. T. *Phys. Rev. B* **2005**, *72*, 184426.
17. Świerczek, K.; Klimkowicz, A.; Zheng, K.; Dabrowski, B. *J. Solid State Chem.* **2013**, *203*, 68-73.
18. Motohashi, T.; Takahashi, T.; Kimura, M.; Masubuchi, Y.; Kikkawa, S.; Kubota, Y.; Kobayashi, Y.; Kageyama, H.; Takata, M.; Kitagawa, S.; Matsuda, R. *J. Phys. Chem. C* **2015**, *119*, 2356-2363.
19. Shin, T. H.; Myung, J.-H.; Verbraeken, M.; Kim, G.; Irvine, J. T. S. *Faraday Discuss.* **2015**, *182*, 227-239.
20. Klimkowicz, A.; Świerczek, K.; Takasaki, A.; Molenda, J.; Dabrowski, B. *Mater. Res. Bull.* **2015**, *65*, 116-122.
21. Tonus, F.; Bahout, M.; Dorcet, V.; Gauthier, G. H.; Paofai, S.; Smith, R. I.; Skinner, S. J. *J. Mater. Chem. A* **2016**, *4* (30), 11635-11647.
22. Pineda, O. L.; Moreno, Z. L.; Roussel, P.; Świerczek, K.; Gauthier, G. H. *Solid State Ionics* **2016**, *288*, 61-67.
23. Klimkowicz, A.; Świerczek, K.; Zheng, K.; Wallacher, D.; Takasaki, A. *J. Mater. Sci.* **2017**, *52* (11), 6476-6485.

24. Castillo-Martínez, E.; Williams, A. J.; Attfield, J. P. *J. Solid State Chem.* **2006**, *179* (11), 3505-3510.
25. Nakajima, T.; Kageyama, H.; Yoshizawa, H.; Ueda, Y. *J. Phys. Soc. Jpn.* **2002**, *71* (12), 2843-2846.
26. Ueda, Y.; Nakajima, T. *J. Phys.: Condens. Matter* **2004**, *16*, S573-S583.
27. Nakajima, T.; Kageyama, H.; Ueda, Y. *J. Phys. Chem. Solids* **2002**, *63*, 913-916.
28. Nakajima, T.; Kageyama, H.; Ichihara, M.; Ohoyama, K.; Yoshizawa, H.; Ueda, Y. *J. Solid State Chem.* **2004**, *177*, 987-999.
29. Nakajima, T.; Yamauchi, T.; Yamaura, J.; Ueda, Y. *J. Phys. Chem. Solids* **2006**, *67*, 620-623.
30. Millange, F.; Caignaert, V.; Domenge's, B.; Raveau, B. *Chem. Mater.* **1998**, *10* (7), 1974-1983.
31. Nakajima, T.; Kageyama, H.; Yoshizawa, H.; Ohoyama, K.; Ueda, Y. *J. Phys. Soc. Jpn.* **2003**, *72* (12), 3237-3242.
32. Trukhanov, S. V.; Trukhanov, A. V.; Szymczak, H.; Szymczak, R.; Baran, M. *J. Phys. Chem. Solids* **2006**, *67*, 675-681.
33. Sengodan, S.; Choi, S.; Jun, A.; Shin, T. H.; Ju, Y.-W.; Jeong, H. Y.; Shin, J.; Irvine, J. T. S.; Kim, G. *Nat. Mater.* **2015**, *14* (2), 205-209.
34. Tsai, C.-Y.; Dixon, A. G.; Ma, Y. H.; Moser, W. R.; Pascucci, M. R. *J. Am. Ceram. Soc.* **1998**, *81* (6), 1437-1444.
35. Lee, W.; Han, J. W.; Chen, Y.; Cai, Z.; Yildiz, B. *J. Am. Chem. Soc.* **2013**, *135* (21), 7909-7925.
36. Martynczuk, J.; Efimov, K.; Robben, L.; Feldhoff, A. *J. Membr. Sci.* **2009**, *344* (1-2), 62-70.
37. Remsen, S.; Dabrowski, B. *Chem. Mater.* **2011**, *23*, 3818-3827.
38. Zhou, W.; Ran, R.; Shao, Z.; Jin, W.; Xu, N. *J. Power Sources* **2008**, *182* (1), 24-31.
39. Klimkowicz, A.; Zheng, K.; Fiolka, G.; Świerczek, K. *Chemik* **2013**, *67* (12), 1199-1206.

CHAPTER 5

Summary and Future Work

5.1 Summary

Non-stoichiometric oxides with reversible oxygen uptake/release capability are called oxygen-storage materials. This research has been mainly focused on the A-site double-perovskite oxides $\text{LnBaMn}_2\text{O}_{5+\delta}$ which have recently attracted a lot of interest as good OSM candidates. The goals were to investigate the crystal structure, oxygen-storage properties, oxygen non-stoichiometric behavior, and electrical properties of the $\text{LnBaMn}_2\text{O}_{5+\delta}$ oxides ($\text{Ln} = \text{Y, Gd, Eu, Sm, Nd, and Pr}$).

The A-site double perovskite oxides $\text{LnBaMn}_2\text{O}_{5+\delta}$ ($\text{Ln} = \text{Y, Gd, Eu, Sm, Nd, and Pr}$) were synthesized by solid-state reaction. The unit cell volumes of $\text{LnBaMn}_2\text{O}_{5+\delta}$ are linearly dependent on the ionic radius of the Ln^{3+} ion. Thermogravimetric analyses show good oxygen uptake/release ability at moderate temperatures with oxygen-storage capacity (OSC) exceeding 3 wt. % for all $\text{LnBaMn}_2\text{O}_{5+\delta}$ compounds. These oxides exhibit reversible oxygen uptake/release characteristics between fully-reduced $\text{LnBaMn}_2\text{O}_5$ and fully-oxidized $\text{LnBaMn}_2\text{O}_6$ during changes of the oxygen partial pressure between oxygen (or air) and 1.99% H_2/Ar . The A-site cationic substitution strongly influences the oxygen uptake/release behavior of the $\text{LnBaMn}_2\text{O}_{5+\delta}$ oxides. $\text{LnBaMn}_2\text{O}_5$ with a larger Ln^{3+} ion starts to take up oxygen at a lower temperature in both air and oxygen atmospheres.

The oxygen non-stoichiometries of $\text{LnBaMn}_2\text{O}_{5+\delta}$ ($\text{Ln} = \text{Y, Gd, and Pr}$) were measured as a function of $p\text{O}_2$ at 600, 650, 700 and 750 °C by solid-state Coulometric

titration technique. Two distinct phases (with $\delta \approx 0, 0.5$) and a third phase with a range of composition with the δ value approaching $\delta \approx \sim 1$ are observed during oxidation/reduction. The phase transition occurs at higher pO_2 with increasing temperature. At constant temperature, the pO_2 for reduction of $LnBaMn_2O_{5+\delta}$ decreases with increasing the size of the Ln^{3+} cation. Phase instability with respect to decomposition to $BaMnO_{3-\delta}$ and $LnMnO_3$ were observed under some conditions (high pO_2 , high temperature, long times) The thermodynamic quantities corresponding to the oxidation of $LnBaMn_2O_5$ to $LnBaMn_2O_{5.5}$ and of $LnBaMn_2O_{5.5}$ to $LnBaMn_2O_{5.6}$ were determined.

The electrical conductivity of $YBaMn_2O_5$ was studied by using the four-probe DC method in an electrochemical cell was reported as a function of temperature in the low- pO_2 range of 10^{-16} to 10^{-23} atm. The $YBaMn_2O_5$ compound has a relatively low electrical conductivity of 0.13 S cm^{-1} at $700 \text{ }^\circ\text{C}$, with an average activation energy (E_a) of 0.87 eV in the $500\text{-}700 \text{ }^\circ\text{C}$ temperature range. The electrical conductivity linearly increases with increasing temperature. Barium migration and segregation on the sample surface were observed after the long-period experiments in low- pO_2 atmosphere at high temperatures. The thermal-expansion behavior of $YBaMn_2O_{5+\delta}$ was investigated by dilatometry measurements and high-temperature XRD studies under different atmospheres. DSC measurements were reported to confirm the structural and electronic phase transitions present in the $LnBaMn_2O_6$ ($Ln = Y, Gd, Eu, Sm, Nd, \text{ and Pr}$) compounds.

5.2 Future Work

The synthesis of half-reduced $\text{NdBaMn}_2\text{O}_{5.5}$ is ongoing and needs to be finished to complete the structural data in this compound system. Further studies on the crystal structure of the $\text{LnBaMn}_2\text{O}_{5+\delta}$ oxides by high-temperature synchrotron X-ray diffraction (SXR) under controlled oxygen partial pressure are suggested to gain deeper understanding of oxygen uptake/release behavior of these oxides. Only the high-temperature SXR study of $\text{YBaMn}_2\text{O}_{5+\delta}$ was reported in the literature [1].

In addition to the electrical conductivity results of YBaMn_2O_5 , the electrical conductivity experiments need to be made on the fully-oxidized YBaMn_2O_6 which is expected to show higher conductivity than YBaMn_2O_5 . Additional studies on the dense-pellet fabrication of $\text{LnBaMn}_2\text{O}_{5+\delta}$ with other lanthanide-substitutions and the electrical conductivity of all the three phases (O_5 , $\text{O}_{5.5}$, and O_6) for the $\text{LnBaMn}_2\text{O}_{5+\delta}$ oxides will give useful knowledge for possible applications. An investigation of the Seebeck coefficients is needed to explain and better understand the mechanisms behind the electrical conductivity of these materials.

In order to confirm that the anomalous thermal-expansion behavior in YBaMn_2O_5 is resulted from the disordering of Y and Ba at high temperature above 630 °C, additional structural measurements on a sample in the disordered state either at high temperature or on a quenched sample are required. High-temperature neutron diffraction studies are suggested to provide sufficient structural data for determining the degree of disordering between Y and Ba. Apart from $\text{YBaMn}_2\text{O}_{5+\delta}$, more investigation on the thermal-expansion behavior of the $\text{LnBaMn}_2\text{O}_{5+\delta}$ oxides with other Ln cations should be made to explore their potential for use in the applications, such as SOFC electrodes.

In the DSC measurements, the transition of YBaMn₂O₆ observed at the temperature 515 °C has not been reported in the literature. More experiments, for example, magnetic susceptibility and electric resistivity, are needed to explain the high-temperature properties.

5.3 References

1. Motohashi, T.; Takahashi, T.; Kimura, M.; Masubuchi, Y.; Kikkawa, S.; Kubota, Y.; Kobayashi, Y.; Kageyama, H.; Takata, M.; Kitagawa, S.; Matsuda, R. *J. Phys. Chem. C* **2015**, *119*, 2356-2363.